Hongben Zhou

Investigation of toner adhesion in the electrophotographic process

Untersuchung der Tonerhaftung in dem elektrofotografischen Prozess

Cuvillier Verlag Göttingen

Investigation of toner adhesion in the electrophotographic process

---

Untersuchung der Tonerhaftung in dem elektrofotografischen Prozess

Der Technischen Fakultät der
Universität Erlangen-Nürnberg
zur Erlangung des Grades

DOKTOR-INGENIEUR

vorgelegt von

Hongben Zhou

Erlangen – 2008

Bibliografische Information der Deutschen Nationalbibliothek
Die Deutsche Nationalbibliothek verzeichnet diese Publikation in der Deutschen Nationalbibliografie; detaillierte bibliografische Daten sind im Internet über http://dnb.ddb.de abrufbar.
1. Aufl. - Göttingen : Cuvillier, 2008
Zugl.: Erlangen-Nürnberg, Univ., Diss., 2008

978-3-86727-748-8

Nonnenstieg 8, 37075 Göttingen
Telefon: 0551-54724-0
Telefax: 0551-54724-21
www.cuvillier.de

1. Auflage, 2008
Gedruckt auf säurefreiem Papier

978-3-86727-748-8

Als Dissertation genehmigt von

der Technischen Fakultät der

Universität Erlangen-Nürnberg

Tag der Einreichung:	04.04.2008
Tag der Promotion:	16.07.2008
Dekan:	Prof. Dr.-Ing. habil. Johannes Huber
Berichterstatter:	Prof. Dr.-Ing. Wolfgang Peukert
	Prof. Dr.-Ing. Karl Sommer

Acknowledgements

Though only my name appears on the cover of this dissertation, a great many people have contributed to this production during my time at the Institute of Particle Technology of Munich/Erlangen. My deepest gratitude is to my advisor, Prof. Wolfgang Peukert, for his support and guidance. Throughout my doctoral work he encouraged me to develop independent thinking and research skills. He continually stimulated my analytical thinking and greatly assisted me with scientific writing.

I want to thank Prof. Karl Sommer and his group for the fruitful discussions about adhesion phenomena and for providing me with their equipment for the centrifugal detachment measurements. My thanks also go to the groups of Prof. Mathias Göken und Prof. Günther Kuhn for their assistance in measuring of the material properties of polystyrene and in modeling the influence of the material properties on the adhesion behavior.

Furthermore, I would like to thank Dr. Manfred Münz and his group of Océ Printing Systems GmbH and Andreas Küttner of Epping GmbH for providing me with the materials and the equipment for the project. Special thanks go to Dr. Rainer Hoffman of Océ for many valuable discussions and for the organization of the cooperation.

I am grateful for the assistance and advice received from the colleagues in Munich and in Erlangen, especially to Dr. Martin Götzinger, who helped me at the beginning of the project. I benefited greatly from his brilliant ideas on how to carry out the experiments. My thanks go also to Xufeng Zhao, Martina Kormann, Darmawan Bhoga and Mohammad Alnaief for their great contribution.

The financial support of Bayerische Forschungsstiftung and Océ Printing Systems GmbH is gratefully acknowledged.

I am particularly grateful to my parents Baoyu Gao and Yuwei Zhou for their continuous encouragement, faith and, above all, their love. Thank you for everything.

Finally, and most importantly, I would like to thank my wife and best friend, Zhengyu Cai, for her love and patience throughout all these busy years. I can never thank her enough for standing by me through the good times and bad times.

Abstract

Adhesion between particles and surfaces is an essential phenomenon for many industrial applications. For example, the key to optimize the electrophotographic process is to understand the adhesion forces between charged toner particles and the photoconductive drum surface. The relevant adhesion forces in this process are the van der Waals, the capillary and the electrostatic forces. In the frame of this work these forces and their dependence on various parameters are investigated by means of AFM, centrifugal detachment and electric field detachment methods. The results are compared with each other and further with model calculations and numerical simulations.

The van der Waals force is identified as the dominating adhesion force in the observed systems. This force is mainly depending on the Hamaker constants and the structure of the contact region. In case of deformable adhesion partners their mechanical properties and the applied load have strong impacts on the van der Waals force as well. The capillary force amounts to the same order of magnitude as the van der Waals force, if the surfaces of the adhesion partners are smooth, while it is negligible between rough adhesion partners. The electrostatic force is usually significantly smaller than the van der Waals force. However, it can result in the relocation of particles and may thus lead to a significant increase of the van der Waals force.

Zusammenfassung

Die Haftung zwischen Partikeln und Oberflächen ist für viele industrielle Anwendungen von großer Bedeutung. So erfordert zum Beispiel die Optimierung des Druckprozesses ein vertieftes Verständnis der Haftkräfte zwischen Tonerteilchen und der Oberfläche der Fotoleitertrommel. Die wesentlichen Haftkräfte in diesem Prozess sind neben der van-der-Waals-Kraft die Kapillar- und die elektrostatische Kraft. Im Rahmen dieser Arbeit werden diese Kräfte sowie ihre Abhängigkeit von verschiedenen Parametern mittels AFM- und Zentrifugenmessungen sowie Messung der Partikelablösung im elektrischen Feld untersucht. Die Messergebnisse werden sowohl untereinander als auch mit Modellrechnungen und numerischen Simulationen verglichen.

Die van-der-Waals-Kraft ist die dominierte Haftkraft des untersuchten Systems. Sie ist vor allem von der Hamakerkonstante und der Struktur des Kontaktbereichs abhängig. Bei deformierbaren Haftpartnern beeinflussen zudem die mechanischen Eigenschaften und die aufgebrachte Normalkraft auf die van-der-Waals-Kraft. Zwischen glatten Haftpartnern ist die Größenordnung der Kapillarkraft mit der der van-der-Waals-Kraft vergleichbar. Zwischen rauen Oberflächen ist die Kapillarkraft jedoch vernachlässigbar. Die elektrostatische Kraft ist in der Regel deutlich kleiner als die van-der-Waals-Kraft, sie führt jedoch zur Umlagerung der Partikeln und dadurch zu einer signifikanten Erhöhung der van-der-Waals-Kraft.

Contents

1 INTRODUCTION

1.1 Motivation

Adhesion of particles on surfaces is a subject of particular interest in process engineering because of its importance in a wide range of industrial fields. One interesting application is the electrophotographic process, also called xerography, which was invented by Carlson and Kornei in 1938 [1]. Since the first commercially available electrophotographic equipment in 1950 this technique has been widely applied because of the high printing quality and low page costs. Nowadays typical commercial high-speed printers use paper speed of up to $1.5\,m/s$, corresponding to 600 A4 pages per minute at a print resolution of 600 dots per inch (dpi) [2]. However, a complete transfer of the toner particles to the paper is not yet possible. A fraction of the particles remains sticking on the photo conductor (PC) surface and has to be mechanically cleaned afterwards. General information on the electrophotographic process can be found in reviews of Goel [1], Schein [3], and Williams [4]. These works show that further improvement of this process requires understanding of the fundamental physical mechanisms of adhesion.

In this work the adhesion behavior between toner particles as well as model particles and substrates is investigated by various experimental techniques at boundary conditions relevant to the electrophotographic process, in order to understand the physics behind the adhesion phenomena. The measurements are compared with model calculations. Furthermore, it is shown that the adhesion force can be tailored by systematical modifications of the particle and the substrate surfaces.

1.2 Adhesion force in the electrophotographic process

Prints resulting from the electrophotographic process consist of micron-sized toner particles. Toner particles are charged triboelectrically: They are mixed with carrier particles (ferrite particle with a polymer coating) and intensively agitated. In this process the toner particles tend to become negatively charged. The toner-carrier mixture builds a thick layer on the magnet roller (MR) (Figure 1-1). When this layer contacts the jumper roller (JR), part of the toner particles is transferred onto the JR, so that the JR is covered with several monolayers of toner particles. The carrier particles cannot be transferred because of the strong magnetic force between the particles and the MR.

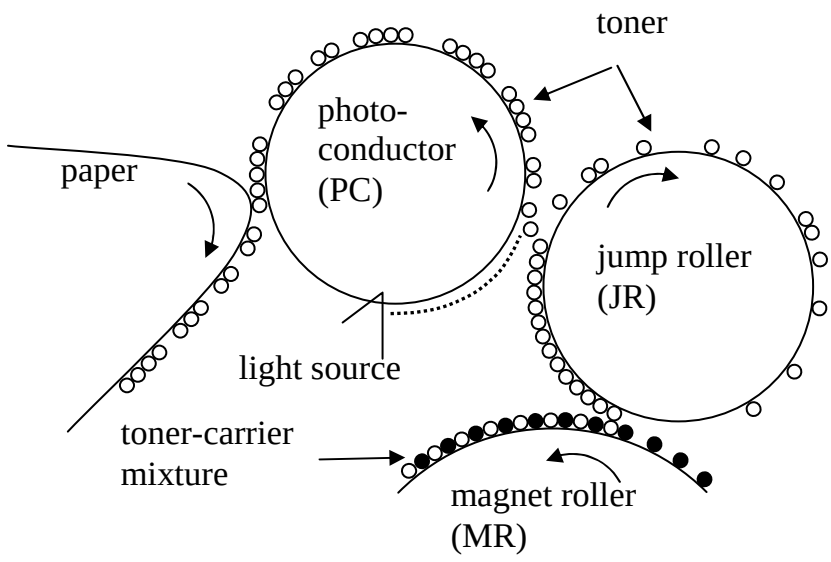

Figure 1-1 Schematic diagram of the electrophotographic process [2].

In the meanwhile, a charge pattern is produced on the photoconductor (PC) surface. The PC surface consists of a light sensitive material. The specific resistance of this material reduces from approximately $10^{14}\,\Omega cm$ to $10^{7}\,\Omega cm$ when the surface is moved from the darkness to the light. The charge pattern is created in two steps: In the darkness the surface becomes homogeneously charged by means of a corona. As for the toner particles, the charge is also negative. Then the locations that will form the toner image are illuminated with a tightly focused light beam emitted from the print head. The local resistance reduces so that the surface charges flow off, while the positions, which are not illuminated, remain charged.

When the toner particles on the JR approach the PC surface, the particles can be removed from the JR by the electric field force of a transfer corona and jump to the PC surface. The particles adhere on discharged locations of the PC surface. The particles are not able to adhere on the positions which are not illuminated because of the strong repulsive force between the particle charge and the surface charge on the PC. As a consequence the toner image is created on the PC. This process is called the jump process. The toner particles are finally transferred from the PC to the paper in the electric field of a second transfer corona. In the transfer processes the electric field force has to override the adhesion force. Unfortunately, this is not always the case. For example, the transfer from the PC to paper usually has an efficiency of approximately 90%, the rest of the toner has to be removed mechanically from the PC and disposed. This results in dissatisfying printing quality and in additional costs for waste management. This process is described in detail by Schein [3].

In order to improve this process it is necessary to understand the physical background of the process. The transfer of toner particles in the electrophotographic process can

be reduced to the fundamental phenomenon: The electric field force of the transfer corona outbalances the adhesion force between the particles and the substrates. The most important adhesion forces in this process are the van der Waals force, the electrostatic forces and in some case also the meniscus force [1, 5, 6]. However, these forces and their dependences on various parameters are still insufficiently understood. It is a major concern of this work to tailor the toner-substrate adhesion basing on a better understanding of the nature of the forces.

1.3 Structure of the thesis

In this study the essential forces determining the electrophotographic process are investigated systematically. The thesis is organized as followed:

Chapter 2 provides a brief overview of the most important adhesion forces in the electrophotographic process. Various models of the van der Waals force, the electrostatic force and the meniscus force are introduced.

In Chapter 3 a new model for the van der Waals force is derived by combining the Hamaker summation method with the Hertz model or FEM simulation for the prediction of particle deformation. The influence of the applied normal force, the material property as well as the roughness can be included into this model.

Chapter 4 describes particles and substrates with various material properties and roughness observed in this study. The methods applied to characterize the adhesion partners and to measure the adhesion force are introduced in this chapter as well.

The characterization of the particles and substrates is described in Chapter 5. The bulk and surface properties of the probes are investigated with various techniques to give a holistic view of the investigated materials.

The adhesion forces measured with various methods are presented in Chapter 6 along with model calculations. It is discussed in detail, how the adhesion force can be influenced by means of varying the properties of the adhesion partners and the measuring conditions. The comparison of the measuring results of various methods at different conditions shows the complexity of adhesion phenomena.

The results are summarized in Chapter 7, followed by an outlook concerning needs for the future research work.

2 FUNDAMENTALS OF ADHESION

Adhesion between particles and surfaces can be classified into two groups – with or without material bridges. The material bridge can be solid (through crystallization of a dissolved substance during drying, through hardening of a binder or sintering) or liquid (meniscus or viscous binder) [7]. Interactions without material bridges include the van der Waals force, the electrostatic force, and the interlocking of fibers. The most important adhesion forces occurring during the electrophotographic process are the van der Waals, the electrostatic, and possibly also the meniscus force. Various earlier referred works have discussed these different adhesion mechanisms [8-10]. Goel [1], Schein [3], and Williams [4] reviewed the relevance of these forces in the electrophotographic process, respectively.

2.1 Van der Waals forces

Van der Waals forces result from interactions between polar or polarizable atoms or molecules. The distance dependency of the van der Waals interaction energy approximately obeys the power law: $U(S) \propto S^{-6}$ in the non-retarded case. The interactions involved comprise the Keesom interaction (dipole–dipole), the Debye interaction (dipole–induced-dipole), and the dispersion interaction between non-polar atoms, also known as London interaction (induced-dipole–induced-dipole) [11]. The most important part of the van der Waals interactions is the dispersion interaction, which is always present. This interaction is of quantum mechanical nature. It is due to the fluctuating dipole moments. Non-polar atoms do not have permanent dipole moments but the atom nuclei and the respective electrons always constitute an instantaneous electric dipole moment u_1. The electric field of this dipole moment polarizes a neighboring atom of polarizability α and induces it with a dipole moment of strength $u_2 = \alpha u_1 / S^3$, where S is the distance between the atoms. The interaction energy between these atoms will be of order of $U \approx -u_1 u_2 / S^3 \approx -\alpha u_1^2 / S^6$ [12]. Hence, the fluctuating interaction energy is proportional to u_1^2. The mean value of the instantaneous dipole moment is $\langle u \rangle = 0$, while $\langle u^2 \rangle \neq 0$ [13], $\langle \cdot \rangle$ denotes the average in time. In vacuum or in air this interaction is always attractive. The dispersion interaction significantly contributes to many physical phenomena such as adhesion, physical adsorption, wetting, *etc*. Peukert *et al.* [14] showed that there is a close correlation between these phenomena. The dispersion interaction also has a strong impact on the properties of gases, liquids, and thin films as well as for the strength of molecular solids.

2.1.1 Van der Waals forces between rigid spherical bodies

The Hamaker model

Following the microscopic theory according to Hamaker [11], the dispersion energy between two bodies is the sum of the pairwise interaction energies of the molecules. Keesom and Debye interactions can also be included in the Hamaker constant. It should be noticed that the pairwise interaction energy between two molecules in interacting bodies is generally not the same as if they are isolated in free space. The presence of neighboring molecules alters the interaction energy normally around $\pm 20\,\%$ [8]. Furthermore, if the distance between the interacting molecules is so large that the time taken for the electric field of the first molecule to reach the second and return is comparable with the period of the fluctuation of the dipole (approximately $3 \cdot 10^{-16}\,s$), retardation of the dispersion interaction occurs. The dispersion energy decays faster than S^{-6}. In vacuum retardation begins at separations above $5\,nm$. The influence of the retardation effect on the dispersion force between bodies that are in direct contact, *i.e.*, $a = a_0 = 0.4\,nm$ [15] is therefore negligible.

To calculate the dispersion force between two bodies in contact Hamaker [11] integrated the pairwise dispersion energies between the molecules in the interacting bodies:

$$U_{vdW} = -\int_{V_1}\int_{V_2} \frac{C\rho^2}{S^{-6}} dV_1 dV_2, \qquad \text{Eq. 2.1}$$

where C is the London–van der Waals constant, ρ the number concentration of the molecules per unit volume, and S the distance between dV_1 and dV_2, which are the volume elements of the bodies with the volume V_1 and V_2, respectively. The influences of the many-body effect and the retardation effect are not included. For two rigid spherical particles with the radii R_1 and R_2 the dispersion energy is:

$$U_{vdW}(a) = -\frac{C\pi^2\rho^2}{12a} \cdot \frac{R_1 R_2}{R_1 + R_2} = -\frac{A}{12a} \cdot \frac{R_1 R_2}{R_1 + R_2}, \qquad \text{Eq. 2.2}$$

provided that R_1 and R_2 are much larger than the contact distance a (see Figure 2-1). $A = C\pi^2\rho^2$ is the Hamaker constant, which depends on the materials of the interacting particles.

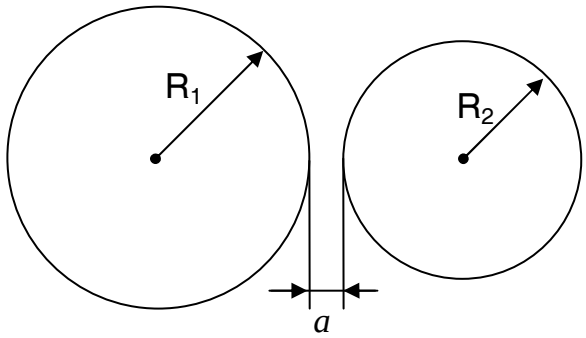

Figure 2-1 Contact geometry of two interacting spheres according to the Hamaker model.

The adhesion force is the derivation of the dispersion energy with respect to the separation distance a. The contact distance a_0 is around $0.4\,nm$ [16, 17]:

$$F_{vdW} = -\left.\frac{\partial U_{vdW}(a)}{\partial a}\right|_{a=a_0} = -\frac{A}{6a_0^2}\cdot\frac{R_1 R_2}{R_1+R_2}\,. \qquad \text{Eq. 2.3}$$

The negative value of the van der Waals force indicates that it is an attractive force. For particle–half space adhesion, *i.e.*, $R_2 \to \infty$, Eq. 2.3 reduces to:

$$F_{vdW} = -\frac{AR_1}{6a_0^2}\,. \qquad \text{Eq. 2.4}$$

Krupp [9] and Israelachvili [8], respectively, summarized the shortcomings of the microscopic theory:

1. The London–van der Waals constant, which refers to the interaction between free atoms or molecules in vacuum, is only known for a limited number of pairs of atoms or molecules.

2. The London theory of dispersion forces assumes that atoms and molecules only have a single ionization potential (one absorption frequency, namely the ionization frequency, typically $\nu_I \approx 3\cdot 10^{15}\,s^{-1}$). However, because of the interaction between the neighboring atoms (many-body effect), the material usually has a wide absorption spectrum. The spectra of the polarizability and the dielectric constant can be observed in the frequency range $10^{13} \sim 10^{16}\,s^{-1}$ (from infrared to ultraviolet).

3. The interacting bodies are assumed to be ideally non-conductive, the correlation of charge–carrier (electrons or holes) motion in each of the two solids is not accounted for.

4. It cannot handle the interaction of bodies in a solvent.

The Lifshitz theory

The macroscopic theory according to Lifshitz [18] is physically more satisfactory. This model completely avoids the problem concerning the additivity as present in the Hamaker model. The interacting bodies are treated as continuous media. The polarizabilities of the interacting atoms can be derived as functions of the bulk properties, such as the dielectric constants of the adhesion partners and the medium [12].

The Hamaker constant between interacting bodies 1 and 2 in medium 3 can be expressed for non-retarded interactions in terms of the complex dielectric constants:

$$A \approx \frac{3}{4} k_B T \left(\frac{\varepsilon_1 - \varepsilon_3}{\varepsilon_1 + \varepsilon_3} \right) \left(\frac{\varepsilon_2 - \varepsilon_3}{\varepsilon_2 + \varepsilon_3} \right) + \frac{3h}{8\pi^2} \int_{\nu_1}^{\infty} \left(\frac{\varepsilon_1(i\nu) - \varepsilon_3(i\nu)}{\varepsilon_1(i\nu) + \varepsilon_3(i\nu)} \right) \left(\frac{\varepsilon_2(i\nu) - \varepsilon_3(i\nu)}{\varepsilon_2(i\nu) + \varepsilon_3(i\nu)} \right) d\nu \,, \qquad \text{Eq. 2.5}$$

where ε_1, ε_2, and ε_3 are the static dielectric constants of the interacting bodies and the medium, respectively, $\varepsilon(i\nu)$ are the values of ε at imaginary frequencies ν. k_B and h refer to the Boltzmann and the Planck's constant.

The Hamaker constants derived from the Lifshitz model can be applied for different contact geometries (*e.g.*, sphere–sphere (Eq. 2.3) or sphere–half space (Eq. 2.4)) [8].

2.1.2 Van der Waals forces between deformable spherical bodies

An increase of the adhesion force due to the increase of the contact area has to be considered, if at least one of the adhesion partners is deformable. A detailed review of various models can be found in Tomas [19]. He identified four different cases: Those with pure elastic deformation, with plastic deformation, with viscoelastic, and with viscoplastic deformation.

2.1.2.1 Models considering elastic deformation

If the elastic deformation of the interacting particles and its influence on the adhesion force are investigated, the deformation in the contact region is always determined according to the Hertz theory [20] of 1882. Hertz investigated the deformation in the contact region of two smooth macroscopic linear-elastic spheres. The spheres are so large that the adhesion force between them is negligible. For two spheres of radii R_1 and R_2 pressed together with a normal force F_N, the contact radius r_C is given by:

$$r_C^3 = \frac{R}{K} F_N \,, \qquad \text{Eq. 2.6}$$

with $R = \frac{R_1 R_2}{R_1 + R_2}$ and $K = \frac{4}{3}\left(\frac{1-\nu_1^2}{E_1} + \frac{1-\nu_2^2}{E_2}\right)^{-1}$.

Herein R is the equivalent particle radius and K is defined as the elastic constant of the system. E and ν are the Young's modulus and the Poisson ratio of the materials, respectively. The centers of these two spheres approach each other by a distance of

$$\delta = \sqrt[3]{F_N^2 / \left(R K^2\right)} = r_C^2 / R \qquad \text{Eq. 2.7}$$

and the contact pressure distribution in the contact area is a function of the radius r:

$$\left(p(r) / p_0\right)^2 = 1 - \left(r / r_C\right)^2, \qquad \text{Eq. 2.8}$$

where $p_0 = 1.5 F_N / \left(\pi r_C^2\right)$ is the contact pressure in the center of the contact circle.

The JKR model

Johnson *et al.* [21] introduced a model describing the adhesion force between elastic particles in which they combined an energetic observation with geometric assumptions according to the Hertz theory. Hui *et al.* [22] were able to show by means of FEM-simulations that this geometric assumption is very accurate and that it holds true for contact partners with large contact radii.

Johnson *et al.* assumed an equilibrium between the mechanical energy U_M, the elastically accumulated energy U_E, and the surface energy U_S:

$$U_T = U_M + U_E + U_S = const.. \qquad \text{Eq. 2.9}$$

To calculate the different energies they constructed a fictive force–displacement route, as shown in Figure 2-2. The adhesion partners are loaded in two steps. In step 1 the surface force is neglected. The adhesion partners are loaded with a normal force, the force–displacement relationship obeys the Hertz theory until the contact radius r_C is reached. The normal force and the displacement are given by $\left(F_1, \delta_1\right)$. Step 2: keeping the contact radius constant at r_C, the normal force is gradually replaced by the surface force until the real status $\left(F_0, \delta_2\right)$ is reached.

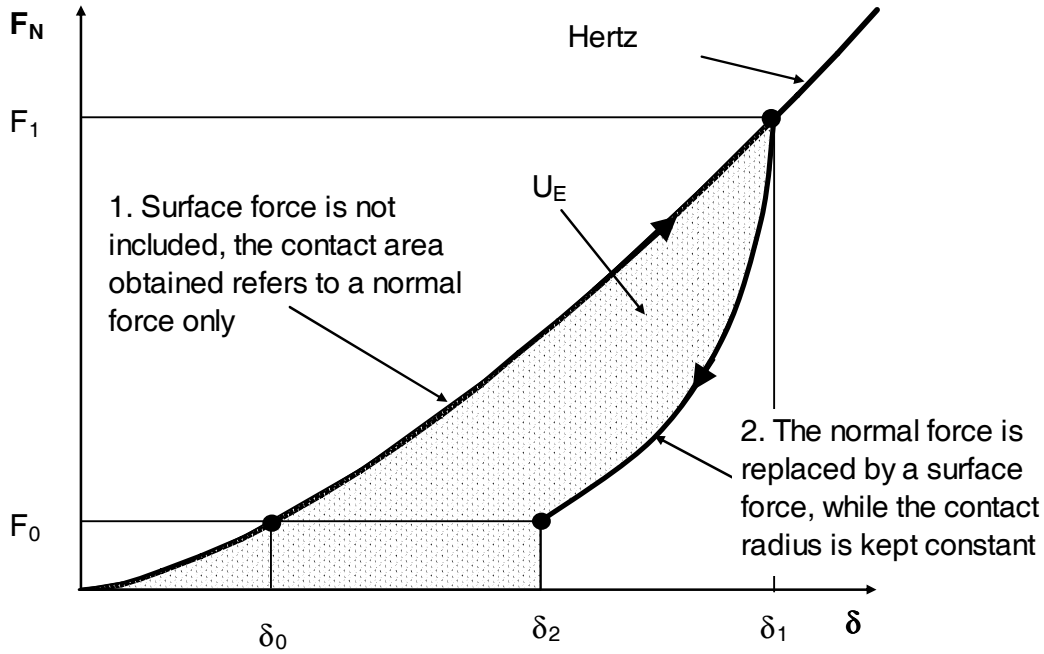

Figure 2-2 Elastic energy U_E as estimated by Johnson *et al.*.

The mechanical energy introduced by the external normal force is $U_M = F_0 \cdot \delta_2$. The surface energy is $U_S = \pi r_C^2 \cdot W$, where W is the work of adhesion. In case of adhesion between particles of the same material, the work of adhesion is twice the surface energy of the material: $W = 2\gamma$. The elastically accumulated energy U_E corresponds to the hatched area in Figure 2-2, it can be calculated as:

$$U_E = \frac{1}{K^{2/3} R^{1/3}} \left(\frac{1}{15} F_1^{5/3} + \frac{1}{3} F_0^2 F_1^{-1/3} \right), \qquad \text{Eq. 2.10}$$

the equivalent particle radius R and the elastic constant K are defined in the same way as in the Hertz model. Solving Eq. 2.9 or its derivation

$$\left. \frac{dU_T}{dr} \right|_{r_C} = 0 \qquad \text{Eq. 2.11}$$

leads to the following expression for the contact radius:

$$r_C^3 = \frac{R}{K} \left(F + 3\pi RW + \sqrt{6\pi RWF + (3\pi RW)^2} \right). \qquad \text{Eq. 2.12}$$

In contact the contact radius r_C remains real, *i.e.*, the term under the root sign is not less than zero. Thus the criterion for the separation is $6\pi RWF + (3\pi RW)^2 = 0$, and the adhesion force is

$$F_{adh} = -\frac{3}{2}\pi RW \ . \qquad \text{Eq. 2.13}$$

The DMT model

The DMT approximation [23] is valid for adhesion partners with high elastic constant K, so that assuming the normal force and the displacement to be equal to zero at the moment of separation is well justified. Equilibrium is established between the elastic energy and surface energy. According to this model the surface energy is:

$$U_S = W(a_0)\cdot \pi r_C^2 + 2\pi \int_{r_C}^{\infty} W(a) r dr \ , \qquad \text{Eq. 2.14}$$

where W is the interaction energy per unit area, which depends on the contact distance a. In contact $W(a_0)$ is defined in the same way as the work of adhesion W in the JKR model (Eq. 2.13). r is the radial coordinate and r_C is the contact radius (Figure 2-3). The first term of Eq. 2.14 refers to the surface energy within the contact area; the second term describes the interaction outside the contact area.

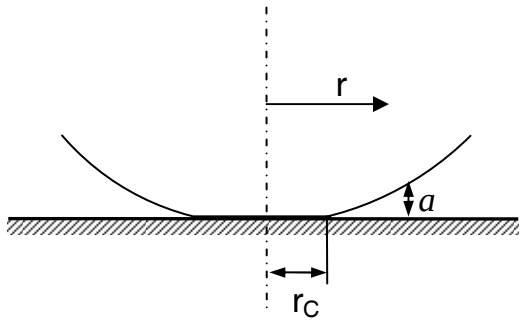

Figure 2-3 Contact geometry as in the DMT model.

Derjaguin *et al.* calculated the surface force by differentiating the surface energy with respect to the displacement δ: $F_S = dU_S / d\delta$. Separation takes place, when the deformation is recovered totally, *i.e.*, $r_C = 0$ and $\delta = 0$. The adhesion force is

$$F_{adh} = -2\pi RW \ . \qquad \text{Eq. 2.15}$$

The Tabor theory

Tabor [24] schematically compared the Hertz, the DMT, and the JKR model in terms of contact radius *vs.* normal force plots. If the adhesion force is negligible, the Hertz model can be applied. The contact radius r_C is then proportional to $F_N^{1/3}$.

If following the DMT theory the contact radius at a given normal force terms out to be larger than in case of the Hertzian approximation. This is because of the additional

deformation due to the adhesion force. For $F_N = 0$ the contact radius is $r_0 = \left(2\pi R^2 W / K\right)^{1/3}$ and the adhesion force is $F_{adh} = -2\pi RW$ as the contact radius reduces to zero.

According to the JKR model the contact radius is $r_0 = \left(6\pi R^2 W / K\right)^{1/3}$ and the adhesion force is $F_{adh} = -1.5\pi RW$. At this point a sudden Griffith crack [25] propagation like instability occurs and the surfaces separate abruptly.

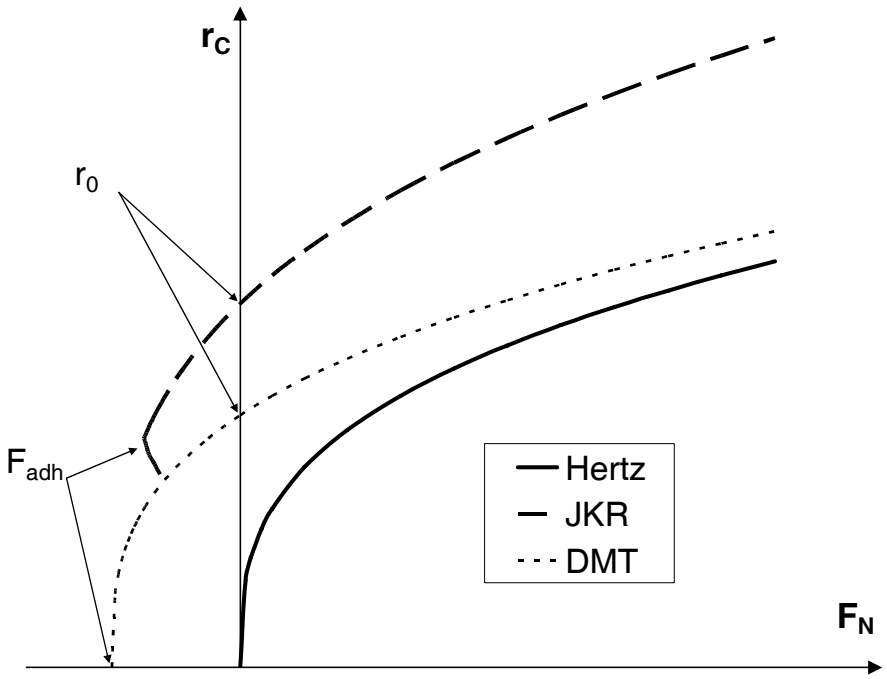

Figure 2-4 Contact between an elastic sphere and a flat rigid substrate according to the Hertz, the DMT, and the JKR model. r_0 is the contact radius at zero normal force and F_{adh} is the adhesion force predicted by each model.

Tabor concluded that a direct comparison between the JKR and the DMT model is meaningless since absolute values of the work of adhesion W in the JKR model and $W(a_0)$ in the DMT model cannot be directly compared. Furthermore, the adhesion is always affected by time-dependent factors.

The Maugis model

Maugis [26] compared the JKR and DMT approximations in terms of contact radius *vs.* normal force diagrams as well. In contrast to Tabor, Maugis suggested that the JKR and the DMT model are the limiting cases of a more general model. In the JKR model the interaction outside the area of contact is neglected while in the DMT model the influence of the adhesion force on the particle deformation is not taken into account. Maugis introduced a characteristic material coefficient λ:

$$\lambda = \frac{2\sigma_0 \big/ (K/R)^{2/3}}{(\pi RW)^{1/3}}, \qquad \text{Eq. 2.16}$$

where $\sigma_0 = 1.03W / a_0$ is the theoretical cohesive stress in the interacting area with a radius r_I. Usually this radius is larger than the contact radius r_0. a_0 is the contact distance, which is equal to the equilibrium separation of the atoms. K, W, and R are defined as in the JKR Model. The coefficient λ is a characteristic value of the material. For $\lambda \to 0$, the DMT limit is reached. Separation takes place when the contact radius reduces to zero. If $\lambda \to \infty$, the JKR limit is reached. Separation takes place when the Griffith instability is reached. In case of polymer particles, the Young's moduli are usually in the range of several GPa. The value of the coefficient λ lies in the range of 5 to 10. The adhesion force approaches the JKR limit which is $F_{adh} = -1.5\,\pi RW$. The Maugis model is supported by Johnson and Greenwood [27].

2.1.2.2 Models with non-elastic deformation

The Molerus model with purely plastic deformation

Molerus [28] assumed purely plastic deformation within the whole contact area. The contact radius r_C depends on the total force $F_T = F_N + F_{adh}$ acting on the contact area and on the Hertzian hardness p_{pl}^H of the material following the relationship:

$$F_T = p_{pl}^H \cdot \pi r_C^2 . \qquad \text{Eq. 2.17}$$

The Hertzian hardness p_{pl}^H is approximately three times larger than the yield stress σ_{yield}. Due to the flattening of the contact area the adhesion force increases to

$$F_{adh} = F_{adh,0} + \frac{A}{6\pi a_0^3 p_{pl}^H} \cdot F_N , \qquad \text{Eq. 2.18}$$

herein $F_{adh,0}$ is the adhesion force between the adhesion partners in the absence of particle deformation and can be calculated according to the Hamaker model (Eq. 2.3).

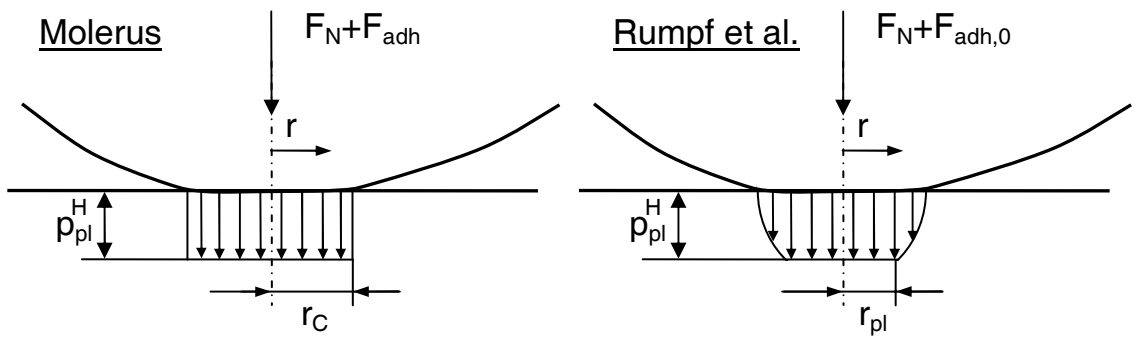

Figure 2-5 Pressure distribution in the contact region according to Molerus (left) and to Rumpf *et al.* (right). The plastic deformation is included in both models.

The Rumpf model with plastic deformation

Rumpf [29] *et al.* applied a linear elastic–purely plastic material model, *i.e.*, the material deforms elastically if the pressure is below the Hertzian hardness p_{pl}^{H}. When the Hertzian hardness is reached, further increase of the normal force causes the increase of the contact area, while the pressure remains constant at p_{pl}^{H} in the plastically deformed section of the contact area (Figure 2-5).

In the first step they calculate the adhesion force $F_{adh,0}$ between the particle and a flat rigid surface according to Hamaker (Eq. 2.4) as if the particle deformation does not occur. Then the particle deformation is estimated according to Hertz model (Paragraph 2.1.2.1) with a force which is equal to the sum of the normal force F_N and the adhesion force $F_{adh,0}$. If the maximum pressure p_0 in the center of the contact circle – it is calculated according to the Hertz theory – exceeds the Hertzian hardness p_{pl}^{H}, the plastically deformed range of the area is:

$$f_{pl} = \pi r_{pl}^2 = \frac{3}{2}\frac{F_N + F_{adh,0}}{p_{pl}^H}\frac{p_{pl}^H}{p_0}\left(1-\left(\frac{p_{pl}^H}{p_0}\right)^2\right), \qquad \text{Eq. 2.19}$$

and the adhesion force is:

$$F_{adh} = F_{adh,0} + p_{vdW} \cdot f_{pl}\,. \qquad \text{Eq. 2.20}$$

Here $p_{vdW} \cdot f_{pl}$ represents the van der Waals force acting between the plastically deformed particle section and the substrate. It is calculated according to the Hamaker model between a cylinder with the cross section f_{pl} and a half space: $p_{vdW} = A/\left(6\pi a_0^3\right)$.

The Rumpf model with viscoelastic and viscoplastic deformation

The Rumpf model which is valid for adhesion partners with plastic material properties can be extended to also account for materials with viscoelastic behavior [29]. In this model the material is described by means of the Maxwell model which consists of a series connection of a purely viscous damper with a viscosity η and a purely elastic spring characterized by the shear modulus G_0 at $t = 0$. The material function $K(t)$ (it replaces the elastic constant K in the Hertz model) is a function of the time t:

$$K(t) = \frac{32}{3}\left(\frac{t}{\eta} + \frac{1}{G_0}\right)^{-1}. \qquad \text{Eq. 2.21}$$

The adhesion force can be calculated as

$$F_{adh} = F_{adh,0} + p_{vdW} \cdot f_{vis}\text{, wherein} \qquad \text{Eq. 2.22}$$

$$f_{vis} = \pi r_{vis}^2 = \pi \left(\frac{R}{K(t)} \left(F_N + F_{adh,0} \right) \right)^{2/3} . \qquad \text{Eq. 2.23}$$

This model can be further extended to consider materials with viscoplastic deformation (sintering). If the influence of the surface tension is negligible, the contact area f_{vis} is proportional to the force $F_N + F_{adh,0}$:

$$f_{vis} = \pi r_{vis}^2 = \frac{2}{5} \left(F_N + F_{adh,0} \right) \cdot \frac{t}{\eta} . \qquad \text{Eq. 2.24}$$

Similar as in the viscoelastic model, the adhesion force can be calculated using Eq. 2.22.

The Tomas model with plastic or viscoplastic deformation

Tomas [19] showed the elastic-plastic yield and adhesion boundary in a load-displacement diagram (Figure 2-6). During the first loading procedure the loading curve follows the Hertz equation (Eq. 2.7) until the yield stress is reached in the center of the contact circle (point **Y** in Figure 2-6). Afterwards the loading curve follows a linear plastic yield boundary curve, which is described by the equation:

$$F_N = 2\pi R \, p_{pl}^H \delta , \qquad \text{Eq. 2.25}$$

where R is the equivalent particle radius (see Eq. 2.6), p_{pl}^H is the Hertzian hardness of the material and δ is the center approach of the both particles.

The adhesion boundary is calculated according to the Rumpf model with plastic deformation [29], the load-displacement behavior can be derived from Eq. 2.20 :

$$F_{adh,boundary} = F_{adh,0} + p_{vdW} \cdot f_{pl} = \frac{AR}{6a_0^2} \left(1 + \frac{2\delta}{a_0} \right). \qquad \text{Eq. 2.26}$$

The adhesion force is shown as a negative normal force in Figure 2-6. During unloading, for example, from the point **U**, the contact recovers elastically along an extended Hertzian parabolic curve to the point **A** where breakage takes places. The position of the the point **A** is calculated iteratively by:

$$\delta_{A,i+1} = \delta_U - \sqrt[3]{\delta_Y \cdot \left(\delta_U + \kappa \delta_{A,i} \right)^2} , \qquad \text{Eq. 2.27}$$

where κ is a coefficient, which denotes the irreversible particle contact stiffness. In case of plastic deformed adhesion partners, κ is equal to the slope of the line $F_{adh} = f(F_N)$.

Both unloading and reloading curve can be described with two extended Hertzian curve:

$$F_{N,unload} = \frac{2}{3} K \sqrt{R(\delta - \delta_A)^3} - F_{adh,A}, \qquad \text{Eq. 2.28}$$

$$F_{N,reload} = -\frac{2}{3} K \sqrt{R(\delta_U - \delta)^3} + F_{N,U}. \qquad \text{Eq. 2.29}$$

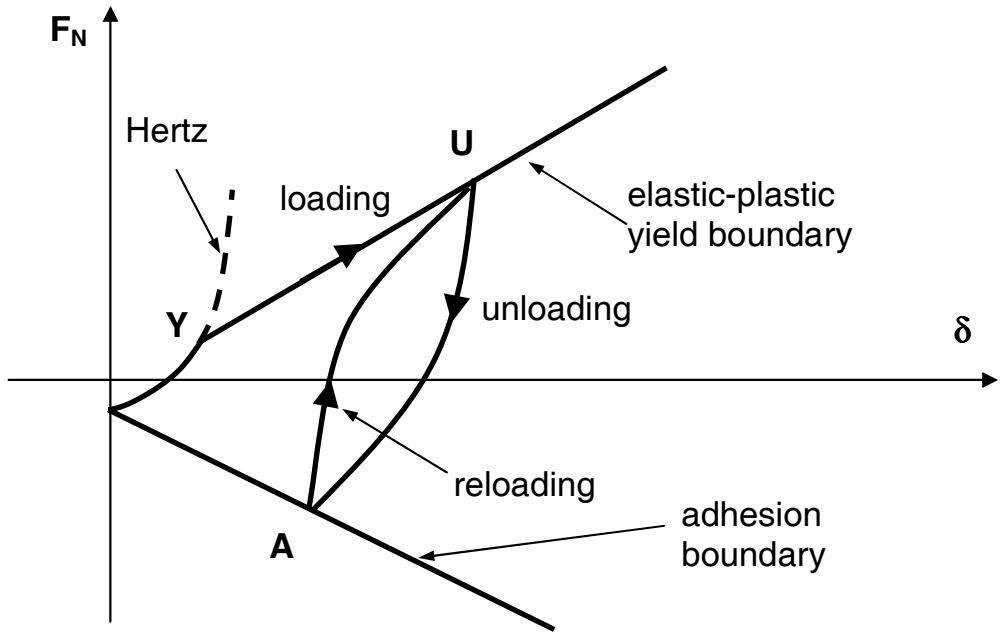

Figure 2-6 Load-displacement diagram according to Tomas [19].

Tomas [19] also extended this model for adhesion partners described by more sophisticated material laws (*e.g.*, viscoplastic and nonlinear elastic). More details about the implementation of these material laws in this model are not given in this work.

The Tomas model is one of the first which considers the loading and unloading procedures and their influence on the adhesion force. However, since the unloading behavior is still described by the Hertzian theory, which bases on the assumption that the particle shape is nearly spherical, the application of this model is limited.

2.1.3 Influence of surface roughness on the van der Waals forces

2.1.3.1 Van der Waals forces between rigid rough adhesion partners

The Rumpf model

In the Rumpf model [30, 31] dealing with rough adhesion partners the particle roughness is reduced to an asperity with half-spherical shape in the contact region, as

shown in Figure 2-7, left. The adhesion force is equal to the sum of the adhesion force between the smooth particle of radius R and the substrate in distance $a_0 + r$, and the adhesion force between the asperity and the substrate in distance a_0:

$$F_{vdW} = \frac{A}{6}\left(\frac{R}{(a_0 + r)^2} + \frac{r}{a_0^2}\right). \qquad \text{Eq. 2.30}$$

A is the Hamaker constant between the interacting bodies. Due to the roughness the adhesion force can be reduced by a factor of 100. If the size of the asperity is much smaller than the particle diameter, Eq. 2.30 can also be applied to predict the adhesion force between a smooth spherical particle and a rough substrate with a half-spherical asperity of radius r in the contact region.

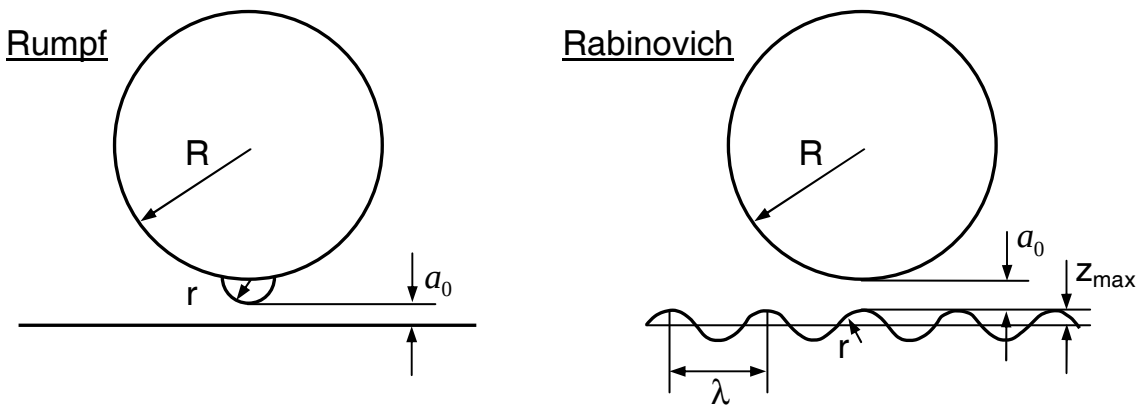

Figure 2-7 Contact geometry between rough adhesion partners according to Rumpf and to Rabinovich.

The Rabinovich model

Technical surfaces are usually characterized by irregular, *i.e.*, rough surfaces. Rabinovich [32, 33] investigated the surface profile of various probes by atomic force microscopy (AFM). He described the surface profile in terms of spherical asperities with centers below the average surface plane. The geometry of the asperities can be characterized with two parameters: the peak-to-peak distance λ and the maximal peak height z_{max} (Figure 2-7). The van der Waals force may then be calculated as:

$$F_{vdW} = \frac{AR}{6a_0^2}\left[\frac{1}{1 + 32R\,z_{max}/\lambda^2} + \frac{1}{(1 + z_{max}/a_0)^2}\right]. \qquad \text{Eq. 2.31}$$

The maximal peak height z_{max} is related to the root-mean-square roughness R_{rms} with $z_{max} = 1.817\,R_{rms}$. Both the λ and the R_{rms} value can be measured with various methods, *i.e.*, AFM or white light interference microscope (WLIM) [34].

Adhesion force distributions on rough surfaces

Actually, the previously described models refer to the values of the minimal adhesion force between a particle and a rough substrate since no more than the interaction between the particle and a single asperity is calculated and because the distance between the particle and the flat substrate reaches its maximum. Götzinger and Peukert [35] randomly varied the contact position and obtained adhesion force distributions for different contact geometries. For example, in case of a smooth spherical particle and a substrate coated with mono-disperse spherical nano-particles in a simple cubic arrangement the adhesion force distribution follows the shape of a Weibull-function [36] with the cumulative frequency function:

$$P(F_{adh}) = 1 - exp\left[-0.693\left(\frac{F_{adh} - F_{adh,min}}{F_{adh,50} - F_{adh,min}}\right)^n\right], \qquad \text{Eq. 2.32}$$

where $F_{adh,min}$ is the minimal adhesion force, which is approximately equal to the prediction of the Rumpf model, $F_{adh,50}$ denotes the force at the probability $P(F_{adh,50}) = 50\%$, the exponent is $n = 1.2$.

Götzinger and Peukert also identified two other types of adhesion force distributions: bimodal Weibull distributions for the case of a rough particle in contact with a substrate coated with mono-disperse spherical nano-particles and logarithmic normal distributions for the case of a rough particle in contact with a randomly rough substrate.

The relocation effect [37]

The contact situation as shown in Figure 2-7 is not stable. Even a very small force F may – together with the supporting force F_{sup} of the substrate – build a significant moment so that the particle may relocate to a more stable position (Figure 2-8). In the electrophotographic process this force may be the electrostatic force or the inertia. The presence of several contact points between the particle and the substrate increases the adhesion force accordingly.

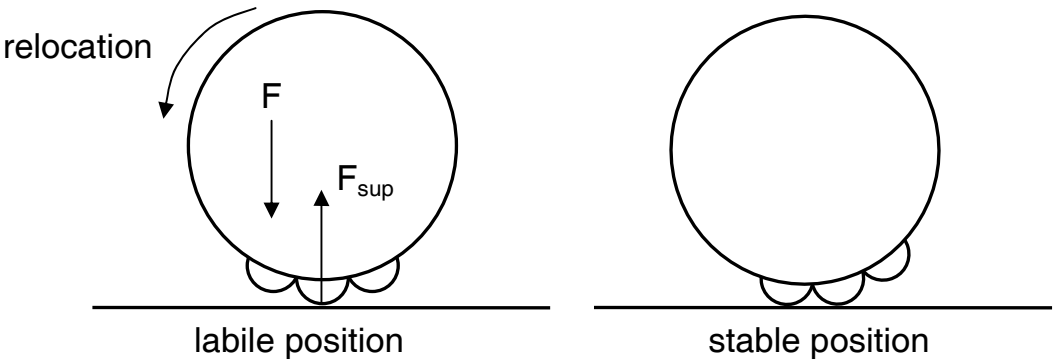

Figure 2-8 Relocation of a rough particle to a stable position

2.1.3.2 Van der Waals forces between deformable rough adhesion partners

The nano-scale asperities may be plastically deformed because of the high contact pressure produced by the normal force and the adhesion force. The flattening of the asperities causes an increase of the contact area between this asperity and the substrate (Figure 2-9 B) [37]. Its influence on the adhesion force can be predicted by the non-elastic models (Molerus or Rumpf, Paragraph 2.1.2.2). However, as the distance between the interacting surfaces reduces because of the flattening of the asperities, more asperities get in contact with the substrate (Figure 2-9 C). This then leads to an increase of the adhesion force. This phenomenon continuously occurs, until equilibrium is reached. The overall increase of the adhesion force due to the flattening of the asperities may in fact be significant.

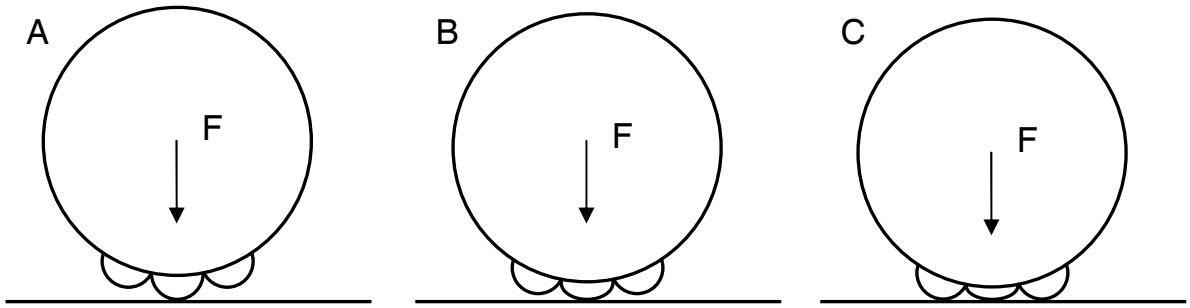

Figure 2-9 Increase of the contact area due to the flattening of the rough particle.

2.1.4 Influence of the oxide/adsorbate layer on the van der Waals force

If surfaces are exposed to the ambience, they may oxidize and moisture may adsorb on them. The oxide (adsorbate) layers usually have Hamaker constants which differ from those of the bulk materials. Langbein [38] concluded that these layers do not only act as a spacer, but cause an additional screening of the reaction field also. As Lifshitz has shown in this approach (Paragraph 2.1.1), the interaction energy is a complex function of the frequency dependent dielectric constants of the bulk materials and the oxide (adsorbate) layers. Its value is normally smaller than the interaction energy in the absence of such layers. The van der Waals force resulting from the interaction between two identical flat surfaces (index 1) each covered with an adsorbate layer (index 2) of thickness T reduces to [8]:

$$\frac{F_{vdW}}{A_C} = \frac{1}{6\pi}\left(\frac{A_{232}}{a_0^3} - \frac{2A_{123}}{(a_0+T)^3} + \frac{A_{121}}{(a_0+2T)^3}\right), \qquad \text{Eq. 2.33}$$

here A_C is the contact area. The index 3 denotes the medium between the adhesion partners. The calculation of the Hamaker constants A_{ikj} between materials i and j in a medium k can be found in the book of Israelachvili [8].

2.2 Electric forces

2.2.1 Particle charging processes

In the electrophotographic process the charging of the particles can be due to different mechanisms, *i.e.*, the transfer of the electrons, of the ions or of material [39].

2.2.1.1 Charging of the toner particle in the developing process

In the developing process the toner-carrier mixture is intensively agitated (see Section 1.2). The particles impact upon each other and experience friction amongst each other.

If two metal surfaces with different work functions are in contact with each other, electrons flow from the part with the lower work function, *i.e.*, higher filled energy level, to the part with higher work function, until the energy levels are equalized [39, 40]. The metal surface with lower work function therefore becomes positively charged while the metal surface with the higher work function turns out to be negatively charged. The assumption of an equal surface energy levels on the whole surface can be applied to metals, but it is not valid for insulators. Various publications [41, 42] suggest that there are local surface energy levels in the band gap because of lattice failures or impurities. The distribution of these inhomogeneities is random, which explains why the values of the measured work functions of insulators widely scatter.

The mechanism of friction charging (triboelectric charging) is even more complicated than the one of contact charging. If a protuberance of a surface rubs over another surface, its temperature can increase significantly. It may then emit electrons and adopt a positive charge. It is usually found that the amount of charge transferred is affected more by the energy of the rubbing than by the nature of the materials involved. High local temperatures as obtained from triboelectric charging may hence result in high charge densities. Also material transfer typically takes place between the friction partners. Charges can be transferred together with the material.

The local charge density is limited by the local breakdown field strength, which is $E_B = 3 \cdot 10^6 \, V/m$ in case of negative charge in dry air, and the maximal charge density is:

$$\sigma_{max} = E_B \cdot \varepsilon_0 \varepsilon_r = 2.66 \cdot 10^{-5} \, C/m^2 , \qquad \text{Eq. 2.34}$$

ε_0 and ε_r are the permittivity of the free space and the dielectric constant of the particle material, respectively.

The maximal charge density can be altered by the relative humidity: In case of relative humidities $\phi < 40\%$ any increase of ϕ results in a significant decrease of the surface charge gained by friction. This is because of the reduction of the breakdown field

strength E_B in the humid air. At higher relative humidities this influence is minor [43].

The surface charge on toner particles obtained through friction is strongly localized. Hays [44] estimated a surface charge coverage of only several per cent and the charge density in the patches can be approximately observed as constant.

2.2.1.2 Charging of the toner particle in the jumping process

In the jumping process (see Section 1.2) the toner particles are exposed to a combined electric field provided by an alternating voltage $\tilde{U}_{AC}$ and a bias voltage U_{DC} between the electrodes. The particles can be charged through ion charging, *i.e.*, immobilization of the free ions in the air [45] and through conductive charging on the electrode [5].

Pauthenier and Moreau-Hanot developed the well accepted field charging theory in 1932 [46, 47]. They investigated the equilibrium charge Q_{eqm} and the kinetic of the charging process in a DC electric field $E = U_{DC}/d$:

$$Q_{eqm} = \left(1 + \frac{2(\varepsilon_r - 1)}{\varepsilon_r + 2}\right)\frac{4\pi\varepsilon_0 E R^2}{e}, \qquad \text{Eq. 2.35}$$

and the charging rate at the time t is:

$$\frac{dQ(t)}{dt} = \frac{e\rho_i\mu_i Q_{eqm}}{4\varepsilon_0}\left(1 + \frac{Q(t)}{Q_{eqm}}\right)^2, \qquad \text{Eq. 2.36}$$

where R is the radius of the particle, e is the elementary charge. ρ_i and μ_i are the ion concentration in the ambience and the electrical mobility of the ions, respectively.

Hays and Feng [45] investigated the charging of toner particles in air through an alternating electric field. The maximal Q/M -ratio of the toner charged in a field with peak field strength $|E_{max}| = \left(|\tilde{U}_{AC,max}| + |U_{DC}|\right)/d$ is:

$$(Q/M)_{max} = \frac{9\varepsilon_0 E_{max}}{\rho R}\frac{\varepsilon_r}{\varepsilon_r + 2}, \qquad \text{Eq. 2.37}$$

here ρ stands for the density of the particle material. Usually the particles are charged negatively through ion charging in an alternating electric field. The particle charge obtained from ion charging is proportional to the electric field strength E and to the applied voltages $\tilde{U}_{AC}$ and U_{DC}.

Because of the inhomogeneity of the toner particle, especially on the particle surface, a certain conductivity of the particle can always be observed. This conductivity can be enhanced by mixing Charge Control Agents (CCA) to the toner particle [42, 48, 49]. The CCA are in our case ionic compounds with anions bound to polymer chains,

while the cations can move freely. The free cations contribute significantly to the surface conductivity of the toner. All the authors observed that the particle charge obtained through triboelectric charging decreases when the amount of the CCA is increased.

2.2.2 The electric forces

2.2.2.1 General consideration

In the electrophotographic process the important electric forces are the electric field force and the electrostatic force. The electrostatic force between a charged particle and a substrate can be approximately described with the image force model, *i.e.*, the attraction between the particle charge and its image in the substrate [6].

In the case of a uniformly charged dielectric spherical particle with a total charge Q resting on a smooth substrate in a uniform electric field E the electric forces can be generally described in three terms [44]:

$$F_e = -c_1 \frac{Q^2}{16\pi\varepsilon_0 R^2} + c_2 QE - c_3 \pi\varepsilon_0 R^2 E^2 . \qquad \text{Eq. 2.38}$$

The second term is the electric field force, which contributes to remove the particle from the substrate. The first and the third term refer to the so-called image force of the particle charge and the polarization in the electric field, respectively. If a charged or a polarized particle is in contact with a substrate, the atoms of the substrate located in the electric field of the particle are polarized, so that an image of the original particle charge is created. The image force is the electrostatic force between the charged or polarized particle and its image in the substrate. These two terms refer to the most important adhesion forces in the electrophotographic process beside the van der Waals force. Feng and Hays [50] defined the coefficients c_i as functions of the dielectric constants of the adhesion partners $\varepsilon_{r,particle}$ and $\varepsilon_{r,substrate}$, the thickness of the substrate, and the spacing between the electrodes. They carried out FEM-simulations to predict the values of the coefficients for different boundary conditions.

2.2.2.2 The electrostatic force as a function of the contact distance

Matsuyama and Yamamoto [51] investigated the distance dependence of the electrostatic force between a uniformly charged particle and a conductive substrate by means of Legendre functions. The charge density on the particle surface is $\sigma = Q/(4\pi R^2)$. The electric field and the field forces are not included in this model. The image force between a spherical dielectric particle and a flat conductive substrate separated by the distance a is:

$$F_e = -\frac{Q^2}{16\pi\varepsilon_0 R^2} \cdot 4\sum_{k=0}^{\infty}(k+1)A_k B_{k+1}, \qquad \text{Eq. 2.39}$$

where A_k and B_{k+1} are the coefficients of the Legendre function of the first kind. This equation has to be solved numerically for each $\varepsilon_{r,particle}$ and a. To reduce the effort of calculation, they have also given an empirical approximation based on the numerical calculation:

$$F_e = -\frac{\gamma}{\left(1+(a/R)^{\alpha}\right)^{\beta}} \cdot \frac{Q^2}{16\pi\varepsilon_0 R^2}, \qquad \text{Eq. 2.40}$$

where the parameters α, β and γ are functions of the particle dielectric constant $\varepsilon_{r,particle}$:

$$\begin{aligned}\gamma = {} & 0.721 + 0.261\varepsilon_{r,particle} + 1.220\cdot 10^{-2}\,\varepsilon_{r,particle}^2 - 1.207\cdot 10^{-4}\,\varepsilon_{r,particle}^3 \\ & + 1.402\cdot 10^{-6}\,\varepsilon_{r,particle}^4 - 9.45\cdot 10^{-9}\,\varepsilon_{r,particle}^5 + 2.63\cdot 10^{-11}\,\varepsilon_{r,particle}^6\end{aligned}, \qquad \text{Eq. 2.41}$$

$$\begin{aligned}\alpha = {} & 1.146 - 0.165\varepsilon_{r,particle} + 2.116\cdot 10^{-2}\,\varepsilon_{r,particle}^2 - 1.749\cdot 10^{-3}\,\varepsilon_{r,particle}^3 \\ & + 8.711\cdot 10^{-5}\,\varepsilon_{r,particle}^4 - 2.37\cdot 10^{-6}\,\varepsilon_{r,particle}^5 + 2.68\cdot 10^{-8}\,\varepsilon_{r,particle}^6\end{aligned}, \text{ and} \qquad \text{Eq. 2.42}$$

$$\beta = 2 + log_2\,\gamma\ . \qquad \text{Eq. 2.43}$$

In contact the image force $F_e\big|_{a=0}$ is equal to:

$$F_e\big|_{a=0} = -\gamma \cdot \frac{Q^2}{16\pi\varepsilon_0 R^2}\ , \qquad \text{Eq. 2.44}$$

which is identical to the result of the image force model (Eq. 2.38) at $E = 0$.

2.2.2.3 The influence of the local charge density and the particle shape

The toner particles in the electrostatic process are not perfectly spherical and the charge is usually not uniformly distributed on the surface, depending on the material property and the way it is charged. For example, charges gained by impact or friction exist usually as charge patches [52-54]. The non-uniform charge distribution has a significant influence on the adhesion force. According to Hays [44] the patches near the substrate dominate the electrostatic force. This part of the charge may be $P \approx 20\%$ of the total particle charge. The charge density on the patches σ ranges from 0.5 to $5mC/m^2$. The electrostatic force between such a particle and a flat conductive surface in contact is:

$$F_e = -\frac{QP\sigma}{2\varepsilon_0}. \qquad \text{Eq. 2.45}$$

Rimai [5] discussed the influence of the localized charge patches on the adhesion force. In comparison to a uniformly charged particle with the same amount of charge the particle with charge patches may show stronger electrostatic adhesion to the substrate. Schein [55] studied the influence of charge localization by means of numerical calculations and came to the same conclusion. Nevertheless, since the local charge density is limited by the air breakdown field strength, this force cannot exceed the range of several $100\,nN$.

2.2.2.4 The influence of the neighboring particles

If there is a layer of charged particles on the substrate, each of these particles induces its own image charge in the substrate. If a particle now interacts with the total image charge of the whole particle collective, the image force can increase by a factor of 10 for a hexagonal close-packed monolayer [56].

2.3 The meniscus force

If the adhesion partners are exposed to the ambient atmosphere which usually contains a certain degree of humidity, they turn out to be covered with water molecules. These condensed water molecules may affect the adhesion force in a rather complex way.

At first, the water layer screens the van der Waals interaction between the bulk materials (Paragraph 2.1.4) and increases the surface conductivity (Paragraph 2.2.1.1). For $A_{solid} > A_{liquid}$, this layer causes the reduction of the van der Waals force and of the electrostatic force. On the other hand, the water molecules build a meniscus in the contact region. To separate the adhesion partners, it is necessary to overcome the meniscus force [8] also. In this case, the adhesion force is the sum of the van der Waals force, the electrostatic force, and the meniscus force.

The condensation of water vapor in the contact region between a spherical particle with the radius R and a flat substrate is related to the relative humidity $\phi = p / p_s$ by the well-known Kelvin equation [8]:

$$\left(\frac{1}{r_1} + \frac{1}{r_2}\right)^{-1} = \frac{V \cdot \gamma \cos\theta}{\Re T \ln(\phi)}. \qquad \text{Eq. 2.46}$$

here $\Re = 8.31\,J/(mol \cdot K)$ is the gas constant and T is the ambient temperature. The surface tension and the molar volume of water are $\gamma = 0.072\,J/m^2$ and $V = 1.8 \cdot 10^{-5}\,m^3/mol$, respectively. r_1 and r_2 are the principal radii of the meniscus. r_1 is negative because the curvature is concave, $r_1 = -|r_1|$. It is assumed that the

contact angle of water on the substrate is equal to the contact angle on the particle surface $\theta_1 = \theta_2 = \theta$. The geometry of the meniscus is shown in Figure 2-10.

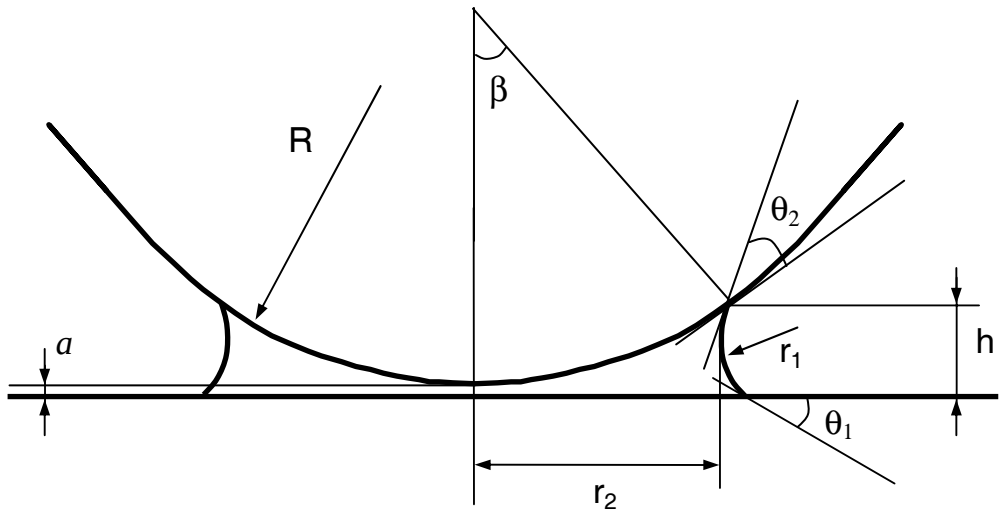

Figure 2-10 Geometry of a meniscus between a rigid spherical particle and a flat substrate.

If $|r_1| << r_2 << R$, *i.e.*, the meniscus is limited to a small region, the meniscus can approximately be seen as a triangle in the 2D projection. The relationship between r_1 and r_2 can be derived from

$$r_2 \approx \sqrt{R^2 - (R-h)^2} = \sqrt{2Rh - h^2} \approx \sqrt{2Rh} \text{ and } h \approx -2r_1 \cos\theta : \qquad \text{Eq. 2.47}$$

$$r_2 \approx \sqrt{-4r_1 R \cos\theta} \qquad \text{Eq. 2.48}$$

for the case of a small embracing angle β. The geometry of the meniscus in dependence of the relative humidity ϕ is obtained from solving Eq. 2.46 and Eq. 2.48. The meniscus force between the particle and the substrate consists of two parts, one part is because of the Laplace pressure in the meniscus and the second part is the surface force at the weakest position, *i.e.*, the neck of the meniscus with the radius r_2. Therefore the total meniscus force is:

$$F_m = F_{Lap} + F_S = -\pi r_2^2 \gamma \left(\frac{1}{r_1} + \frac{1}{r_2} \right) + 2\pi r_2 \gamma \approx -\frac{\pi r_2^2 \gamma}{r_1} + 2\pi r_2 \gamma . \qquad \text{Eq. 2.49}$$

Usually, the second term is significantly smaller than the first term, so that it can be neglected. Substituting Eq. 2.48 in Eq. 2.49 simplifies this expression to:

$$F_m = 4\pi R \gamma \cos\theta . \qquad \text{Eq. 2.50}$$

Farshchi-Tabrizi *et al.* [57] provided a more precise model for the meniscus force between a spherical particle and a smooth substrate:

$$F_m = 2\pi R\gamma \sin\beta\left[\sin(\beta+\theta) - \frac{R}{2}\sin\beta\cdot\left(\frac{1}{r_1}+\frac{1}{r_2}\right)\right], \qquad \text{Eq. 2.51}$$

the principal radii of the meniscus r_1 and r_2 are also calculated according to Kelvin (Eq. 2.46). However, the angle β is considered as a variable in this paper, the dependence of β on the relative humidity ϕ is not given.

Meanwhile, the formation of the meniscus between the particles results in the reduction of the van der Waals force, since the Hamaker constant for a solid interaction across the air A_{sgs} (solid-gas-solid) is typically 5 to 10 times higher than which across the liquid water A_{sls} (solid-liquid-solid). The van der Waals force reduces to:

$$F_{vdW} = -\frac{A_{sls}-A_{sgs}}{6R}\frac{a/R+1-2\cos\beta}{(a/R+1-\cos\beta)^2} + \frac{A_{sls}}{6R}\frac{a/R-1}{(a/R)^2} - \frac{A_{sgs}}{6R}\frac{1}{a/R+1}. \qquad \text{Eq. 2.52}$$

2.3.1 The dependence of the meniscus force on the contact distance

If the adhesion partners are separated, the meniscus is deformed before it finally breaks. Stifter *et al.* [58], Rabinovich *et al.* [59], and Li *et al.* [60] studied the distance dependence of the meniscus force based on the assumption of a constant meniscus volume, respectively. Since the separation takes place very quickly, the volume of the meniscus remains approximately unchanged until breakage.

Rabinovich *et al.* [59] investigated the change of the meniscus geometry and its influence on the meniscus force, if the distance between the adhesion partners is increasing. The meniscus force is:

$$F_m = \frac{4\pi R\gamma\cos\theta}{1+a/(h-a)} + 2\pi\gamma R\sin\beta\sin(\beta+\theta), \qquad \text{Eq. 2.53}$$

where γ is the surface tension of water. The definitions of the geometry can be found in Figure 2-10. For a certain value of the meniscus volume V the maximal height of the meniscus is $h=\sqrt{a^2+V/(\pi R)}$ and the relationship between the embracing angle β and the meniscus volume V is:

$$\beta^2 = \frac{2a}{R}\left(-1+\sqrt{1+\frac{V}{\pi R a^2}}\right). \qquad \text{Eq. 2.54}$$

Li *et al.* [60] compared the two extreme cases of the meniscus force between a cylinder and a flat surface. If the adhesion partners are separated rapidly, the volume of the meniscus remains constant. The meniscus force does not fall monotonously

with the separation distance, the maximal meniscus force is slightly larger than the meniscus force in contact. If separation progresses very slowly, equilibrium can always be maintained. The geometry of the meniscus can always be calculated with the Kelvin equation (Eq. 2.46). In this case, the meniscus force falls monotonously with the distance. The reality is somehow between these two extreme cases.

2.3.2 The meniscus force between rough adhesion partners

Ata *et al.* [61] studied the influence of the roughness on the meniscus force. They assumed there is a hemispherical asperity in the contact region. If the principal radius r_1 calculated with Eq. 2.46 is smaller than the half of the radius of the asperity r, the meniscus is built between the asperity and the particle, and the meniscus force is:

$$F_m = 4\pi r \gamma \cos\theta , \qquad \text{Eq. 2.55}$$

while in the case of $r_1 > 2r$, the meniscus fills the gap between the particle and the substrate. The meniscus force is then:

$$F_m = 4\pi R \gamma (1 - r/(2r_1)) \cos\theta . \qquad \text{Eq. 2.56}$$

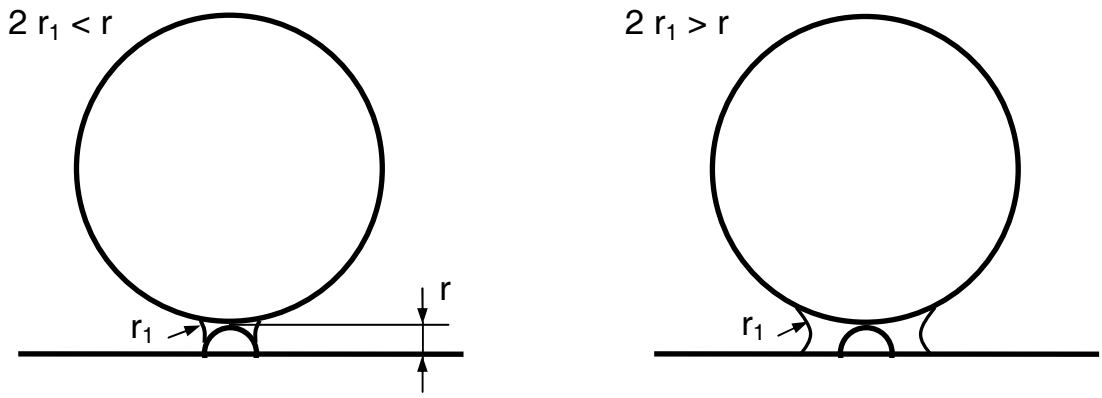

Figure 2-11 Schematic diagram of the meniscus between rough adhesion partners.

If the planar surface is covered by a layer of mono-disperse spherical asperities in the range of several nm, and the distance between the asperities is sufficiently small, so that it is possible that the particle builds menisci with several neighboring asperities. Farshchi-Tabrizi *et al.* [57] modeled the meniscus force in this case. They assumed that the particle is coaxially in contact with one asperity. The distances between the neighboring asperities and the particle can be calculated from the geometric data. As soon as the distances is smaller than meniscus thickness h (see Eq. 2.47), meniscus is built between them, this gives a rise to the meniscus force. For example, a $10\,\mu m$ particle is in contact with a surface covered with densest packed $10\,nm$ spherical asperities, the distance between the particle and the first ring of 6 neighboring asperities is $0.411\,nm$. Assuming that the contact angle is $\theta = 0°$, the menisci can be

built at a relative humidity of 7.9%. According to Eq. 2.55 the meniscus force suddenly increases by a factor of 7 from $4.5\,nN$ to $31.7\,nN$. Bocquet and Barrat (in Butt *et al.* [62]) suggested that formation of the small menisci between the particle and surface asperities may finally fill the pores between the asperities and result in one large meniscus. So they derived a humidity and time-dependent menicsus force:

$$F_m = \gamma a \frac{\ln(t/\tau_0)}{\ln(\phi)}, \qquad \text{Eq. 2.57}$$

where a is the distance between the adhesion partners and τ_0 is a time constant of the order of the time needed to condense one liquid layer.

2.3.3 The viscous force

Because of the viscosity of the meniscus, an additional viscous force arises, which is related to the pressure generated in the meniscus resulting from the relative displacement of the adhesion partners [63].

This force is

$$F_{vis} = \frac{2}{3}\pi\eta R^2 \left(1 - \frac{a}{a + r_2^2/R}\right)^2 \frac{1}{a}\frac{da}{dt}, \qquad \text{Eq. 2.58}$$

where η is the dynamic viscosity of the meniscus, R is the particle radius and a is the distance between the adhesion partners. The diameter of the meniscus r_2 is given by Eq. 2.48.

Usually this force is significantly smaller than the meniscus force, if the meniscus consists of water. However, in case of a meniscus built through capillary condensation, the meniscus has a thickness of merely several nm. The water molecules in the meniscus strongly interact with the particle and the substrate surface, so that the viscosity of the meniscus is much higher than in the bulk. The viscous force may be no more negligible.

2.4 Comparison of the adhesion forces

We compare the distance dependency of the van der Waals force, the electrostatic and the meniscus forces in Figure 2-12. The van der Waals forces are calculated according to the Rumpf model (Paragraph 2.1.3.1). Here the particle size is $R = 5\,\mu m$, the Hamaker constant is $A = 6.6 \cdot 10^{-20}\,J$. The asperity radii are stated in the diagram.

The electrostatic force is a long-range force in comparison to the van der Waals force. In this diagram the electrostatic force is calculated according to Matsuyama

(Paragraph 2.2.2.2). For toner particles the dielectric constant is approximately $\varepsilon_{r,particle} \approx 4$. Accordingly, the value of coefficients are $\alpha = 0.73$ and $\beta = 2.97$. Three curves with different amount of charge are shown in the diagram.

The meniscus force is calculated according to Rabinovich (Paragraph 2.3.1). It is assumed that the meniscus volume is $2 \cdot 10^5\, nm^3$, which is approximately the volume of the meniscus water between a $10\,\mu m$ particle and a flat substrate if equilibrium is reached at 50% relative humidity.

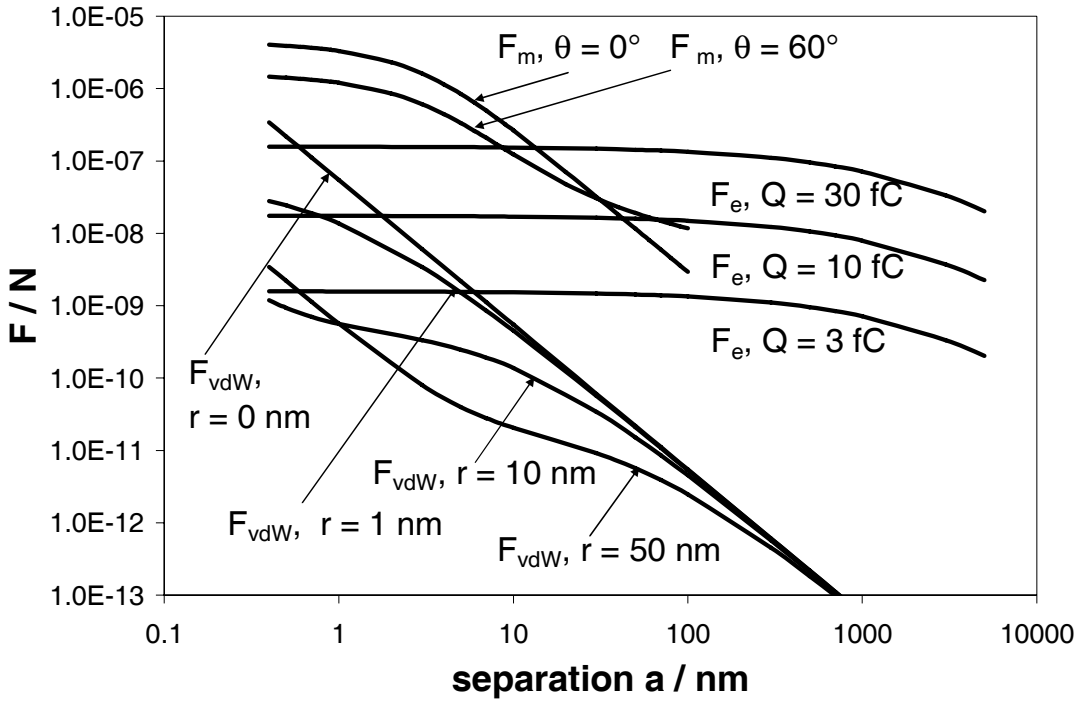

Figure 2-12 Comparison of the distance dependence of the van der Waals forces, the electrostatic forces and the meniscus forces.

3 MODELING OF THE VAN DER WAALS FORCE [64]

3.1 The analytical approach

3.1.1 Comments on the approaches based on energy balances

For the estimation of the adhesion force between deformable adhesion partners, approaches based on energy balances (JKR, DMT, and Maugis, Paragraph 2.1.2.1) are always applied, in which the adhesion force is calculated through an energy balance between the mechanical energy and the surface energy [26]. In this manner the Hamaker summation of the complicated geometry after deformation can be avoided, so that this problem can be solved analytically.

The JKR model [21] as an example, assumes a balance between the mechanical energy, the elastically accumulated energy, and the surface energy. The elastically accumulated energy U_E depends not merely on the start and the end positions in the force-displacement plot; it also depends on the exact route of the force-displacement curve. Unfortunately, the construction of the exact route of the force-displacement curve is not possible in the JKR model, because the surface force is not implicitly defined as a function of the displacement δ. Johnson *et al.* chose a route, in which the particle deforms according to the Hertz theory until it reaches the expected contact area with a physically not defined normal force F_1. This force is then replaced by the surface force while the contact area remains constant. This approach causes an overestimation of the elastically accumulated energy U_E.

In the DMT-model, the surface force is calculated by differentiating the surface energy with respect to the displacement δ and not to the contact distance a. Nevertheless, the adhesion force should be the force needed to enlarge the separation between the adhesion partners. Simply consider two flat surface in contact, the contact area remains constant while the displacement varies with the normal force. According to Derjaguin *et al.* [23] the surface energy is a constant and the surface force is zero until separation takes place. Obviously, a reasonable expression for the surface force should be

$$F_S = dU_S / da\Big|_{a = a_0} . \qquad \text{Eq. 3-1}$$

For approaches based on energy balances, a further principal problem is to decide when separation occurs. In these models the criteria of separation are not always straightforward (see Paragraph 2.1.2.1). Hence, a physically more reliable model is developed in the frame of this work, which bases on the Hamaker theory (see

Paragraph 2.1.1). The Hamaker summation of the deformed adhesion partners is carried out numerically. To illustrate the modeling strategy, in the following an analytical model with purely elastic deformation based on Hertz theory is presented at first.

3.1.2 Assumptions of the new model

It is assumed that the adhesion partners are brought into contact very slowly, so that at every moment the equilibrium between the three energy terms, the mechanical energy of the applied normal force, the elastically acummulated energy and the dispersion interaction energy, is maintained. The term "dispersion interaction energy" is used instead of the surface energy in the JKR model (Paragraph 2.1.2.1), so that the interaction energy outside of the contact area may also be included. The deformation of the soft particle depends on the sum of the normal force F_N and the dispersion force F_D. For convenience this force is defined as the total normal force:

$$F_T = F_N + F_D . \qquad \text{Eq. 3-2}$$

In the analytical model the relationship between the total normal force and the particle deformation is described with the Hertz model.

The dispersion interaction energy can be calculated using the Hamaker summation method [8]:

$$U_D = \pi r^2 \cdot \frac{A}{12\pi a_0^2} , \qquad \text{Eq. 3-3}$$

where r is the contact radius. The dispersion force F_D is obtained from the derivation of the dispersion interaction energy with respect to the contact distance a:

$$F_D = dU_D / da \Big|_{a = a_0} = \pi r^2 \cdot \frac{A}{6\pi a_0^3} . \qquad \text{Eq. 3-4}$$

The dispersion force is the force needed to separate the adhesion partners abruptly without changing the deformation of the particle. Similar to the JKR model, the interaction outside the contact area is neglected in the analytical model, *i.e.*, the dispersion force F_D is equivalent to F_S in the JKR model.

3.1.3 The adhesion procedure and the criterion for the separation

Considering that the contact radius depends on the total normal force according to $r^3 = F_T \cdot R / K$ and the displacement is given by $\delta = r^2 / R$ (Hertz theory). Thus, the following relationship between the total normal force and the dispersion force holds:

$$F_D = \pi r^2 \cdot \frac{A}{6\pi a_0^3} = \frac{A}{6a_0^3}\left(\frac{R}{K}F_T\right)^{2/3}. \qquad \text{Eq. 3-5}$$

The normal force is:

$$F_N = F_T - F_D = F_T - \frac{A}{6a_0^3}\left(\frac{R}{K}F_T\right)^{2/3}. \qquad \text{Eq. 3-6}$$

Eq. 3-5 and Eq. 3-6 can be normalized by dividing the forces F_D, F_T and F_N by $(A/6a_0^3)^3 \cdot (R/K)^2$:

$$\tilde{F}_D = \tilde{F}_T^{2/3} \text{ and} \qquad \text{Eq. 3-7}$$

$$\tilde{F}_N = \tilde{F}_T - \tilde{F}_T^{2/3} = \tilde{F}_D^{3/2} - \tilde{F}_D, \qquad \text{Eq. 3-8}$$

where $\tilde{F}_D$, $\tilde{F}_T$ and $\tilde{F}_N$ are the normalized forces, respectively. The relationship between these three terms is shown in the normalized force equilibrium plots in Figure 3-1.

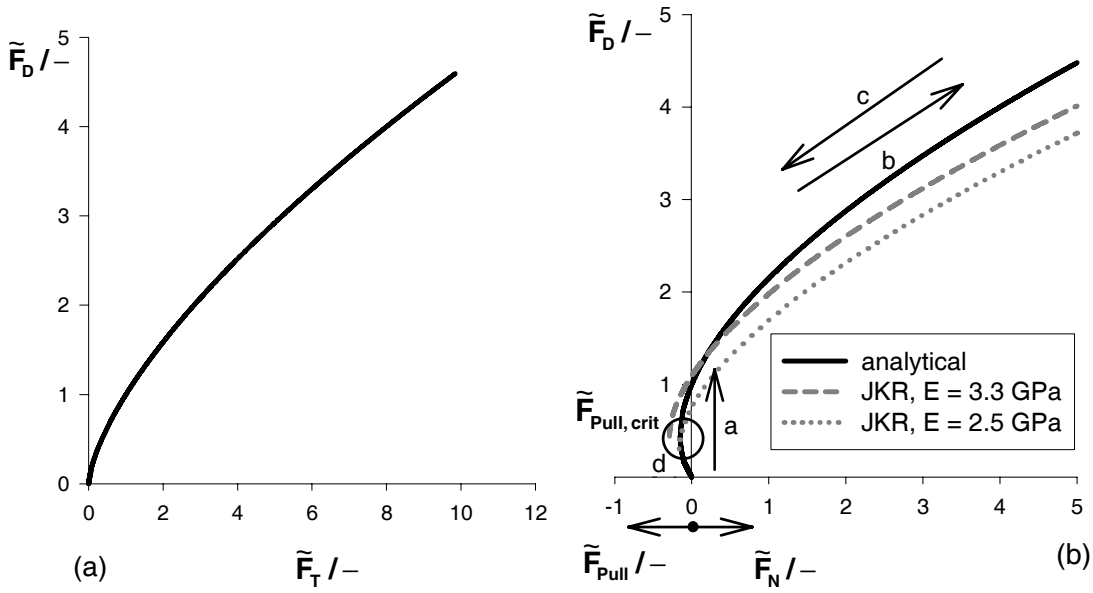

Figure 3-1 Normalized force equilibrium plots of the analytical model in comparison to the JKR model with different Young's moduli.

As shown in Figure 3-1, the approaching and retrace procedures can be described as follows:

a. As soon as the particle gets in contact with the surface, the particle deforms, until the equilibrium between the dispersion force and the elastic force is reached;

b. As the normal force increases, a new equilibrium can be established for each value of the normal force, the dispersion force increases with the normal force;

c. The normal force is reduced, turns to pulling force and reaches a calculational maximum, which is defined as the critical pulling force $F_{Pull,crit}$. Equilibrium can also be reached at each point on the referring curve;

d. When $F_{Pull,crit}$ is exceeded, equilibrium can no longer be established. Adhesion becomes instable and the surfaces separate abruptly, even though the dispersion force F_D is still larger than the pulling force.

Griffith [25] develpoed a model concerning this kind of energetic instability for the fracture mechanics. Cracks may propagate, if it is energetically favorable, *i.e.*, if it happens to reduce (or maintain) the sum of the potential energy of the applied force and the strain energy of the body. The application of the Griffith theory in predicting the separation of adhesion partners is supported by Tabor [24] and Maugis [26].

For the separation it is necessary to overcome the critical pulling force. This force can be reached if:

$$\frac{d\tilde{F}_N}{d\tilde{F}_D} = 0 \quad \Rightarrow \quad \frac{3}{2}\tilde{F}_D^{1/2} - 1 = 0 . \qquad \text{Eq. 3-9}$$

Solving this equation we get the normalized dispersion force and the normalized normal force $\tilde{F}_D = 4/9$ and $\tilde{F}_N = -4/27$, respectively. So the critical pulling force is:

$$F_{pull,crit} = -\tilde{F}_N \cdot \left(\frac{A}{6a_0^3}\right)^3 \cdot \left(\frac{R}{K}\right)^2 = \frac{4}{27} \cdot \left(\frac{A}{6a_0^3}\right)^3 \cdot \left(\frac{R}{K}\right)^2 . \qquad \text{Eq. 3-10}$$

$F_{Pull,crit}$ is the adhesion force measured with different methods (*e.g.*, force-distance measurement with AFM or centrifugal detachment method). For comparison the curves according to the JKR model are also shown in Figure 3-1. In this model, the dispersion force is calculated as:

$$F_D = \frac{A}{6\pi a_0^3} \cdot \pi r_C^2 . \qquad \text{Eq. 3-11}$$

The contact radius r_C is a function of the normal force F_N according to Eq. 2.12. The Hamaker constant A is related to the work of adhesion W with $A = W \cdot 12\pi a_0^2$ according to Israelachvili [8], where $a_0 = 0.165\,nm$ is the equilibrium separation between the atoms. The curves are also normalized with the term $(A/6a_0^3)^3 \cdot (R/K)^2$. The position of the JKR curve in the normalized $\tilde{F}_D - \tilde{F}_N$ equilibrium plot is not unique. It depends on the values of the single parameters (*e.g.*, the Young's modulus), as shown in Figure 3-1.

3.2 The numerical approach

3.2.1 FEM-simulation of the particle deformation

A higher precision can be achieved in which the dispersion interaction energy outside of the contact radius is also considered. This is only possible by means of numerical calculations. In this work FEM-simulations of the particle deformation were carried out with the program Abaqus® 6.4-1 [65] (Abaqus Inc., USA) provided by Institute of Applied Mechanics, University of Erlangen. A short summary of the main features of the FEM program can be found in Appendix 10.1. The particle was simulated with an axisymmetric 4-nodes model. In some cases (especially in case of particle-asperity contacts) grid sizes of below $1nm$ in the contact region are necessary for sufficient accuracy. This fine grid size nevertheless leads to meaningful results although at this small scale the application of any continuum model is questionable in the strict sense. From molecular dynamics simulations of compression of a spherical crystal one may conclude that the lower limit is around $3-5nm$ [66]. Luan *et al.* [67] even state that continuum mechanics may be applicable down to lengths as small as two or three atomic diameters. However, the atomic structure of surfaces can have profound consequences for larger contacts.

The (macroscopic) material property of the particle is described with elasticity or bilinear isotropic plasticity, *i.e.*, linearly elastic under the yield stress, then linearly plastic with a reduced Young's modulus. The total normal force F_T is simplified to a force acting on a distant point on the rotation axis. Amongst the adhesion partners considered in this study the flat or rough substrate surfaces have always significantly higher Young's moduli than the particles, hence, they are considered as rigid in this model.

In the FEM-simulation the stress in all directions in space can be normalized to an overall stress, the von-Mises stress [68]:

$$\sigma = \sqrt{\sigma_{xx}^2 + \sigma_{yy}^2 + \sigma_{zz}^2 - \left(\sigma_{xx}\sigma_{yy} + \sigma_{yy}\sigma_{zz} + \sigma_{zz}\sigma_{xx}\right) + 3\left(\sigma_{xy}^2 + \sigma_{yz}^2 + \sigma_{zx}^2\right)} \quad . \qquad \text{Eq. 3-12}$$

The von-Mises stress is equivalent to the absolute value of the tensile stress in the tensile test. The local deformation of the material depends on the local von-Mises stress. The total normal force F_T is varied in the FEM-simulation. If total normal forces are applied, the coordinate of each node on the particle surface can be exported to data files, which constitutes the input file for the calculation of the dispersion force.

An example of the input file for the FEM-simulation can be found in Appendix 10.2.

3.2.2 Calculation of the dispersion force

As derived from the Hamaker model [11] (Eq. 2.1) the dispersion interaction energy between two interacting axisymmetric bodies is:

$$U = -\int_{z_2}\int_{z_1}\int_{r_2}\int_{r_1}\int_{\theta_2}\int_{\theta_1}\frac{C\rho_1\rho_2 r_1 r_2}{S^6}d\theta_1 d\theta_2 dr_1 dr_2 dz_1 dz_2, \qquad \text{Eq. 3-13}$$

here ρ_1 and ρ_2 denote the number densities of the molecules in both bodies, C and S are the London–van der Waals constant and the distance between unit volumes, respectively. The unit volume is expressed in a cylindrical coordinate system as $dV = r\,d\theta\,dr\,dz$.

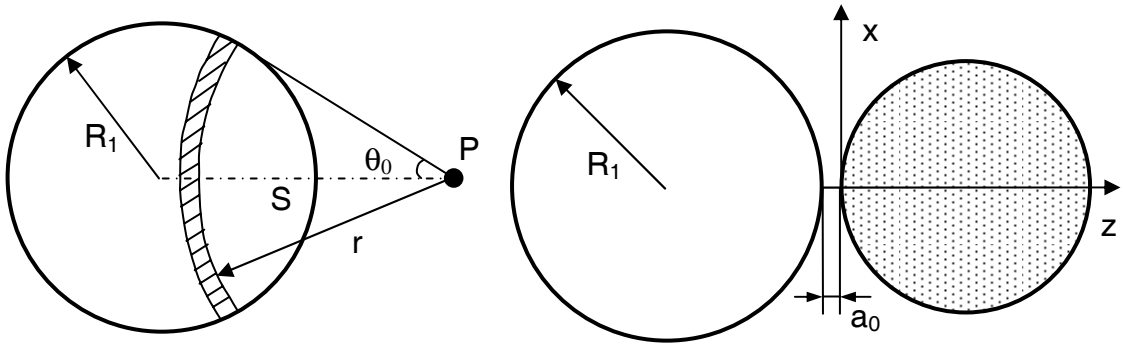

Figure 3-2 The dispersion interaction energy is calculated in two steps: 1. Integration according to Hamaker to get the point-to-sphere interaction energy (left). 2. Numerical integration over the deformed particle (dotted) to get the total interaction energy (right).

The interaction energy between a point P in the deformable particle and the rigid sphere (see Figure 3-2 left) can be calculated by integrating the interaction energy over the rigid sphere of radius R_1 [11]:

$$\begin{aligned} U_{point\_sphere} &= -\int_{S-R_1}^{S+R_1}\frac{C\rho}{r^6}\pi\frac{r}{S}\left[R_1^2-(S-r)^2\right]dr \\ &= \frac{C\rho\pi}{S}\cdot\left(\frac{R_1^2-S^2}{4r^4}+\frac{2S}{3r^3}-\frac{1}{2r^2}\right)\Bigg|_{r=S-R_1}^{r=S+R_1}. \end{aligned} \qquad \text{Eq. 3-14}$$

Further integration over the deformable particle has to be carried out numerically (*e.g.*, by applying the rectangle rule):

$$U_{particle\_sphere} = 2\pi\rho \int_x \int_z \frac{C\rho\pi}{S}\left[\left(\frac{2S}{3r^3} + \frac{R_1^2 - S^2}{4r^4} - \frac{1}{2r^2}\right)\Bigg|_{r=S-R_1}^{r=S+R_1}\right] x dx dz$$
$$= 2A\sum_x \sum_z \frac{1}{S}\left[\left(\frac{2S}{3r^3} + \frac{R_1^2 - S^2}{4r^4} - \frac{1}{2r^2}\right)\Bigg|_{r=S-R_1}^{r=S+R_1}\right] x\Delta x\Delta z \quad . \qquad \text{Eq. 3-15}$$

The distance S from a point in the deformable particle to the center of the rigid sphere can be calculated from the coordinate x and z of this point (see Figure 3-2 right). In case of micron-sized particle in contact with a rigid sphere or surface $x = 0..200\,nm$ and $z = z_{\min}(x)..100\,nm$ is sufficient to keep the relative error below 1%. $z_{\min}(x)$ describes the contour of the deformed particle, it is achieved by interpolating the discrete contact geometry data from the FEM-simulation with a cubic spline, taking into account a contact distance $a_0 = 0.4\,nm$. Of course, dispersion forces inside and outside of the region of direct contact (at a_0) are included.

The dispersion force is also calculated numerically:

$$F_D = \frac{U_{particle\_sphere, a_0+\delta} - U_{particle\_sphere, a_0}}{\delta}, \qquad \text{Eq. 3-16}$$

where δ is an infinitesimal distance. Different total normal forces F_T are applied to the particle to obtain a curve in the force equilibrium plot, see Figure 3-1. It is important to note that this approach is not limited to spherical geometries but can be applied to any contact geometry. Intrinsically, this hybrid approach combines continuum modeling of material deformation with molecular simulation to obtain the adhesion forces. Under the assumption of additivity of dispersion forces, the molecular simulation is replaced by volume integral over the contact geometry. Generalization of this approach to other thermo-mechanical properties, different particle sizes and shapes, other types of intermolecular forces and varied external forces is straight forward.

The Hamaker summation is programmed with C-code, the Nassi-Shneidermann diagram of the program structure is shown in Appendix 10.3.

3.2.3 Case study 1: elastic and plastic particle with low modulus

The adhesion between a polystyrene particle with low Young's modulus and a flat rigid surface ($R \to \infty$ and $E \to \infty$) is simulated according to the numerical approach. At first, it is assumed that the deformation of the polystyrene particle is purely elastic. The data used for the simulation of the particle deformation and for the calculation of the adhesion force are as follows:

Particle diameter $2R = 10\,\mu m$

Young's Modulus $E = 3.3\,GPa$

Poisson number $\nu = 0.32$

Hamaker constant $A = 6.6 \cdot 10^{-20}\ J$

The Young's modulus and the Poisson number are taken from the CAMPUS®-database for polystyrene 158 K (BASF) at $23°C$. The value of the Hamaker constant is taken from Visser [10] applying the Lifshitz approach.

The FEM method has been validated by comparison with Hertzian contact mechanics. Both approaches should lead to similar results as long as the deformation of the sphere remains purely elastic. For example, for the given spherical polystyrene bead on a flat surface being compressed by a total normal force of $F_T = 5\,\mu N$, both approaches lead to an identical displacement of $6\,nm$ and to contact radii of $180\,nm$ and $172\,nm$ for the FEM and Hertzian methods, respectively. The numerically obtained force equilibrium curves are shown in Figure 3-3 together with the corresponding analytical solutions resulting from Eq. 3-5 and Eq. 3-6. It can be observed that the dispersion forces calculated with the numerical method are significantly higher than the analytical results. Accordingly, the adhesion force, *i.e.*, the critical pulling force is also higher. This difference is due to the restrictions of the analytical model, which neglects the dispersion force outside of the contact area.

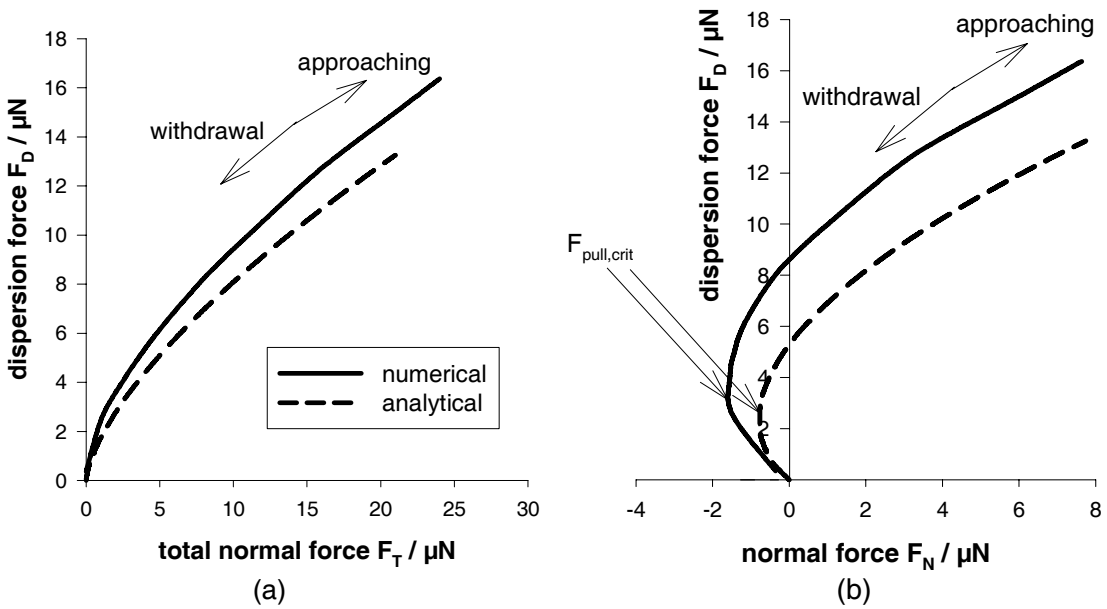

Figure 3-3 Numerically simulated force equilibrium plot of a $10\,\mu m$ polystyrene particle in contact with a flat rigid surface with the assumption that the particle deformation is elastic. For comparison the results of the analytical approach (Eq. 3-5 and Eq. 3-6) are also illustrated. Separation occurs when the pulling force reaches $F_{Pull,crit}$.

For the observed $10\,\mu m$ polystyrene particle, the FEM-simulation shows that the yield stress of $50\,MPa$ is reached with a total normal force of $F_T = 5\,\mu N$. Without any external normal force, *i.e.*, $F_N = 0$, the dispersion force reaches $8.3\,\mu N$. The polystyrene particle deforms plastically as soon as the contact to a flat rigid surface is established.

Therefore, it is necessary to take the plastic deformation of the particle into consideration. The plasticity of the material is simulated with a bilinear plasticity model. In the case of polystyrene the Young's modulus is $3.3\,GPa$ in the elastic range If the stress is larger than the yield stress of $50\,MPa$ the slope of the stress-strain curve is $1.0\,GPa$. These values are obtained through discretization of the stress-strain curve of polystyrene 158 K (BASF) at $23°C$ (CAMPUS®-database), as shown as the dotted and the dashed curves in Figure 3-4. The curve with $E = 4.0\,GPa$ in the elastic range is also shown in this diagram. This curve fits better for small strains below $0.5\,\%$.

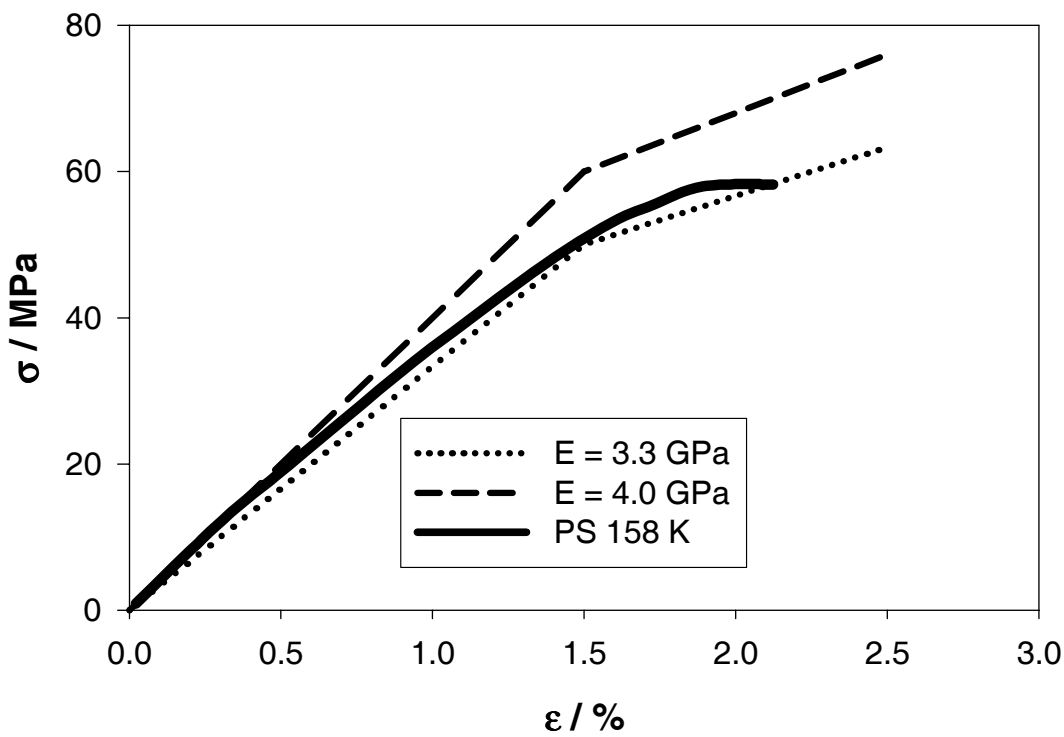

Figure 3-4 Stress-strain diagram of polystyrene 158 K (BASF) at $23°C$ and the approximation of this curve with the bilinear model.

As an example, the compression of a $10\,\mu m$ polystyrene particle is pressed to a flat rigid surface with a maximal total normal force of $F_T = 24\,\mu N$ and the subsequent retrace procedure is simulated. As shown in the force plot (Figure 3-5) as well as in the force-displacement diagram (Figure 3-6) the approaching and retrace curves deviate from each other, since the deformation cannot be totally recovered. Here the displacement is defined similar to the displacement in the JKR model (Paragraph

2.1.2.1): it is the distance, by which distant points in both adhesion partners approach each other.

In the course of approaching the normal force becomes negative at small displacements, as shown in Figure 3-6. This effect can be explained by the simulation routine. During the FEM simulation a total normal force of increasing magnitude is applied to the particle, which causes the deformation of the particle. The dispersion force between the deformed particle and the substrate is then calculated by means of Hamaker summation. If the value of the dispersion force is higher than the total normal force applied in the FEM simulation, the normal force becomes negative according to Eq. 3-6. The deformation at that total normal force is not stable, the particle will deform further alone due to the dispersion force until equilibrium is reached, *i.e.*, $F_D = F_T$ and $F_N = 0$.

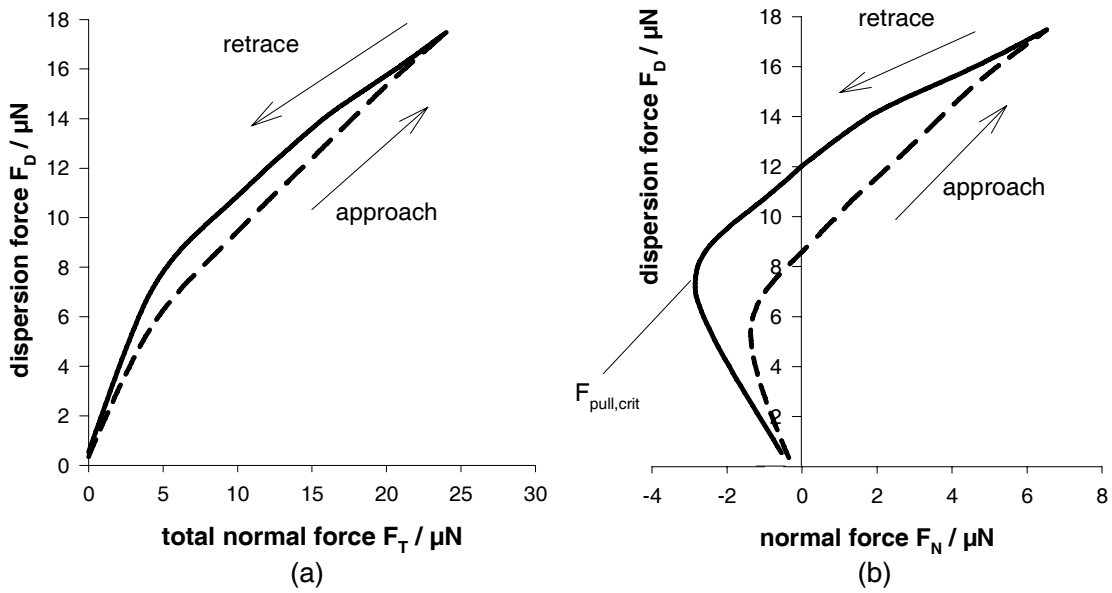

Figure 3-5 Numerically simulated force equilibrium plot of a 10 μm polystyrene particle in contact with a flat rigid surface, the material property of the particle is modeled with bilinear plasticity.

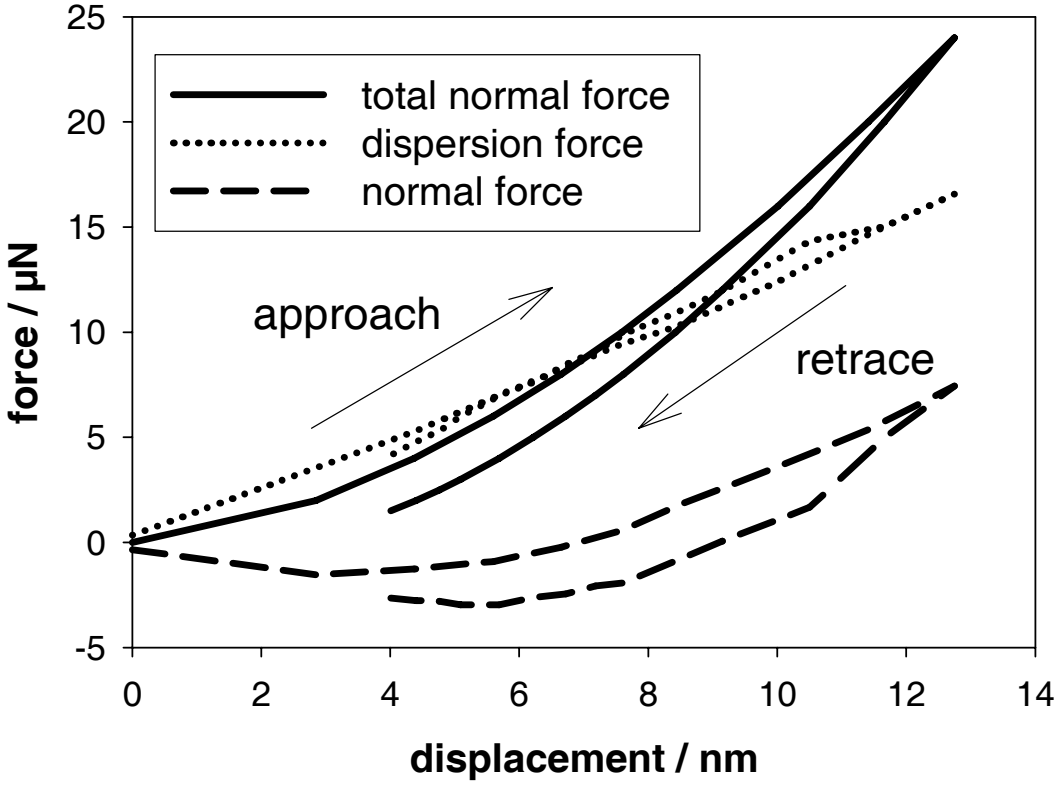

Figure 3-6 Numerically simulated force-displacement behavior of a 10 μm polystyrene particle in contact with a flat rigid surface.

In the simulation including plastic deformation the adhesion force is larger than the elastic case (see Figure 3-3). The value of the adhesion force depends on the maximally applied normal force. In comparison to the Rumpf model for plastic deformation (see Paragraph 2.1.2.2) the numerical approach is physically more accurate because it includes the full plastic deformation and calculates the van der Waals force inside and outside of the contact region. Furthermore, it can be expanded to include arbitrary material properties and geometries.

3.2.4 Case study 2: elastic particle with high modulus

A second numerical simulation is carried out with a silica particle and a flat wafer. The deformation of the silica particle is modeled as ideally elastic. We used the following data for the simulation:

Particle diameter $2R = 10\,\mu m$

Young's Modulus $E = 75 GPa$

Poisson number $\nu = 0.17$

Hamaker constant $A = 6.6 \cdot 10^{-20}\ J$

The mechanical properties of silica are taken from [69] and the Hamaker constant is taken from [8]. The simulation results are shown as force equilibrium curves in Figure 3-7. Figure 3-8 shows the related force-displacement diagram.

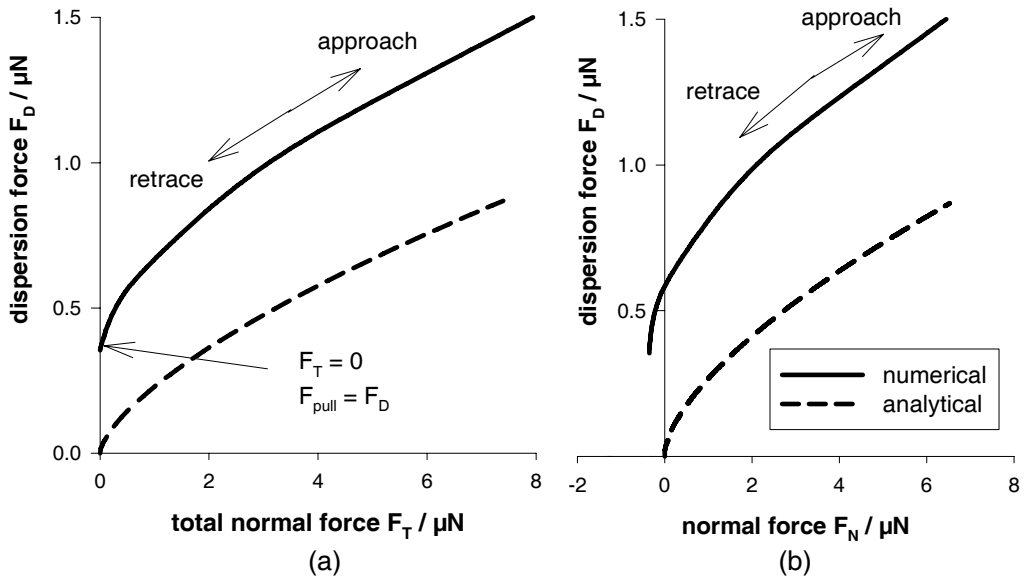

Figure 3-7 Numerically simulated force equilibrium plot of a 10 μm silica particle in contact with a flat rigid surface in comparison to the results of the analytical approach (Eq. 3-5 and Eq. 3-6).

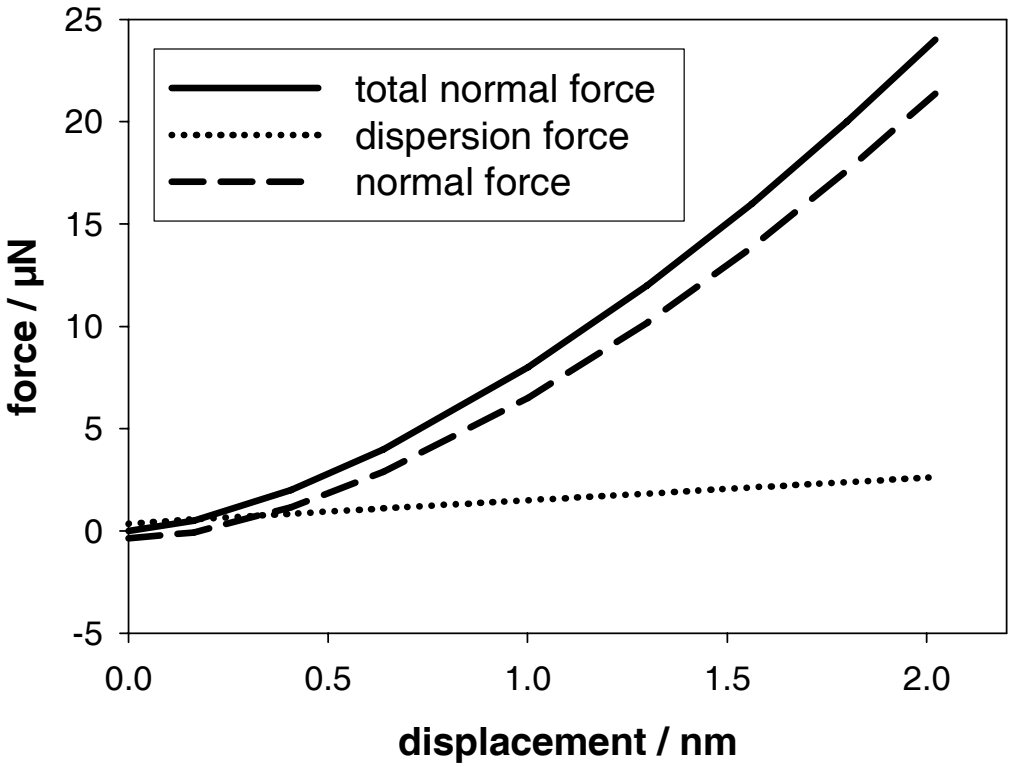

Figure 3-8 Numerically simulated force-displacement behavior of a 10 μm silica particle in contact with a flat rigid surface.

In this simulation the approaching and the retrace curve are identical because of the fully reversible elastic deformation. During retrace the dispersion force reduces monotonically with the normal force (Figure 3-7b) until the sum of these two forces reaches $F_T = 0$ (Figure 3-7a and Figure 3-8). No critical pulling force $F_{pull,crit}$ can be observed in this case. The particle separates abruptly from the surface when the pulling force F_{pull} surpasses the dispersion force F_D. The simulation indicates that the separation does not take place before the contact radius r and the displacement δ reduce to zero. A small deformation with $r = 8\,nm$ and $\delta = 0.36\,nm$ remains at the moment of separation. Obviously, the continuum FEM-simulation is (in the strict sense) no longer valid at such small scale. Nevertheless the corresponding simulation gives a reasonable adhesion force value of $354\,nN$, which is only slightly larger than the result obtained from the Hamaker model ($344\,nN$) for rigid adhesion partners. Recently, Yang *et al.* [70] showed good accordance of their molecular dynamics simulation with the Hertz theory in the sub-micron scale. The pressure distribution in the contact region between a spherical tip and a flat surface estimated by both approaches is quite similar. The continuum approaches (*e.g.*, the Hertz model) do not totally lose their validity, except that the continuum models always assume a sudden jump of the contact pressure to zero at the edge of the contact circle, while the molecular dynamics simulations predict a physically more reasonable, gradual reduction of the contact pressure along the radius. Independent of the work of Yang *et al.*, Luan and Robbins [67] simulated the pressure between a tip and a flat surface with molecular dynamics simulation. The local contact pressure is very sensitive to the molecular structure of the surface. In case of an amorphous structure, for instance, the local contact pressures and the substrate scatter strongly. However, averaged contact pressures agree fairly well with the Hertz theory. Both Luan and Robbins and Yang *et al.* found that the radius of the contact region is slightly larger than the prediction of the Hertz model. As shown in Section 3.2.3, the FEM simulation also predicts a slightly larger contact radius than the Hertz model.

The case studies show that separation takes place if one of the two criteria is fulfilled. Between smooth adhesion partners the type of separation depends first of all on the material properties of the adhesion partners. Adhesion partners with low moduli are separated, if the critical pulling force $F_{pull,crit}$ is reached (**type A**). Adhesion partners with high moduli can already be separated if $F_{pull} = F_D$ (**type B**), *i.e.*, before the critical pulling force $F_{pull,crit}$ is reached.

3.2.5 Case study 3: Adhesion of low modulus particle on rough surfaces

Small asperities in the contact region have a significant influence on the adhesion force between particles and substrates. Rumpf [17] showed that for rigid adhesion

partners the adhesion force is reduced by a factor of hundred in the presence of an asperity of proper size, which is usually in the nanometer range.

Because of the small contact area, the stress is concentrated in the contact region. The maximal von-Mises stress in the contact region is significantly higher than in the case of contact between smooth adhesion partners. Figure 3-9 shows the maximal von-Mises stress in dependence of the Young's modulus of the particle and the total normal force for the case of a $10\,\mu m$ particle in contact with an asperity of $r = 250\,nm$.

The material properties of various polymer materials (Young's modulus, yield stress) (chosen from the CAMPUS®-database) are also shown in this figure. Obviously, the yield stress of the polymers can be reached with a fairly small total normal force F_T, which is below the adhesion force between the particle and the substrate. Furthermore, the maximal von-Mises stress is approximately proportional to the inverse quadric asperity radius as obtained from simulations where the asperity size was varied systematically. With decreasing asperity size yielding occurs at even smaller total normal forces. Thus, the influence of the plastic deformation on the particle adhesion between rough adhesion partners is a major influencing parameter.

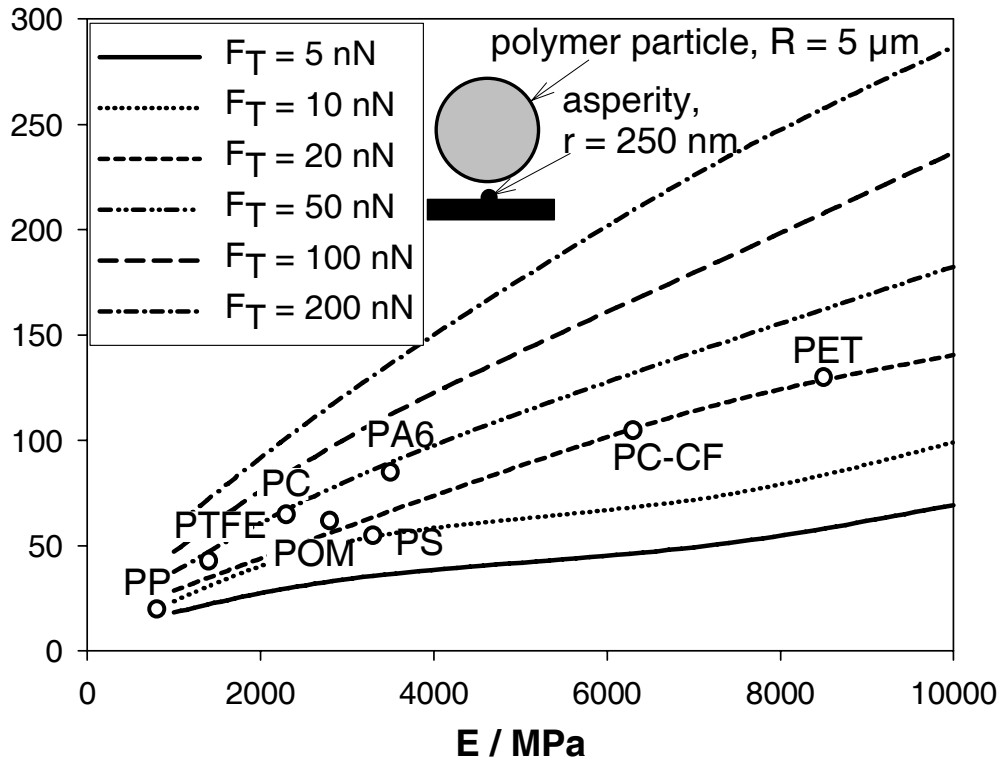

Figure 3-9 Maximal von-Mises stress in the contact region of a polymer particle in contact with an asperity of $r = 250\,nm$. The literature values of the Young's modulus and yield stress of different polymer materials are shown as circles in the diagram.

In the next step the adhesion force between a $10\,\mu m$ polystyrene particle and a rigid surface with an asperity of $r = 50\,nm$ in the contact region is simulated. As in the simulation between smooth adhesion partners the material property of polystyrene is modeled with bilinear plasticity. The simulation results referring to a maximal vertical force of $F_N = 3.2\,\mu N$ are shown in Figure 3-10a. In comparison to the simulation between smooth adhesion partners there is a range of small normal forces (a→b) where the asperity acts as a spacer between the particle and the flat surface, *i.e.*, the particle still has no direct contact with the flat surface or the contact is so weak, *i.e.*, elastic deformation prevails, that the contact will automatically break if the normal force disappears. This case is shown in Figure 3-11b, the sudden increase of the slope at the end of the curves indicates that the particle gets in contact with the flat surface. Figure 3-12 shows the direct contact between the polystyrene particle and the flat surface covering completely the asperity in the contact region. If the normal force exceeds the point b the particle deforms so strongly that the asperity losses its function as a spacer. Similar to the step a described in Paragraph 3.1.3, a new equilibrium will be reached at point c with a significantly higher dispersion force. The next steps (c→d→e) of the procedure are the same as described in Paragraph 3.1.3. The separation is of type A, a maximum of the pulling force (or a minimum of the normal force) can be observed in Figure 3-10a as well as in Figure 3-11a. The adhesion force is equal to the critical pulling force $F_{pull,crit}$ at point e (1.2 μN). The case of normal forces in region from a to b is shown in Figure 3-10b. The separation is of type B and takes place at point e', when $F_{pull} = F_D$, accordingly $F_T = 0$, as shown in Figure 3-10b and Figure 3-11b. In this case, the adhesion force ($0.43\,\mu N$) is significantly smaller compared to cases with higher normal forces. In conclusion, it is possible to adjust the adhesion force and the type of separation, *i.e.*, A and B, respectively, by varying the maximal normal force and the size of the asperity.

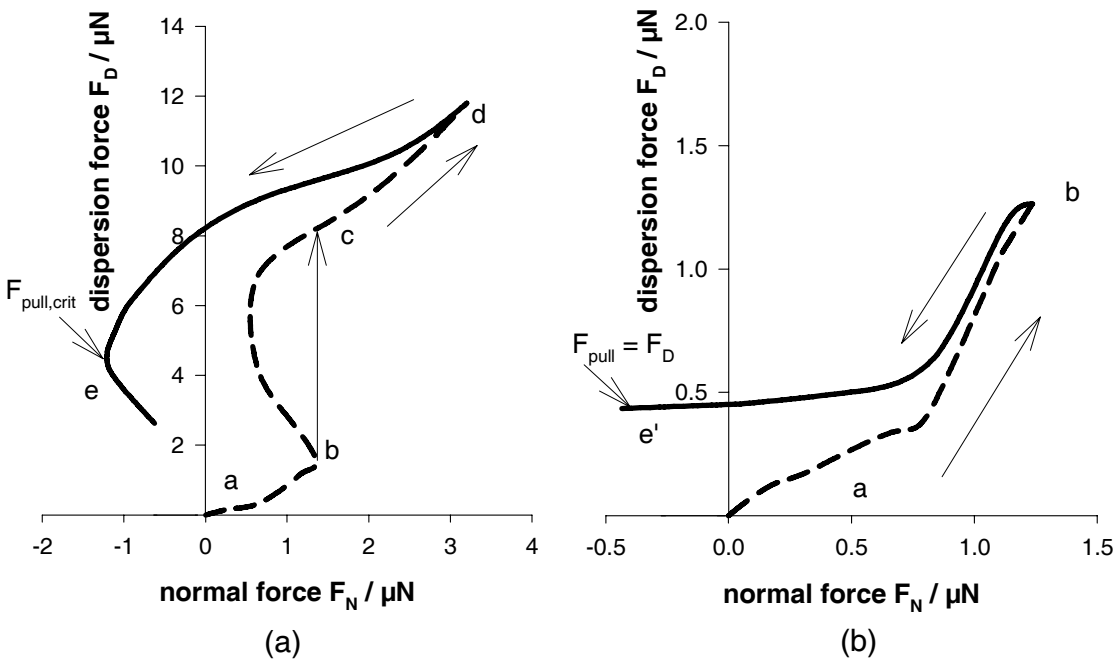

Figure 3-10 Force equilibrium plot of a 10 μm polystyrene particle in contact with a rigid surface with an asperity of $r = 50\,nm$, the material property of the particle is modeled with bilinear plasticity. (a): at large normal force; (b): at small normal force.

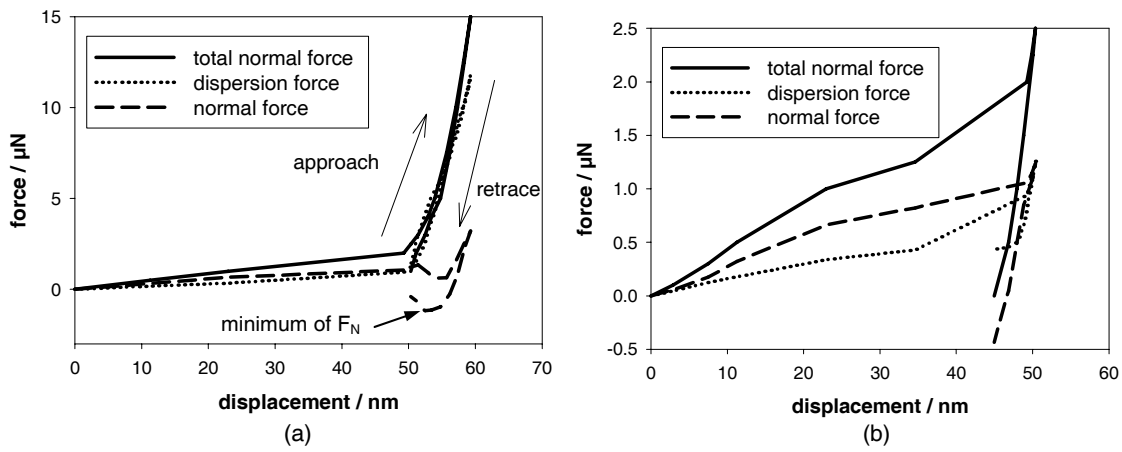

Figure 3-11 Numerically simulated force-displacement behavior of a 10 μm silica particle in contact with an asperity of $r = 50\,nm$. (a): at large normal force; (b): at small normal force.

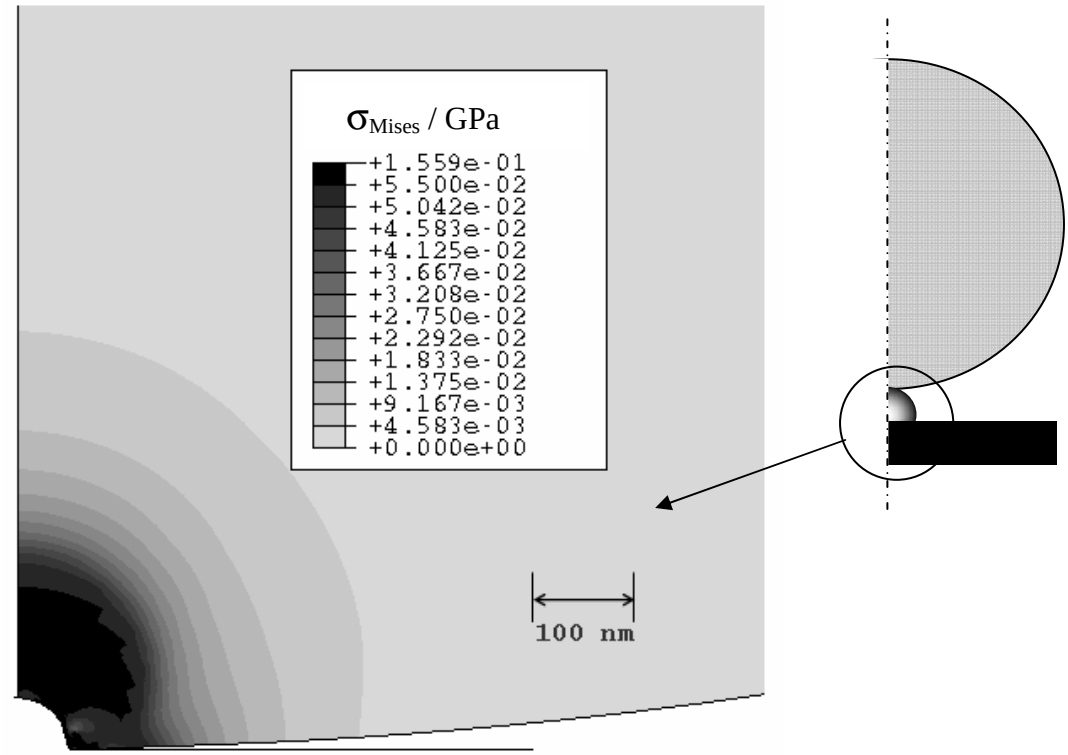

Figure 3-12 FEM-simulation: Particle deformation and local stress in a $10\,\mu m$ polystyrene particle in contact with a rigid surface with an asperity of $r = 50\,nm$ on the contact area. The particle gets in contact directly with the flat surface at a large normal force (*e.g.*, $2000\,nN$).

4 MATERIALS AND MEASURING METHODS

4.1 Investigated materials

4.1.1 Toner and model particles

Mostly, toner particles are ground polymer particles with diameters ranging from 5 to $15\,\mu m$. In order to be used in the electrophotographic process the polymer particles are modified: They include a binding material such as a resin, a pigment to give the color and additives to provide proper particular properties to the toner particle. One commonly used additive is nano-sized silica. The silica particles can be produced by means of a pyrogenic or a sol-gel process [71].

Various toner types (Océ Printing Systems (OPS), Munich) with various additives are investigated in this study. Figure 4-1 (left) shows one example of such particles. The irregular shape of the particle and the surface additive can be observed. Since the toner particles are inhomogeneous, chemical and physical properties of the toner particles are not well defined. The adhesion force between the toner particles and substrates can be widely scattered and strongly depends on the individual particle. Hence, to investigate the dependence of particle adhesion on various parameters it is necessary to find well defined particles. Smooth polymer particle polystyrene particles (Postnova, Landsberg/Lech) with a diameter of $10\,\mu m$ are chosen as a model substance in this study. The surface properties of the polystyrene particle surfaces can be modified in which they are dyed, *i.e.*, they are coated with nano-sized pigment particles.

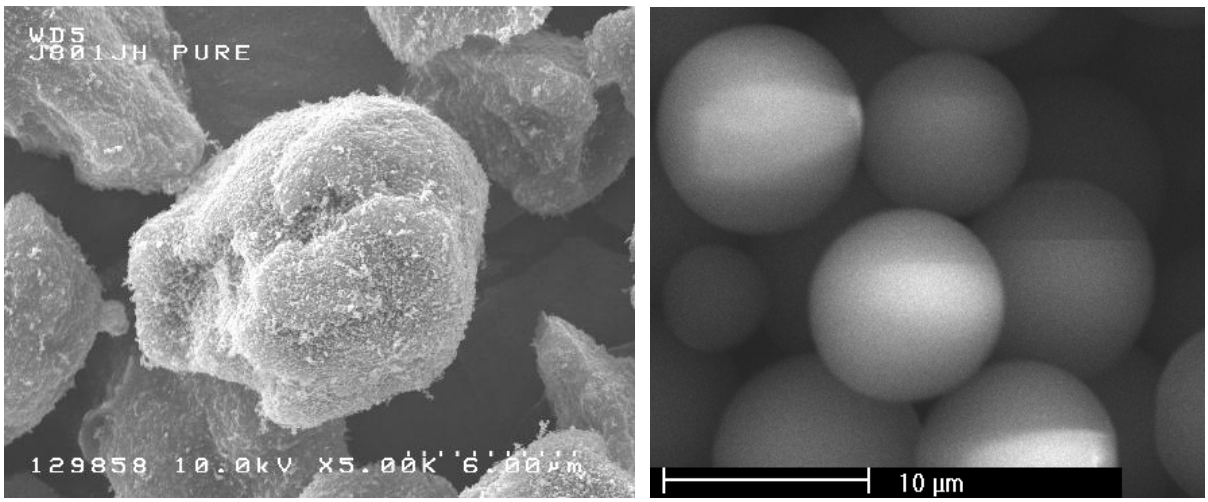

Figure 4-1 Left: SEM micrograph of ground toner particles coated with various surface additives. Right: SEM of smooth polystyrene particles without surface coating.

The adhesion behavior of nanometer and micron-sized silica particles is investigated as well. Nanoscale colloidal silica particles are produced in a sol-gel process (Degussa, Hanau); micron-sized silica particles are produced through sintering of quartz flour (MILLISIL W12, Quarzwerke, Frechen) in a flame reactor [72] or through encapsulated precipitation (Postnova, Landsberg/Lech).

The pre-treatment processes of the investigated particles prior to the adhesion force measurements are shown in Table 4-1.

Table 4-1 Particles and their pre-treatments

Particles (mean diameter)	Source / Production	Pre-treatment and preparation
Toner of different types ($8\,\mu m$)	OPS / ground	None (in some measurements electrostatically charged, see Paragraph 2.2.1)
Polystyrene ($10\,\mu m$)	Postnova / polymerized (without surface functionalities)	1. Rinsed with ultra-pure water; 2. Dried with pure nitrogen.
Dyed Polystyrene ($10\,\mu m$)	Postnova / polymerized (coated with pigment nano-particles of several $10\,nm$)	None
Silica particle ($30\,nm$)	Degussa / sol-gel process	1. Rinsed with ultra-pure water; 2. Dried with pure nitrogen 3. Heated up to $800\,°C$ 4. Cooled down to the room temperature in pure nitrogen flow
Silica particle ($10\,\mu m$)	LFG / sintered	1. Rinsed with ultra-pure water; 2. Dried with pure nitrogen 3. Heated up to $800\,°C$ 4. Cooled down to the room temperature in pure nitrogen flow
Silica particle ($10\,\mu m$)	Postnova / precipitated	1. Rinsed with ultra-pure water; 2. Dried with pure nitrogen 3. Heated up to $800\,°C$ 4. Cooled down to the room temperature in pure nitrogen flow

4.1.2 Organic photo conductor (OPC) and model surfaces

The modern photo conductor (PC) surface is of organic basis. Figure 4-2 shows the structure of the OPC [73]. If the surface is illuminated (Paragraph 1.2), the charge generating layer (CGL) absorbs the light and generates electron-hole pairs. The positive charge migrates through the charge transfer layer (CTL) to the surface and compensates the surface charge; the negative charge is directed to the aluminum electrode. The CTL and the CGL are both made from polymer materials.

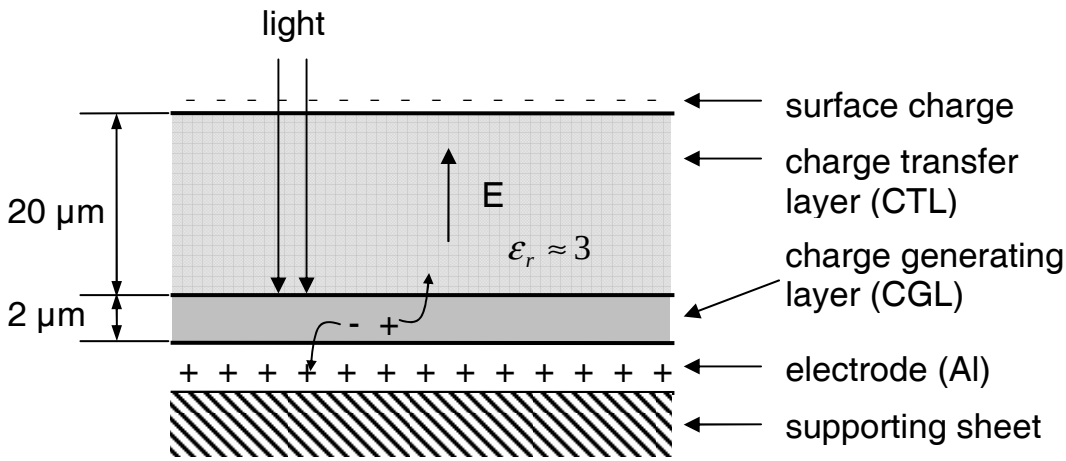

Figure 4-2 Structure of the OPC.

Beside the PC various other surfaces with different properties are also investigated in this work. Silicon wafer {100} (Wacker, Burghausen) with a root-mean-square (rms) roughness significantly below $1nm$ is used as a model of ideally smooth surfaces. To investigate the influence of roughness on the adhesion force, the substrate surfaces are treated with various techniques (*e.g.*, polishing, physical vapor deposition (PVD) and dip-coating) [74]. In order to understand the influence of hydrophobicity on the adhesion force in humid ambience, the surface chemistry of the mica substrates (Plano, Wetzlar) is functionalized through silanization. The substrates investigated in this work are summarized in Table 4-2.

Table 4-2 Substrates and their pre-treatments

Substrates	Source / Production	Pre-treatment
OPC	OPS / unknown	Untreated (in some measurements coated with silica or ITO nano-particles)
Silicon wafer	Wacker / polished	1. Cleaned with acetone and ethanol; 2. Rinsed with ultra-pure water; 3. Dried with pure nitrogen; 4. Heated up to $800°C$ 5. Cooled down to the room temperature in pure nitrogen flow
Mica	Plano / unknown	Freshly cleaved (in some measurements silanized)
Aluminum	LFG / PVD-coated	1. Cleaned with acetone and ethanol; 2. Rinsed with ultra-pure water; 3. Dried with pure nitrogen; 4. Heated up to $150°C$ 5. Cooled down to the room temperature in pure nitrogen flow
Aluminum	LFG / polished	1. Cleaned with acetone and ethanol; 2. Rinsed with ultra-pure water; 3. Dried with pure nitrogen; 4. Heated up to $150°C$ 5. Cooled down to the room temperature in pure nitrogen flow
Particulate silica surfaces	LFG / dip-coating	1. Cleaned with acetone and ethanol; 2. Rinsed with ultra-pure water; 3. Dried with pure nitrogen; 4. Heated up to $900°C$ 5. Cooled down to the room temperature in pure nitrogen flow

4.2 Characterization methods

Roughness [75, 76], surface charge [40, 51] and surface chemistry [77] of the particles and the substrates may have an influence on the adhesion force. These properties are characterized by means of various methods.

4.2.1 Atomic Force Microscopy for the topography measurement

Atomic Force Microscopy (AFM) was invented by Binnig [78] in the 1980's. It was designed as a nanoscale profilometer. Modern AFMs provide various possibilities to record and visualize the topography, the charge distribution and diverse surface properties of the probe [79]. In this work, topography measurements are carried out with a commercial AFM (Nanoscope 3a, Digital Instruments, USA) in Tapping Mode (TM-AFM). The surface profile is mapped by lightly tapping the surface with an oscillating probe tip (*e.g.*, OMCL-AC 160TS, Olympus, Japan) with a radius of approximately $10\,nm$. The cantilever's oscillation amplitude (typically on the order of a few 10's of nanometers) changes with the tip-substrate distance, and the topography image is obtained by monitoring these changes and closing the z feedback loop to minimize them. In the frame of this work TM-AFM measurements of different particles and substrates are performed in ambient air. The roughness of the surfaces can be expressed in terms of the rms-roughness R_{rms} [32]:

$$R_{rms} = \sqrt{\frac{1}{n}\sum_{n}\left(z(n)-\bar{z}\right)^2}\ , \qquad \text{Eq. 4-1}$$

where n is the number of the lattice points, $z(n)$ is measured height of each lattice point and

$$\bar{z} = \frac{1}{n}\sum_{n} z(n) \qquad \text{Eq. 4-2}$$

is the average height of the profile. The n lattice points can be distributed on a line (one-dimension roughness profile) or on an area (two-dimension roughness profile).

The R_{rms} value strongly depends on the size of the sampling area [33]. If a small sampling area (*e.g.*, $1\mu m \times 1\mu m$) is chosen, this value gives information on the structure of the surface at the nanoscale. The adhesion force is sensitive to changes of the nano-structure.

4.2.2 Surface Potential (SP) for the surface charge distribution measurement

Surface charge distribution can be measured with field or potential probes. Any probe in the electric field distorts the field and a signal is induced [80]. The surface charge distribution measurement with SP bases on the well known Kelvin probe method [81-84].

The Kelvin probe method is based on concepts developed by Lord Kelvin in 1898. It is an extremely sensitive analytical tool to measure the work functions of the materials. When two materials with different work functions are brought together, electrons are transferred from the material with the lower work function to the one with the higher work function. Equal and opposite charges are formed on the both surfaces [85]. The voltage developed over this capacitor is called the contact potential difference $U_{CPD} = -(\phi_1 - \phi_2)/e$, where ϕ_i is the work function of each material and e is the elementary charge.

The SP method is a secondary imaging mode derived from the TM-AFM. It is performed through a two-step technique, the so-called Lift-Mode. In the first step the topography of the surface is measured in the tapping mode; during the second step the electric potential is measured using the topographical information to track the probe tip at a constant height above the sample surface, as shown in Figure 4-3. Measuring at a constant height assures a constant sensibility of the potential measurement in the second step. During the second step the electric potential is measured in which the tip is set to a voltage U_1 and it is forced to vibrate with a certain frequency near its resonance frequency (large amplitude, high sensitivity). Wherever the potential of the surface U_2 differs from the potential of the tip, the tip and the cantilever experience an electric force which is proportional to the potential difference of the two surfaces:

$$F_e \propto |U_1 - U_2|, \qquad \text{Eq. 4-3}$$

so that the vibration of the tip is disturbed, the vibration of the cantilever differs from the driving signal with a phase shift. The force is nullified by varying the voltage U_1 of the tip so that the tip is at the same potential as the region of the sample surface U_2 underneath it:

$$U_1 - U_2 = 0 \quad \rightarrow \quad F_e = 0\,. \qquad \text{Eq. 4-4}$$

Hence, the SP method is a nulling technique. In the frame of this work the SP measurements are carried out with the Nanoscope IIIa equipped with a phase detection kit. The phase detection kit consists of a conductive cantilever, a cantilever holder which provides a special channel to contact the cantilever, and the electronics to set the electric potential on the cantilever and to detect the phase shift.

Details concerning the AFM imaging techniques can be consulted in the Nanoscope documentation and in reviews of Garcia [86] and Giessibl [79].

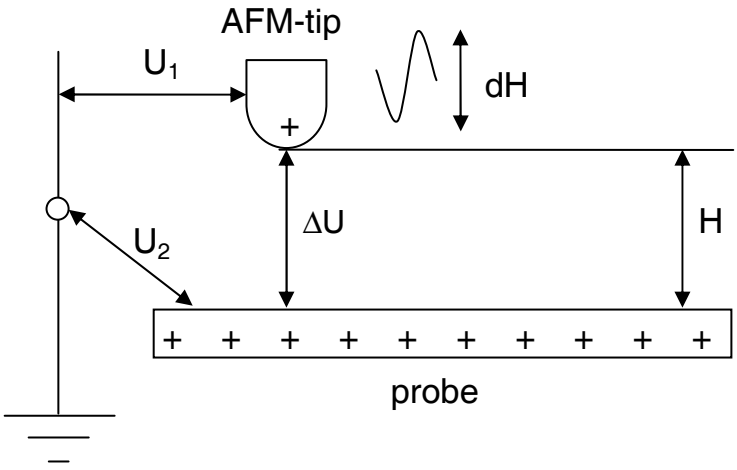

Figure 4-3 Principle of the SP measurement.

4.2.3 q-test for the particle charge distribution measurement

While SP measures local charge distributions on the surfaces, the total charge on the toner particles can be measured with the so-called q-test equipment (Epping, Freising). In this test the toner-carrier mixture (6 weight percent of toner) is agitated in an activation cell, so that the toner particles are charged triboelectrically as in the electrophotographic process. The toner particles are then sucked into a measuring chamber with an air stream and a flow across an electric field. Charged particles are deflected by the electric field force and settle on the electrodes according to the q/d-ratio [87]. The electrode can be scanned with an image analysis equipment to get the q/d-distribution of the particles. Since in this measurement the particles tend to build agglomerates on the electrodes, the amount of particles is very difficult to determine, hence, the pixel number at each q/d-range is used as a measure of the particle amount. The measuring range can be varied by modifying the electric potential of the electrodes and the air flow through the measuring chamber. The investigated toner types have usually a dominating part of the particles in the q/d-range from 0.1 to $1\,fC/\mu m$, the configuration $-2000V$ electrode potential and $160\,ml/min$ air flow provide a proper resolution in this range.

This method can also be applied to disperse the particles on the substrates according to the q/d-ratio for the electric field detachment measurement (Paragraph 4.3.3).

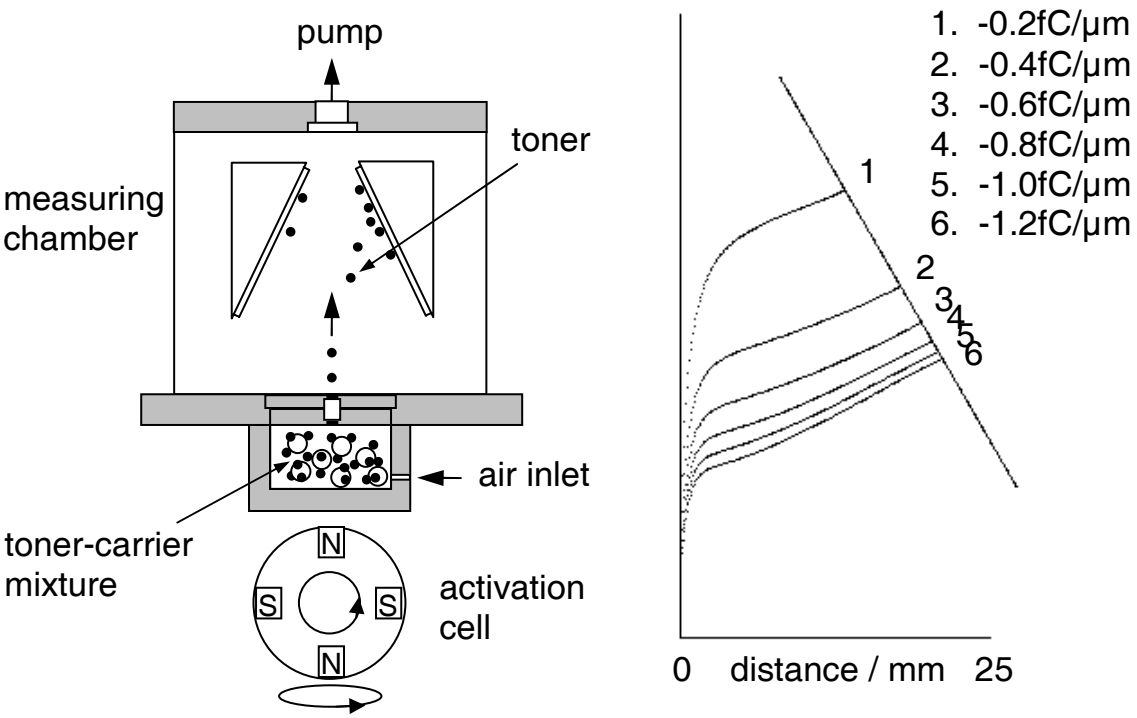

Figure 4-4 Scheme of the q-test equipment (left) and trajectory of toner particles with different q/d -ration in the measuring chamber (right), settings: electrode potential $2000V$ and air flow $160\,ml/min$.

4.2.4 Characterization of the toner conductivity

In the electrophotographic process the particle charge can be obtained not only triboelectrically in the developing stage but also through conduction in the jumping process (see Paragraph 2.2.1). The conduction behavior of the toner particles is investigated with the resistance measurement at high voltage range (up to several $1000V$) as well as with the impedance measurement at low voltage level (*e.g.*, $1V$).

4.2.4.1 The resistance measurement

Prior to the resistance measurement at high voltage the toner particles are dispersed homogenously on two round steel electrodes ($\phi 20\,mm$) with the sedimentation apparatus, which will be described later in Paragraph 4.3.2. Then the electrodes are mounted with the toner side facing each other to form an approximately $50 \sim 100\,\mu m$ thick toner layer between two electrodes. This layer is usually not a closed layer, but coverage of at least 50% can always be reached. The electrodes are then connected to a circuit with a high voltage supplier (Model 248, Keithley, USA). The resulted current is recorded with a picoamperemeter (Model 6487, Keithley, USA). The conductivity κ of the probe can be calculated as:

$$\kappa = \frac{l}{RA}, \qquad \text{Eq. 4-5}$$

where l and A are the thickness and the cross sectional area of the probe, respectively, and $R = U / I$ is the resistance measured with this method.

4.2.4.2 The impedance measurement

The impedance measurements [88, 89] are carried out with the broadband dielectric spectrometer (Novocontrol Technologies, Hundsangen). As in the resistance measurement, the toner particles are dispersed on the electrodes with the sedimentation apparatus. To investigate the bulk conductivity of the toner material, the toner particles can also be sintered at a temperature of $70°C$ over night, right below the melt temperature of the toner. The impedance spectrum is determined at frequencies varying from $10^7\,Hz$ to $10^{-4}\,Hz$. An AC voltage $U(t) = U_{max}\,sin(\omega t)$ is applied between the electrodes and the resulted current $I(t)$ is recorded. Similar to the Ohm's law, the relationship between the voltage and the current is:

$$Z(\omega) = \frac{U(t)}{I(t)}, \qquad \text{Eq. 4-6}$$

where $Z(\omega) = Z'(\omega) + iZ''(\omega)$ is defined as the impedance, which is in dependence of the angular frequency $\omega = 2\pi f$ [90]. The conductivity of the toner material at a certain angular frequency $\kappa(\omega)$ is:

$$\kappa(\omega) = \frac{l}{Z(\omega)A}. \qquad \text{Eq. 4-7}$$

In case of conductive or semi-conductive materials the conductivity at low angular frequency converges to the value of the conductivity in the DC resistance measurement.

4.2.5 Scanning electron microscopy (SEM)

SEM is a method to visualize the particles and substrates with resolution in nanometer range. In this work several SEMs are used, *i.e.*, an Ultra 55 (Zeiss SMT, Oberkochen) at Zeiss Munich, a Joel 5900 LV (Joel, Tokyo, Japan) at the chair of electromicroscopy, TU Munich and a Jeol JSM 6400 (Jeol, Tokyo, Japan) at Chair for Surface Science and Corrosion, University of Erlangen. Furthermore, the chemical composition of some probes is investigated with an Energy-Dispersive X-Ray spectroscopy (EDX, EDAX/TSL Genesis 4000, Icon, India) at Chair for Surface Science and Corrosion, University of Erlangen. A comprehensive overview of the SEM and EDX methods can be found in Newbury [91].

4.2.6 Contact angle measurement

The surface energy of the substrates can be measured with a contact angle instrument. If the thermodynamic equilibrium between the three phases solid (S), liquid (L) and gas (G) is reached, the chemical potential in the three phases should be equal and the three phases should build a constant contact angle. The relationship between the interfacial energies γ_{SL}, γ_{SV} and γ_{LG} is given by the Young equation:

$$\gamma_{SG} - \gamma_{SL} - \gamma_{LG} \cos\theta = 0 . \qquad \text{Eq. 4-8}$$

In this work the contact angle is measured with an OCA20 (Dataphysics, Filderstadt) in the static mode to determine the surface energy of various substrate surfaces.

If two solid particles of materials A and B contact in vacuum or in air, the interfacial energy depends almost only on the surface energy of the interacting phases [8]:

$$\gamma_{AB} = \gamma_A + \gamma_B - 2\sqrt{\gamma_A \gamma_B} . \qquad \text{Eq. 4-9}$$

4.2.7 Measurement of the mechanical properties

4.2.7.1 DMA for the determination of bulk material properties

The mechanical properties of the polymer materials can be measured statically as well as dynamically. The static property, *i.e.*, the time-independent stress-strain behavior can be described with the elasticity-plasticity model. The static property of a material can be obtained by the classic tension test, in which the strain is a unique function of the stress. In case of polymer materials, the strain of the probe depends also on the applying time of the stress. Hence, it is a dynamic behavior. This behavior can be described with the viscoelasticity model. The viscoelasticity of polymer materials can be determined with the dynamic mechanical analysis (DMA) [92]. In the extension measurement for example, the probe is loaded with a sinusoidal stress $\sigma(t)$. The complex Young's modulus of the material is the ratio between $\sigma(t)$ and the response of the material $\varepsilon(t) = \Delta l(t) / l_0$:

$$E^* = E' + E'' = \frac{\sigma(t)}{\varepsilon(t)} = \left| E^* \right| \tan\delta . \qquad \text{Eq. 4-10}$$

Herein E' is the storage modulus and E'' is the loss modulus, respectively. $\tan\delta$ is defined as loss tangent. In the bending test the shear modulus is measured instead of the Young's modulus. The relationship between the complex Young's modulus and the complex shear modulus is:

$$G^* = \frac{E^*}{2(1+\nu)}, \qquad \text{Eq. 4-11}$$

where ν is the Poisson's number of the material. For polymer materials, the Poisson's number usually lies in the range $0.3 \sim 0.4$.

4.2.7.2 Nanoindentation for the determination of microscopic material properties

While the DMA measurement determines the macroscopic mechanic properties of the materials, nanoindentation measures the mechanical properties of the contact region (usually in an area of several μm^2). The indenter is mounted on a load-controlled displacement-sensing device. Basically, the dynamic behavior of the materials is not investigated in the conventional nanoindentation measurement. The indenter is driven into a sample and then withdrawn by decreasing the load to generate a load *vs.* depth of penetration plot. The mechanical properties of the material can be determined by fitting the load *vs.* depth curve. Oliver and Pharr [93] developed algorithms for the linear elastic–purely plastic material model (compare to the Rumpf model with plastic deformation, Paragraph 2.1.2.2) to fit the load *vs.* depth curves for different indenter geometries. The material is described with the two parameters: the elastic constant K and the Hertzian hardness p_{pl}^H.

The elastic constant K of the material can be obtained from the slope of the unloading curve $s = dF / dh$:

$$K = \frac{E}{1-\nu^2} = \frac{s}{2}\sqrt{\frac{\pi}{A}}, \qquad \text{Eq. 4-12}$$

where A is the projected contact area. The Hertzian hardness p_{pl}^H is the ratio of the maximal load to the projected contact area [94]:

$$p_{pl}^H = \frac{F_{max}}{A_{max}}. \qquad \text{Eq. 4-13}$$

The Hertzian hardness is usually significantly higher than the yield stress, where the plastic deformation begins.

The material behavior of a polymer is not exactly plastic. The deformation of the polymer material depends also on the time, it behaves to some degree also viscous. The viscoelasticity of polymer can be observed in the time domain in which the probe is loaded with a constant force, the displacement is recorded as a function of the time. The material behavior can be approximated with the Kelvin-Voigt model, which is represented by a purely viscous damper and a purely elastic spring connected in parallel:

$$\sigma(t) = E\varepsilon(t) + \eta \frac{d\varepsilon(t)}{dt}, \qquad \text{Eq. 4-14}$$

where $\varepsilon(t)$ is the strain and $\sigma(t)$ is the stress at the time t, η and E are the material properties coefficient of viscosity and Young's modulus, respectively.

If a constant stress σ_0 is suddenly applied to the material, the deformation would approach the deformation for the pure elastic material σ_0 / E with the difference decaying exponentially:

$$\varepsilon(t) = \frac{\sigma_0}{E}\left(1 - e^{-\lambda t}\right), \qquad \text{Eq. 4-15}$$

where $\lambda = E / \eta$ is the rate of relaxation.

The dynamic behavior of the material can also be measured in frequency domain applying the continuous stiffness measurement (CSM) technique, in which the load signal is superimposed by an oscillating force with force amplitudes generally several orders of magnitude smaller than the nominal load. The response amplitude and the phase angle resulting from the dynamic loading and unloading procedure are registered. The dynamic properties (*e.g.*, the storage modulus E' and the loss modulus E'') of the material can be determined as functions of the displacement into the probe. The nanoindentation method is explained in detail in a recent book of Fischer-Cripps [94].

The DMA measurements are carried out with a DMA 2980 (TA Instruments, New Castle, USA) in the single cantilever bending test mode. The nanoindentation measurements were carried out with a NANO Indenter XP (MTS, Eden Prairie, USA) equipped with the CSM extension and a 3-faces pyramidal Berkovich indenter tip or a flat punch of $50\,\mu m$ diameter at the Institute 1 of Material Science, University of Erlangen.

4.3 Methods for adhesion force measurements

Since various forces are of importance in the electrophotographic process, different measuring methods are applied to investigate those under well defined boundary conditions.

4.3.1 Atomic force microcopy (AFM) measurement

Traditionally, the AFM has been used as a nanoscale profilometer, as shown in Paragraph 4.2.1. Since an AFM scans the surfaces by sensing the repulsive force between the tip and the surface, the equipment can also be used to sense the

interaction forces between a particle and a substrate. Hereby the particle is fixed at the tip of a cantilever with known spring constant. Cappella [95] and Butt *et al.* [62], respectively, reviewed this measuring technique. In the frame of this work measurements were carried out with Nanoscope 3a (Digital Instruments, USA). Various cantilevers with different spring constants were applied in order to sense forces in a wide range from below $1nN$ to several μN.

4.3.1.1 Determination of spring constant of the cantilever

The spring constant of the cantilever depends on the geometry and on the Young's modulus [95]. Especially the thickness T of the cantilever has a strong impact on the spring constant as $k \propto T^3$. The cantilever thickness can always differ from a given specification, so that the spring constant – even within the same batch of the same type of cantilever – may vary significantly. Therefore, the cantilevers need to be calibrated individually. Here the spring constants of the cantilevers are determined with two methods: the thermal noise method is applied for soft cantilevers with spring constants below $0.1 N/m$; while for relatively hard cantilevers the added mass method is applied.

The thermal noise s of the cantilever is recorded in the contact mode. The spring tension of the cantilever k is equal to [96, 97]:

$$k = \frac{k_B T}{\langle s^2 \rangle}, \qquad \text{Eq. 4-16}$$

where k_B is the Boltzmann constant, T the temperature and $\langle s^2 \rangle$ the average in time of the quadric noise signal. To reach a high precision, this measurement has to be carried out in a silent environment. It has to be repeated at least 3 times. If the spring tension is large, the noise signal is very small (*e.g.*, the mean value of the noise is $|\bar{s}| \approx 0.06 nm$ for $k = 1 N/m$). This method may result in large errors. Hence, for the cantilevers with spring constants above $0.1 N/m$, the added mass method is more precise.

The added mass measurement is carried out in the tapping mode. Glass spheres with a density $\rho_{glass} = 2500 kg/m^3$ were attached to the cantilever whose radii were determined by an optical microscope. The resonance frequencies of the cantilever with and without an added mass were measured. The spring constant k can be calculated from the change of the resonance frequency [98]:

$$k = -\frac{2}{3}\pi^3 \rho_{glass} \frac{d_1^3}{f_1^{-2} - f_0^{-2}}, \qquad \text{Eq. 4-17}$$

where f_0 is the resonance frequency without the added mass and f_1 is the resonance frequency when the diameter of the added glass sphere is d_1. This measurement is repeated at least twice. An accuracy of $\leq 5\%$ can be achieved with this method.

4.3.1.2 Probe preparation

For the AFM-measurement the polymer particles (toner, polystyrene) are glued to the cantilever with epoxy resin while the oxide particles can also be sintered to the cantilever at high temperature ($900°C$). The particle is then treated as described in Paragraph 4.1.1. In the meanwhile, the substrate is treated according to Paragraph 4.1.2.

4.3.1.3 Humidity control during the measurement

For adhesion force measurements in a well defined atmosphere, the commercial liquid cell for the Nanoscope 3a is used. Before the measurements the cell is flushed with pure nitrogen (Messer Griesheim, 5.0) for at least $10 min$. During the measurements, in which the influence of the meniscus force is to be excluded, the cell continues to be flushed with pure nitrogen. To investigate the influence of the meniscus force, the measurements are carried out in the liquid cell flushed with moistened nitrogen with controlled relative humidity.

Concerning cantilevers with relatively large spring constants, *i.e.*, at least $0.5 N/m$, as used for the investigation of meniscus forces, the gas flow in the cell has no significant influence on the stability of the force-distance measurement.

4.3.1.4 Force measurement with an AFM

Particle-substrate adhesion forces are measured in contact mode. During this measurement, the cantilever is mounted in a standard cantilever holder or in a liquid cell and kept at a fixed position. The substrate is – driven by a piezo element – moved up- and downward. The deflection of the cantilever is detected optically with a four-section photodiode.

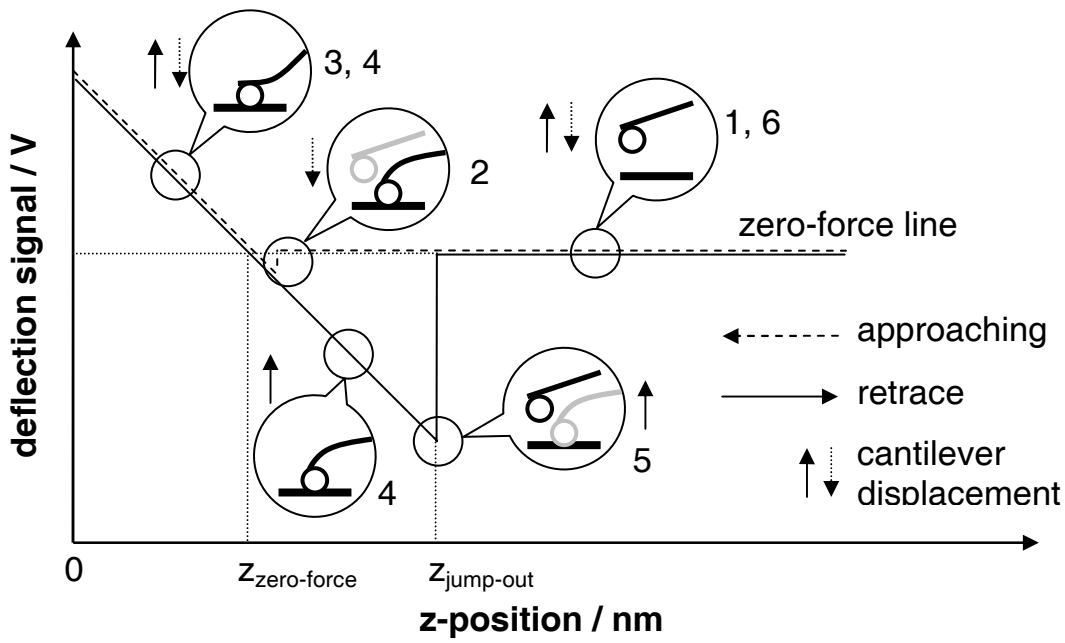

Figure 4-5 Schematic of the force-distance curve and the referring cantilever positions.

Figure 4-5 demonstrates the run of the force-distance curve measured with an AFM. The force-distance curve is actually ill-defined. The abscissa of the curve is the z-position of the fixed side of the cantilever and the ordinate is the deflection signal received by the four-section photodiode. At large separation, no interaction between the adhesion partners occurs; the cantilever deflection is equal to zero and the deflection signal remains constant (1). The particle approaches the substrate driven by a piezo element, at separation distance of several nm the particle-substrate interaction overcomes the spring tension of the cantilever. The particle jumps abruptly into contact with the substrate. This is observed as "jump-in" (2) in the force-distance curve. Then the particle moves upward (3) and downward (4) together with the substrate (deflection signal increases and then decreases). As soon as the spring tension of the cantilever overcomes the interaction forces between the adhesion partners, the particle separates abruptly from the surface, so called "jump-out" (5), the deflection of cantilever returns to zero (6).

The adhesion force is proportional to the spring tension of the cantilever at the moment of separation, it can be calculated with the Hooks law: $F_{adh} = -k \cdot l$, where k is the spring constant of the cantilever determined according to Paragraph 4.3.1.1, l is the cantilever deflection at "jump-out". Since in contact (curve 3-4) the cantilever deflection is equal to the displacement of the fixed side of the cantilever, it can be calculated from the difference between the z-position of the zero-force point – the intersection point of the curve (3-4) and the zero-force line (6) – and the z-position of the jump-out point: $l = z_{jump-out} - z_{zero-force}$. The maximal normal force applied in the measurement is the spring tension of the cantilever at $z = 0$, *i.e.*, the fixed side of the cantilever reaches the lowest point and the normal force is $F_N = k \cdot z_{zero-force}$.

4.3.2 Centrifugal detachment

While the AFM measures the adhesion force of a single particle with substrate, the adhesion force distribution of a particle ensemble can be measured with the centrifugal detachment method [6].

4.3.2.1 Probe preparation

To measure the adhesion force with the centrifuge the particles are brought onto the substrate surface in advance. To avoid normal forces during preparation the probe is prepared with the apparatus shown in Figure 4-6, left. The particles are dispersed in the space in the PMMA-hood with an impulse of compressed air at $4\,bar$ for $1\,s$, then the particles are allowed to settle down on the substrate surface. This apparatus is equipped with a sieve with mesh size of $25\,\mu m$, so that the large particles, for example the carrier particles in the toner-carrier mixture (see particle charging process, Paragraph 2.2.1.1), which are approximately $50\,\mu m$ in diameter, can be separated.

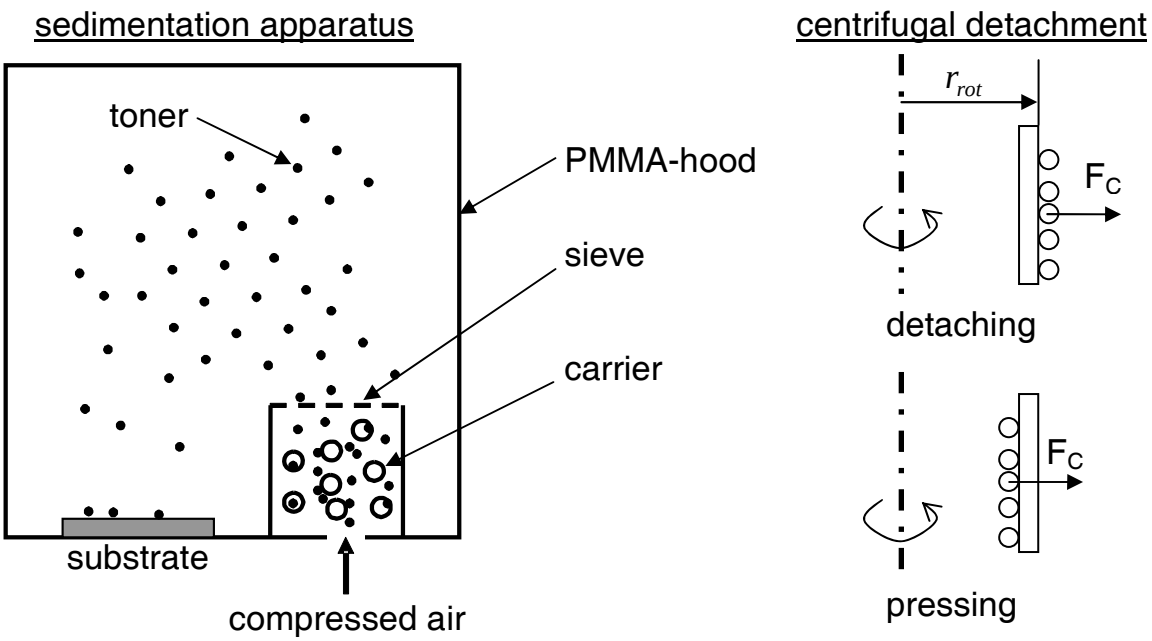

Figure 4-6 Schematic of the sedimentation apparatus for the dispersion of the toner particles on the substrate (left) and of the centrifugal detachment method (right).

4.3.2.2 Centrifuge measurement with image analysis

The centrifugal detachment measurements were carried out with an ultracentrifuge Sorvall Discovery 90 (Kendro Laboratory Products, Asheville, USA) at Lehrstuhl für Maschinen- und Apparatekunde, TU Munich. With a fixed-angle rotor T-890 it is possible to rotate the probes with a speed up to $90000\,rpm$. The probe is fixed vertically in a substrate holder, with the surface carrying the particles facing outwards as shown in Figure 4-6, top right. To realize a normal force on the particles the probe can also be centrifuged with the backside outwards (down right). The probe is

$r_{rot} = 59.5\,mm$ away from the rotation axis (shown in the figure as dash-dot line). During a measurement the particles are removed from the substrate along sequentially higher and higher rotation speeds. The detaching force at a certain angular velocity ω is:

$$F_C = Ma = \frac{\pi d^3 \rho}{6} r_{rot} \omega^2 , \qquad \text{Eq. 4-18}$$

where m is the mass of the particle, d is the diameter of the particle and ρ is the particle density. The density of the toner particles is $\rho = 1200\,kg/m^3$.

Prior to the first centrifugation step and after every centrifugation step a certain area on the substrate is scanned with a microscope (Leitz, Wetzlar) equipped with a high-resolution CCD camera and analyzed with the image analysis program ImageC™ (SiS, Stuttgart) to detect the particles remaining on the substrate. The area equivalent diameter d of each particle is registered for the calculation of the adhesion force distribution.

4.3.3 Electric field detachment

Electric field detachment measurement may be applied as well in order to measure the adhesion force of a particle ensemble. To carry out this measurement the particles are brought onto the substrate surface in advance with the apparatus shown in Figure 4-6 or with the q-test apparatus (Figure 4-4) according to their q/d-ratio. The electric field detachment measurement is carried out between two parallel electrodes. The substrate is connected as the lower electrode and an ITO-coated glass slice is used as counter electrode so that the measurement can be observed in-situ with an optical microscope (Figure 4-7). If a voltage U is applied between the electrodes, the field strength is:

$$E = U / D , \qquad \text{Eq. 4-19}$$

where D is the distance between the electrodes. The detaching force is the electric field force:

$$F = QE , \qquad \text{Eq. 4-20}$$

where Q is the particle charge.

Fukuchi [99] and Mizes [6] measured the transfer rate in term of the resultant current. The transferred charge from the lower electrode to the upper electrode in the interval $t + \Delta t$ is equal to the integral of the current during this period:

$$\int_{t}^{t+\Delta t} I_{jump}(t)\,dt = \sum_{1}^{n} Q_i\,, \qquad \text{Eq. 4-21}$$

This signal overlaps with the current of the capacitive charging, so the total current is:

$$I_{total}(t) = I_{jump}(t) + CdU/dt\,, \qquad \text{Eq. 4-22}$$

Since the particle charge is usually of the order of several fC, the current due to the toner jumping is very small. For example, if 100 particles, each of 10 fC jump within $1s$, the resultant current is merely $1\,pA$. Hence, large amounts of particles have to be measured to produce a measurable current. To assure that the particle-substrate and not the particle-particle layer adhesion force is measured, it is necessary to have two large coplanar electrodes, which is, however, not trivial. On the other hand, if measuring the behavior of thick particle layers, the electric field may be strongly distorted, so that the results obtained may be non-reliable.

In this work electric field detachment measurements are evaluated by means of image analysis. Measurements are carried out between particles and substrate. A sequentially increasing voltage is applied to the measuring cell during a certain period, and after each voltage level the amount of the detached particles is registered. With this method it is possible to investigate the detachment rate as a function of the particle size and the original q/d-ratio of the particles.

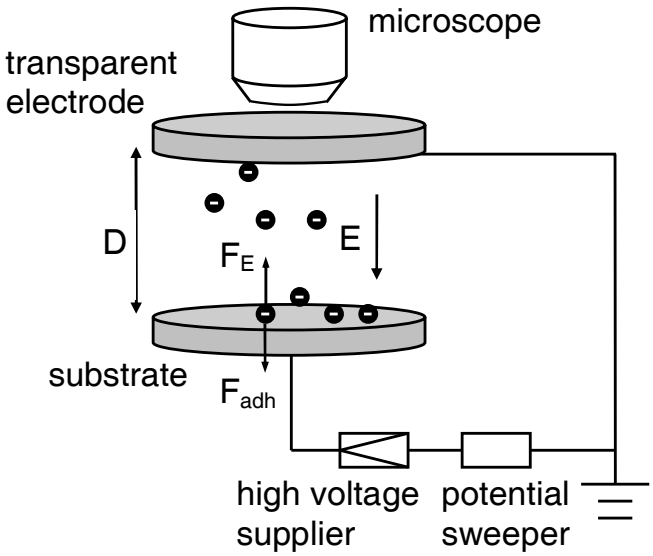

Figure 4-7 Setup of the electric field detachment method.

4.3.4 Comparison of the measuring methods

The application areas as well as the advantages and disadvantages of the three methods allowing to measure the adhesion force are summarized in Table 4-3 [6]:

Table 4-3 Comparison between the measuring methods

	AFM	Centrifugal detachment	Electric field detachment
Particle type	Charged / uncharged	Charged / uncharged	Charged
Statistic	Several particles	Particle ensemble	Particle ensemble
Advantages	- Possible to vary the normal force and contact time (from milliseconds to seconds); - Very high resolution; - Particle-particle measurements also possible; - Possible to control the humidity.	- Possible to vary the normal force and contact time (from minutes to hours); - Measures the adhesion force distribution of a particle ensemble.	- Similar to the real process; - Relatively short preparing and measuring period; - Concerning the charging of the particle on the electrode; - Measures the adhesion behavior of a particle ensemble.
Disadvantages	- Limited number of particles; - Relatively long preparing and measuring period.	- Long preparing and measuring period; - Working in open ambience, control of the temperature and humidity not possible.	- Adhesion force cannot be determined directly.

5 CHARACTERIZATION OF THE PARTICLES AND SURFACES

5.1 Topography of the investigated surfaces

The topography of the investigated surfaces is measured with AFM (Paragraph 4.2.1), and SEM imaging (Paragraph 4.2.5). Figure 5-1 shows the 3D surface profile of the OPC surface scanned with AFM (left) as well as its SEM image (right). The surface is almost atomically smooth, with rms-roughness of approximately $0.3nm$. However the OPC is an industrial product and some nano-sized dust particles remain on the OPC surface even after thorough cleaning with pure nitrogen. These particles can be observed on AFM as well as on SEM images.

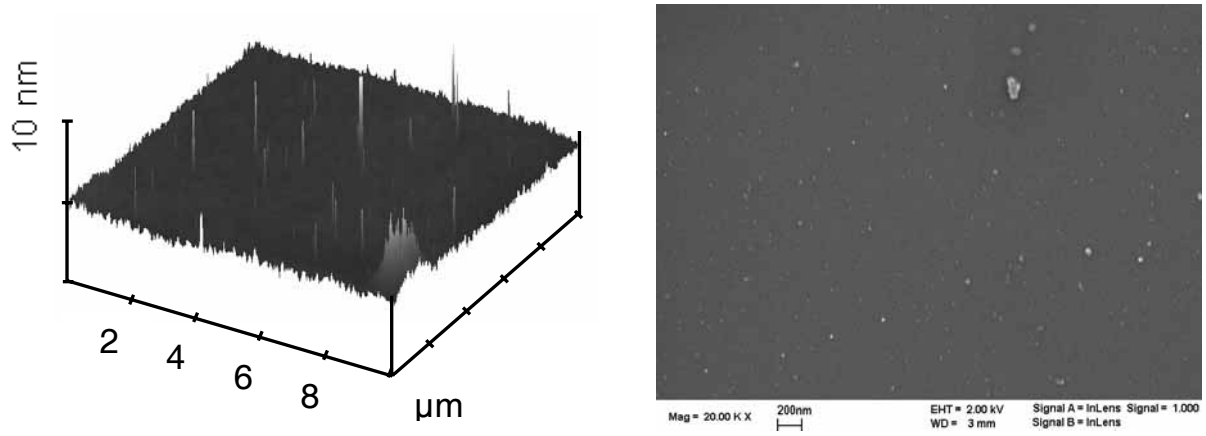

Figure 5-1 Left: Surface profile of OPC surface measured with AFM in contact mode, measuring range $10\mu m \times 10\mu m$; right: SEM image of OPC.

To understand the influence of the substrate surface roughness on the adhesion force, different model surfaces are tested during the adhesion force measurements. Three essential types of substrate morphologies can be characterized. The silicon wafer and the mica surfaces are nearly atomically smooth, with rms-roughness significantly below $0.3nm$. Roughness in this size range has little influence on the adhesion force between deformable adhesion partners. However, most technical surfaces are not smooth to nanometer scale. Polished surfaces, for example, usually have wave-form roughnesses. Figure 5-2 shows the surface profile of a polished aluminum substrate. In the left figure, a significant waviness of the surface can be observed. Because of the inhomogeneity of the polishing medium and the irregular motion of the probe during polishing the hill and valley structure of the surface is not regular. The roughness at a smaller scale of the polished surface can be highlighted through flattening in the post-procedure of the AFM-program “Nanoscope”, as shown in the right figure. Through the flattening the rms-roughness, which is evaluated in an area of $1\mu m \times 1\mu m$ with a resolution of 512×512 dots (Eq. 4-1), reduces from $7.4nm$ to $1.4nm$. Surfaces

coated by means of physical vapor deposition (PVD) usually have hill-form roughnesses (Figure 5-3). The rms-roughness of PVD-coated surfaces is around $28.7\,nm$. It is significantly higher than the one of the polished surface (Figure 5-2), furthermore, this value cannot be significantly reduced by flattening (from $28.7\,nm$ to $23.3\,nm$). The surface structure can be described as spherical segments on a flat surface. Usually, the center of each spherical segment is below the flat surface [32]. A typical value of the radius of a spherical segment is $100\,nm$, as shown in the 2D view in Figure 5-3, right.

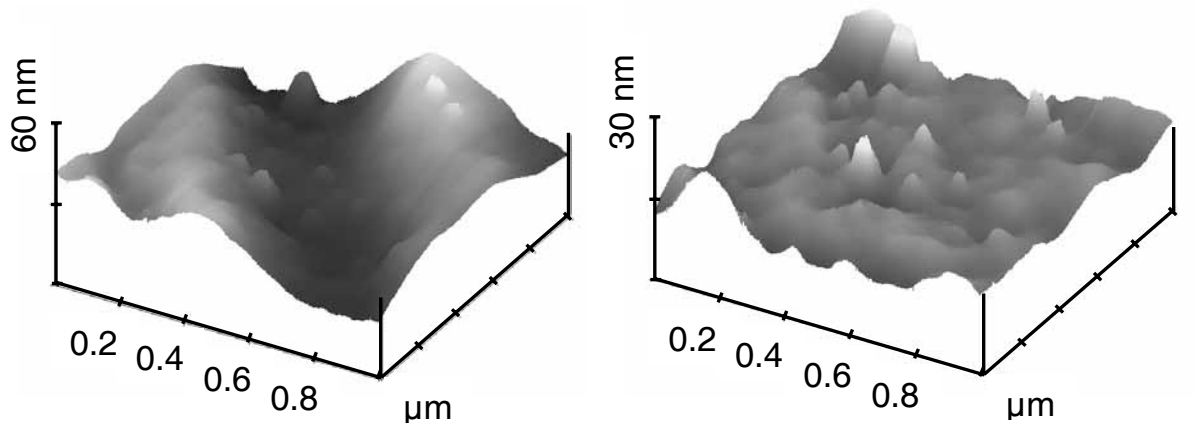

Figure 5-2 Surface profile of a polished aluminum substrate before (left) and after (right) flattening allowing for eliminating the waviness measured with AFM in tapping mode.

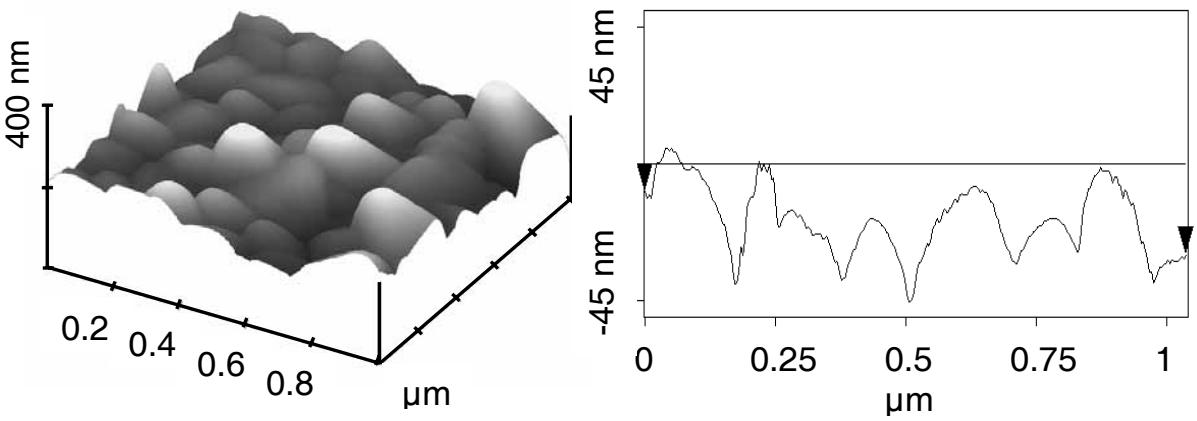

Figure 5-3 Surface profile of PVD-coated aluminum substrate measured with AFM in tapping mode. Left: 3D-view; right: 2D-view.

Substrates with well defined surface structure are produced through dip-coating with mono-disperse silica nano-particles [35, 74]. As shown in Figure 5-4 left, a nearly hexagonal closely-packed monolayer can be obtained if the surface is coated in a well stabilized suspension with mono-disperse silica particles of $250\,nm$ in diameter. In case of a suspension with silica particles of $110\,nm$ in diameter, a monolayer can still be built under the same coating condition. However, the structure is less well ordered (Figure 5-4 middle). If the particles are even smaller (*e.g.*, $34\,nm$), an irregularly structured layer is built, as shown in Figure 5-4 right. The irregular surface structure is first of all due to the influence of the interaction forces between the particles. A

further reason is that the smaller the particles are, the more difficult it is to get mono-disperse particles with regular particle shapes, which hinders the building of well structured surfaces.

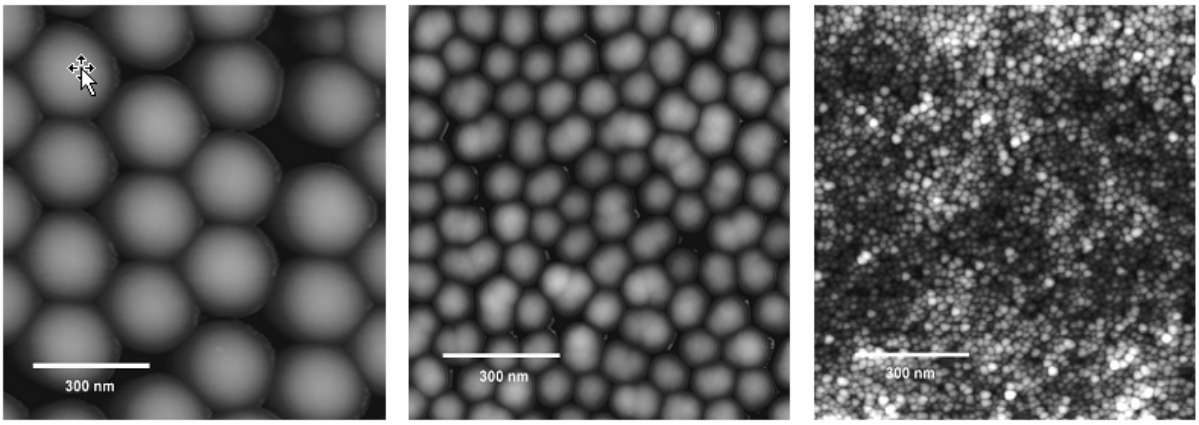

Figure 5-4 Surface profile of dip-coated silica substrate measured with AFM in tapping mode. From left to right: $250nm$, $110nm$, and $34nm$ silica coating.

The AFM-topography and SEM-image of an approximately $10\mu m$ toner particle is shown in Figure 5-5. The toner particles are usually irregular, the particles are produced through grinding and then they are coated with various additives (*e.g.*, pigments, charge control agents (CCA) [49] and oxide nano-particles – usually pyrogenic or precipitated silica particles – to tune the adhesion behavior). In both images of Figure 5-5 the nano-sized particles can be observed on the toner particle surface. Furthermore, EDX measurements indicate that the nano-particles are made of silica. In different toner types investigated in this work the average size of the silica particles varies from $10nm$ to $400nm$ and the surface coverage ranges from 10% to over 90%.

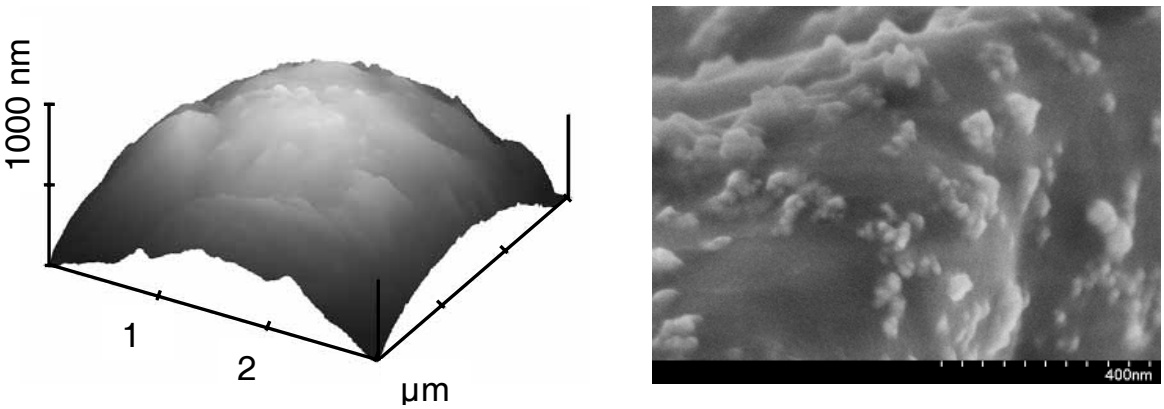

Figure 5-5 Surface profile of toner particle measured with AFM in tapping mode (left) and SEM-image of a toner particle surface (right).

Polystyrene particles (Postnova, Landsberg/Lech) and silica particles (flame synthesized at LFG or precipitated, Postnova, Landsberg/Lech) each with diameter of several microns are utilized as model particles for soft and hard particles. The polystyrene particles are nearly atomically smooth, they have usually perfect spherical

shape. The flame synthesized silica particles have also atomically smooth surfaces. However, the shape of the particles is not exactly spherical. The particle shape is affected by the surrounding air flow during particle cooling. The precipitated silica particles are neither smooth nor spherical. All the particles are imaged with AFM and SEM. The SEM images of silica particles on cantilever tips are shown in Figure 5-6, images of polystyrene particle can be found in Figure 4-1.

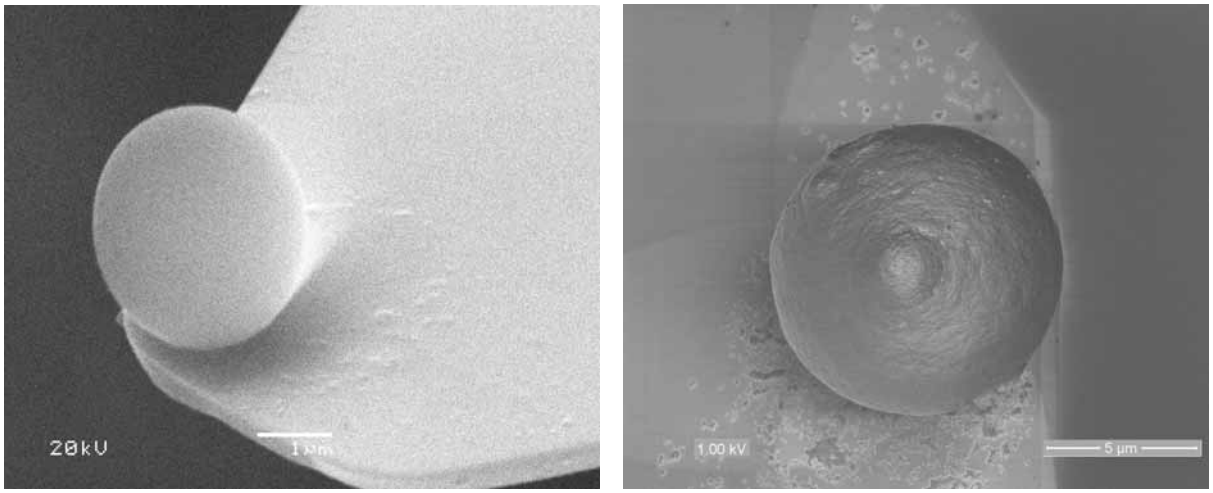

Figure 5-6 SEM images of flame synthesized (left) and precipitated (right) silica particles.

5.2 Charges on toner particles

5.2.1 Surface potential (SP) measurement

The charge distribution on the surface can be investigated with the SP measurement (Paragraph 4.2.2). At first the charge distribution on silicon wafers are measured. The surface can be triboelectrically charged. Hereby the wafer is mixed with carrier particles and agitated, similar as in the toner charging procedure of the laser printing process. Figure 5-7 right shows the surface potential of a randomly chosen area of the electrically charged wafer surface. The dark zones in the right image indicate the charged surface regions. A comparison between the topography and the potential image (there is always an asperity where there is a peak of surface potential) indicates that the charge transfer is usually accompanied with material transfer.

It can also be observed that the surface charge can be compensated if it is exposed to ambience. This measurement starts from the upper side of the image and runs downwards. The intensity of the surface charge reduces significantly within the duration of the measurement of approximately 2 hours.

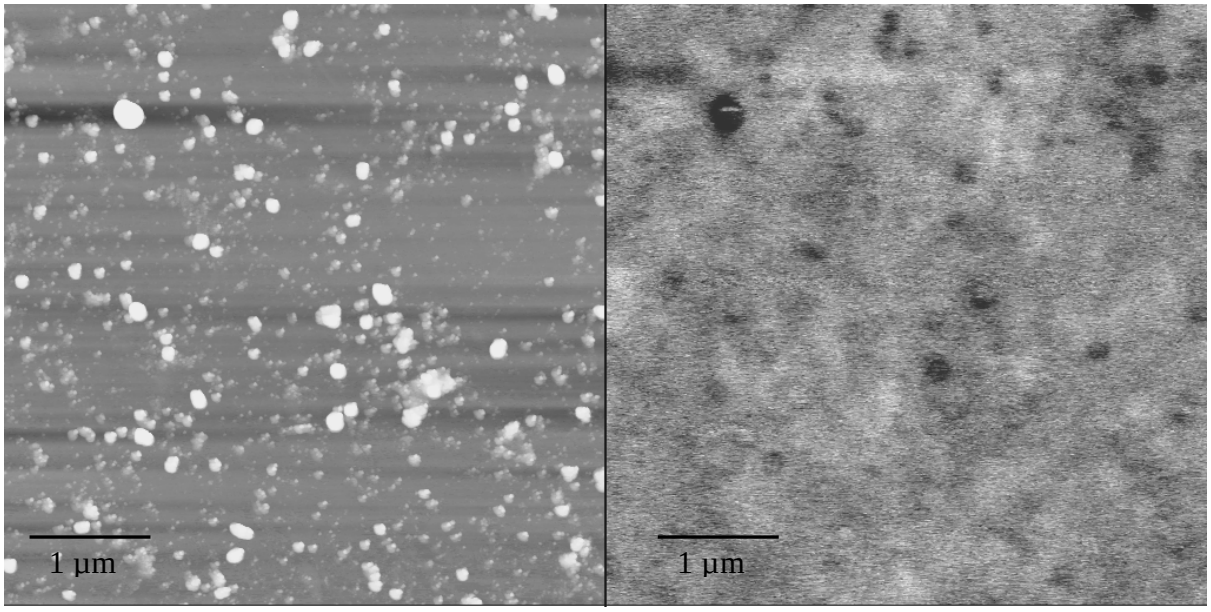

Figure 5-7 SP measurement of the surface charge on a triboelectrically charged silicon wafer. Scan size $5\mu m \times 5\mu m$; Left: topography image, $Z-$range $20nm$; right: surface potential image, $Z-$range $0.2V$, measured at a lift height of $20nm$ above the probe.

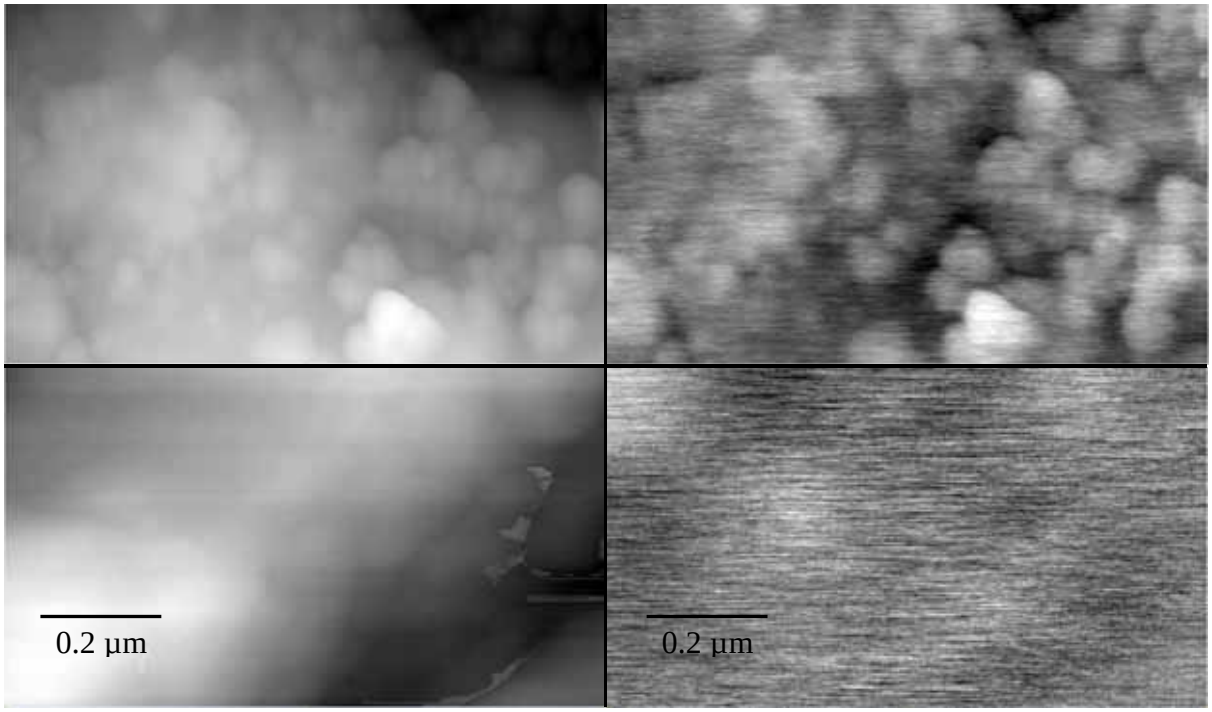

Figure 5-8 SP measurement of the surface charge of a triboelectrically charged toner particle. Scan size $1000nm \times 600nm$. Top: immediately after charging; bottom: 2 days after charging. Both measurements are carried out on the same particle. However, due to the thermal drift the position changes slightly. Left: topography, Z-range $250nm$; right: surface potential, Z-range $0.5V$ (top) and $0.1V$ (bottom). SP-Measurement is carried out at a lift height of $20nm$ above the probe.

The toner particles are charged triboelectrically. Hereby they are mixed with carrier particles (6 weight percent of toner) and agitated for $15 min$. Then the toner particles are transferred onto a piece of silicon wafer which is covered with a very thin layer of epoxy glue (no thicker than $1 \mu m$). SP measurement is carried out on a randomly chosen toner particle. Figure 5-8 shows the result of the SP measurement of a toner particle immediately after the charging process (top) as well as two days after charging (bottom). The charge density on the toner particle surface can be significantly higher than the charge density on the triboelectrically charged silicon wafer. The charges are mainly distributed on the asperities, where impact and sliding take place. As shown in Figure 5-8, bottom, the charge on the surfaces reduces to zero after the particle has been exposed to the ambient conditions for two days.

5.2.2 q-test measurements

The overall charging behavior of the toner particles is determined by applying the q-test (Paragraph 4.2.3). During this measurement the toner particles are triboelectrically charged in the same way as during the SP measurement. Figure 5-9 shows the particle charge distribution of the toner particles (magenta, without charge control agents, CCA) during the agitation period and several minutes after the probe has been agitated for $16 min$. The amount of toner particles in a certain q/d-interval is given by a pixel number as directly obtained from image analysis.

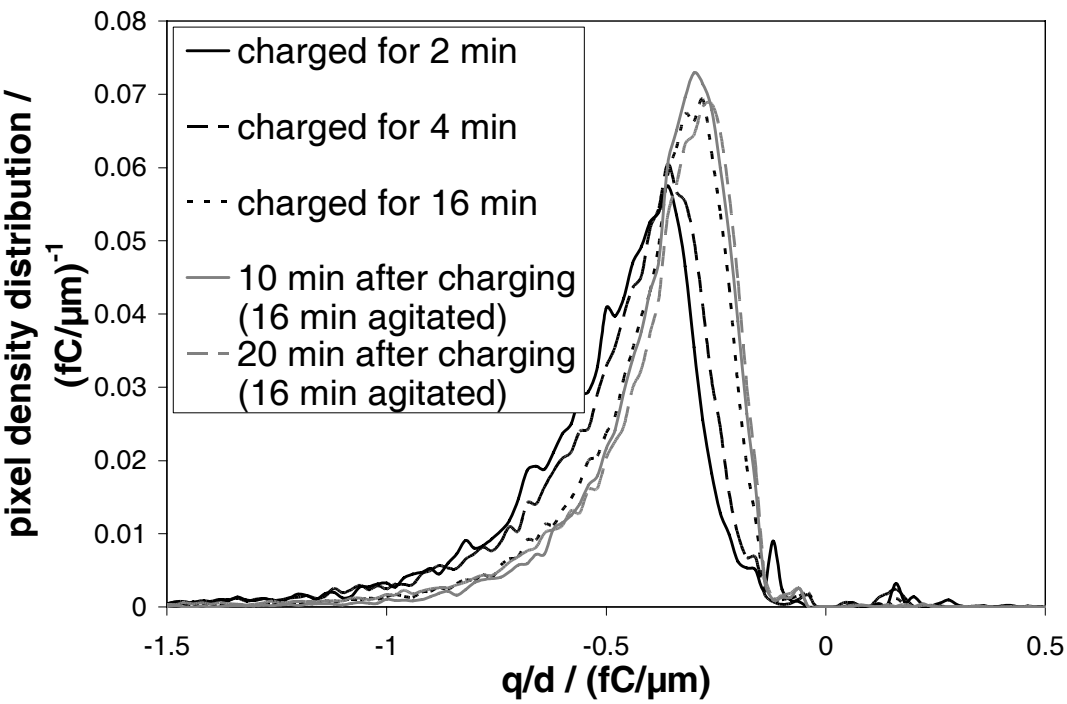

Figure 5-9 q-test measurement of triboelectrically charged toner particles (magenta, without CCA).

The toner particles seem to be already charged after a relatively short agitation period, *i.e.*, $2\,min$. However, the charge distribution of the particles is rather wide and up to 2% of the particles are charged positively. There also is a certain fraction of the particles which is charged to less than $\pm 0.04\ fC/\mu m$. The amount of these particles cannot be determined by means of this measuring technique. An increase of the agitation time results in a reduction of the width of the charge distribution. If the probe is agitated for more than $8\,min$, the charge distribution reaches an equilibrium situation. Surprisingly, in equilibrium the average value of the charge is smaller than after a short agitation time. This is possibly because the charge gained through impacting and friction is strongly localized, so that the highly charged surface area loses a part of its charge through contacting or air breakdown during the ongoing agitation process, until equilibrium is reached. The charge distribution remains also relative constant after the agitation process is stopped for a period of at least $40\,min$.

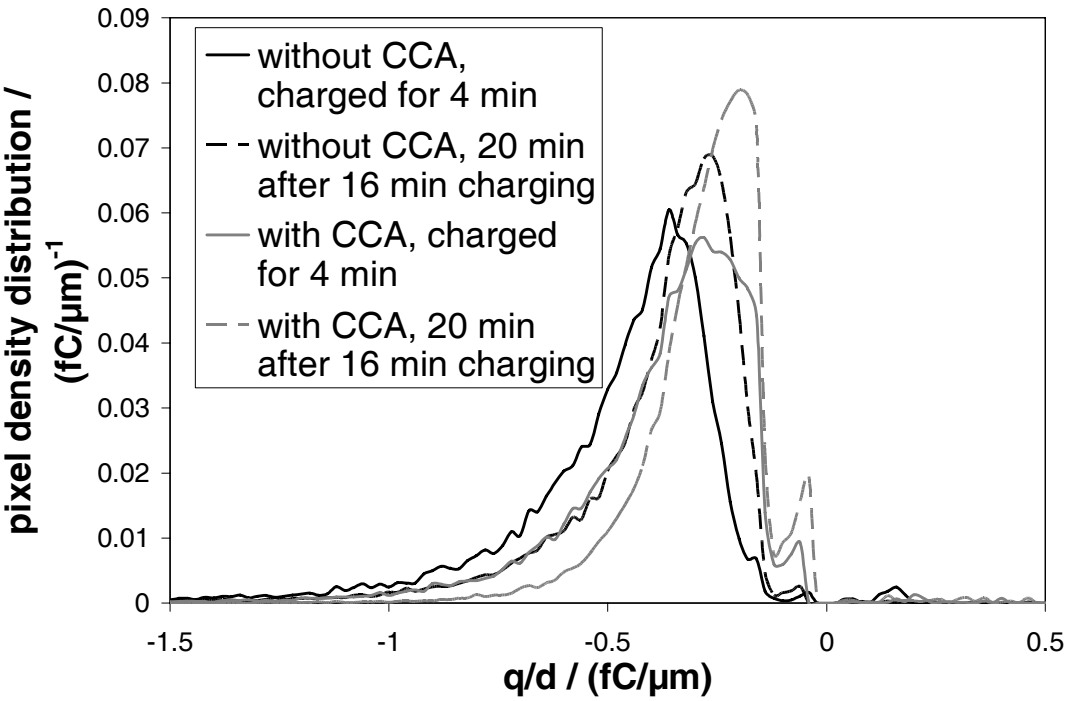

Figure 5-10 Comparison of the charge distribution of triboelectrically charged magenta toner particles with and without CCA. The measurements are carried out immediately after $4\,\text{min}$ agitation as well as $20\,\text{min}$ after a $16\,\text{min}$ long charging process, respectively.

As shown in Figure 5-10, the toner type magenta, with CCA has a similar behavior. The particle charge distribution of the toner particles is – at the same moment during charging or after charging – slightly narrower in comparison to the toner without CCA, and the mean value of q/d is smaller. A second peak in the range between -0.1 and $-0.04\ fC/\mu m$ can also be observed. In this range the particles are predominantly small particles ($<4\,\mu m$). It is reasonable that the particle charge is related to the particle surface area, which is proportional to the squared particle diameter d^2, therefore, smaller particles have smaller q/d-values, if the surface

charge density on the particles of different sizes is comparable. Considering that the pixel number is proportional to d^2, the amount of particles falling in this range is not minor. For the toner particles without CCA this part is significantly less and the particle charge distribution is wider. CCA improves the charge transfer between the particles so that the charge distributes on the surfaces of the toner particles turns out to be relatively homogeneously. Schein *et al.* [42] have also observed that the charge distribution of toner particles with CCA is narrower than without CCA in their "cage blow-off"-measurement, which measures the total charge amount of a sample of toner particles with defined mass. They found that the CCA results also in a higher q/M-value. This indicates that a large fraction of the toner particles without CCA is not charged, they just fly through the measuring chamber during the q-test measurement and are not characterized. This existence of CCA can significantly reduce this fraction. The same effect can be also achieved if the surface is covered with carbon black pigment, since carbon black has a sufficiently high conductivity.

5.3 Toner conductivity

5.3.1 The resistance measurement

The conductivity of the toner material is determined by means of the resistance measurement described in Paragraph 4.2.4.1. The toner particles are dispersed between the electrodes to form a $50-100\mu m$ thick, not fully closed layer. A DC voltage is applied on the both sides of the toner particle layer. The voltage is increased by $1V$-increments from $40V$ to $300V$ and then reduced to $40V$ again. Figure 5-11 shows the beginning of this measurement. Upon voltage changing, there is always a jump of the current passing through the electrodes. However, it asymptotically re-approaches the expected value rapidly.

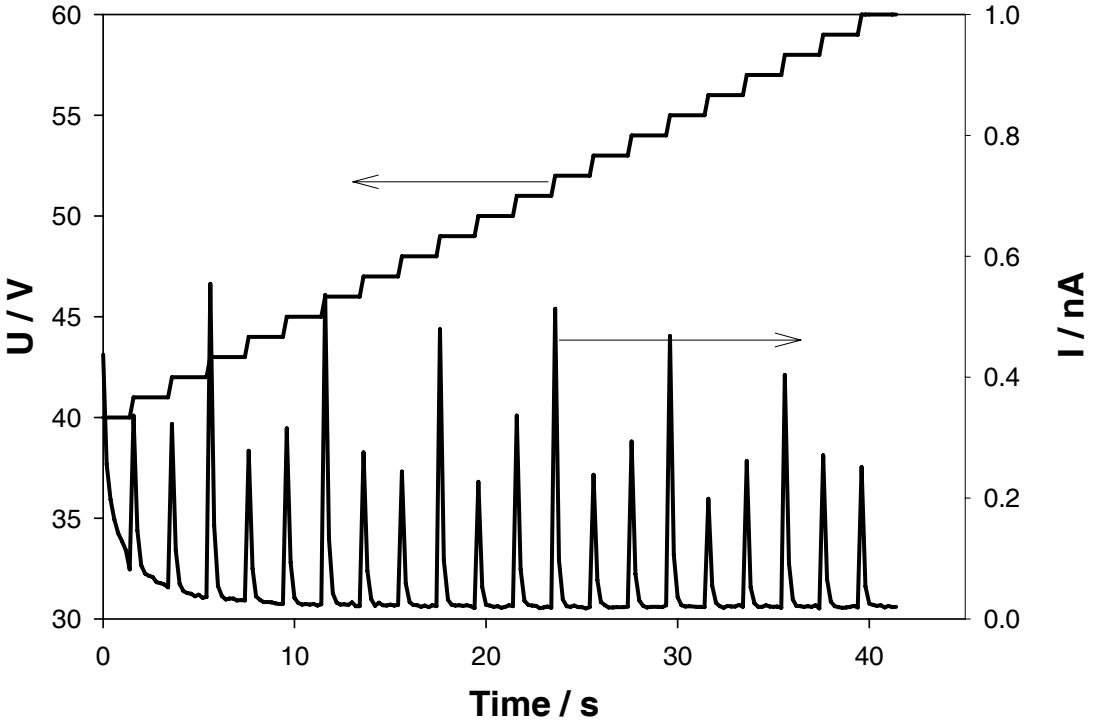

Figure 5-11 Resistance measurement of magenta toner without CCA. The voltage and the current are recorded as functions of time.

Despite of the jump of the current upon increasing the voltage, the current can be evaluated in terms of the voltage, such as shown in Figure 5-12. The current is in the pico-ampere range; in this measurement the thickness of the probe is approximately $70\,\mu m$ and the diameter of the toner probe is $20\,mm$. Fitting the curve “loose layer, voltage increases” with the Ohm's law $R = U / I$ leads to the resistance of the probe as $R = 2 \cdot 10^{12}\,\Omega$. If the probe can be regarded as homogeneous, the specific resistance of the toner layer is approximately $1 \cdot 10^{13}\,\Omega \cdot m$.

During the resistance measurements a hysteresis of the current can always be observed. This is because that the particles tend to capture charge faster than losing them later on upon decreasing the voltage. This phenomenon is less significant during the measurements with sintered ($60\,°C$, over night) toner probes, where the particles are fused together. The curves are also shown in Figure 5-12. This comparison indicates that the particles can be polarized in the electric field and that the charges are stored on the surfaces of the toner particles.

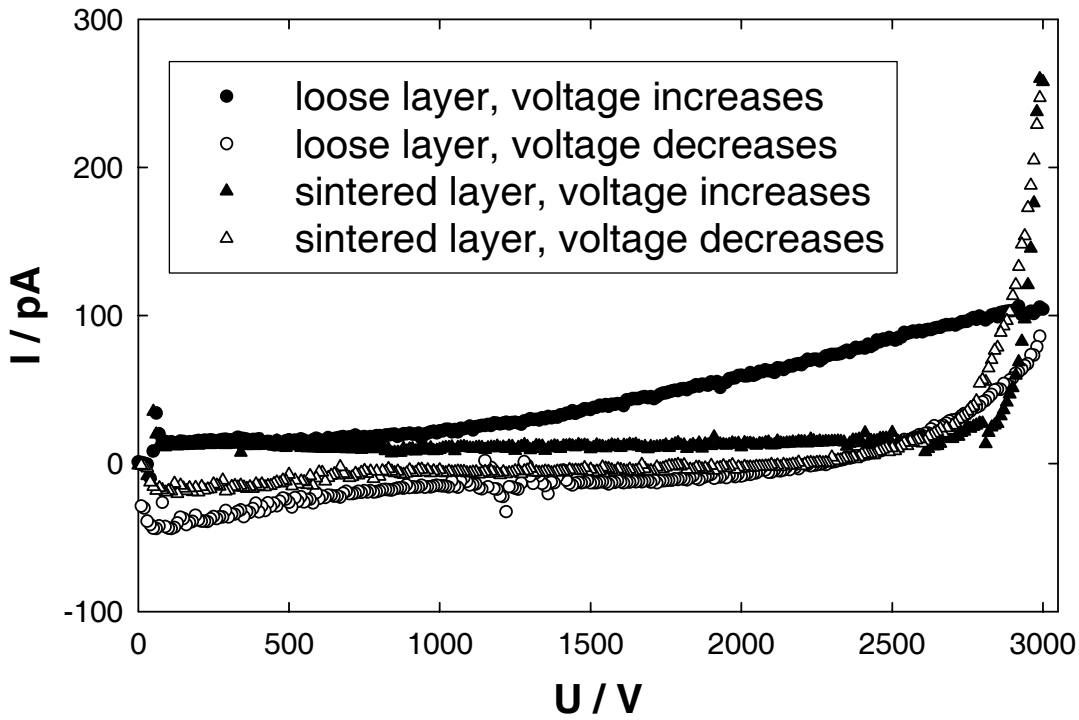

Figure 5-12 Resistance measurement of magenta toner without CCA, current flow through a toner layer ($70\mu m$ thick, $20mm$ diameter) is shown as a function of the applied voltage.

All measurements show the same tendency. Nevertheless, the reproducibility of the data is not satisfying. Even measurement of the same probe can differ by more than one order of magnitude. It is possible that the toner layer is changed when high voltage is applied. This measurement technique obviously provides insufficient accuracy for determining of the toner conductivity. Hence, it is necessary to carry out the impedance measurement with a broadband dielectric spectrometer at a significantly lower voltage level.

5.3.2 The impedance measurement

As introduced in Paragraph 4.2.4.2, the impedance of the probes can be given as a complex number $Zs = Zs'(f) + Zs''(f)$, both real and imaginary part of the impedance are functions of the measuring frequency f.

Various toner types are investigated by means of impedance measurement (Figure 5-13 and Figure 5-14). None of the magenta toner types investigated here has conductive components. CCA is an organic salt. Although showing a significant influence on the triboelectrical charging process (see Paragraph 4.2.3), it has only little influence on the conductivity of the toner particles. The addition of the conductive pigment carbon black causes only a small reduction of the impedance of the probe. Following Paragraph 4.2.4, the real part of the impedance normally tends to be constant in the low frequency range, and converges to the resistance of the probe as

in the resistance measurement. This is not the case during measurements with toner particles. The real part of the impedance increases monotonously as the measuring frequency decreases. The resistance of the toner layer is beyond the measuring range of the equipment. As shown in Figure 5-13, the real part of the impedance Zs' reaches at least a value of $3.5 \cdot 10^{11}\,\Omega$ (in the case of black toner). Considering the geometry of the toner layer the specific resistance of the toner sorts must be larger than:

$$\rho = \frac{RA}{l} = \frac{3.5 \cdot 10^{11}\,\Omega \cdot \pi \cdot (0.01m)^2}{70 \cdot 10^{-6}\,m} = 1.6 \cdot 10^{12}\,\Omega m\,. \qquad \text{Eq. 5-1}$$

The material shows negligible conductivity, if a constant DC-voltage is applied.

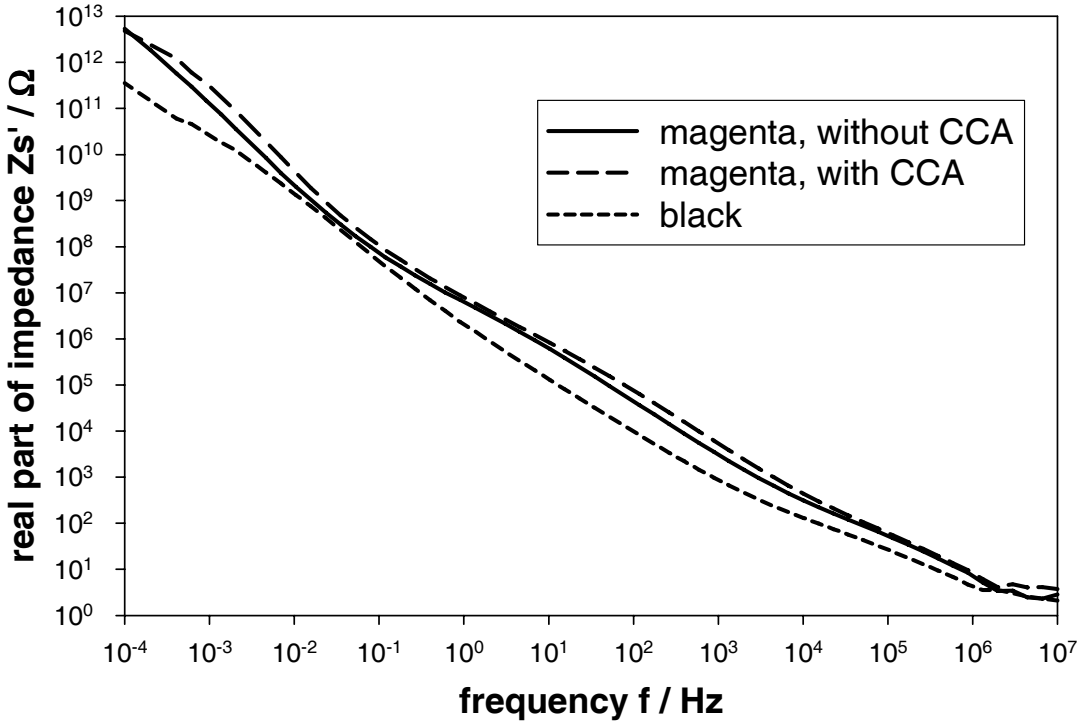

Figure 5-13 Real part Zs' of the impedance of layers of several toner sorts ($70\,\mu m$ thick, $20\,mm$ diameter) as a function of the measuring frequency.

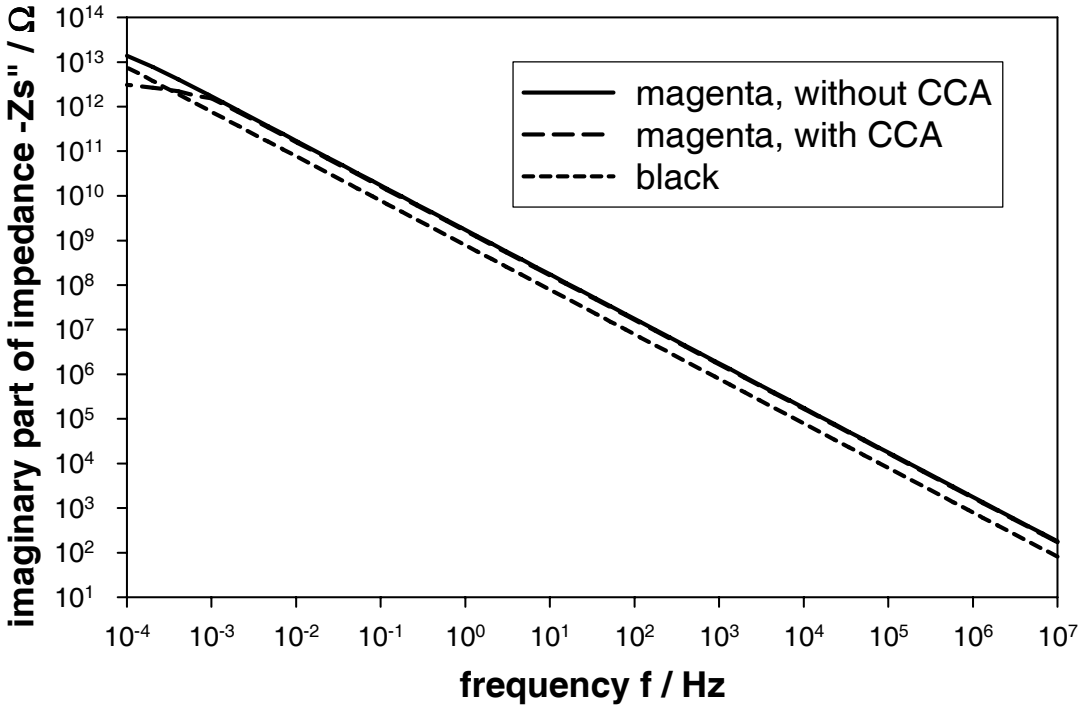

Figure 5-14 Imaginary part Zs'' of the impedance of several toner types as a function of the measuring frequency.

5.4 Surface chemistry and contact angle

The surface chemistry of the particles and the substrates cannot only be modified by various processes such as silanization but also by exposition to the ambient air. On the silicon wafer for example, directly after cleaning and heating (see Table 4-2), the contact angle of water on the wafer surface is less than $10°$. If the wafer surface is exposed to the air, the contact angle of water increases gradually to more than $20°$ after 2 hours and further to approximately $40°$ after 24 hours. Silicon wafers stored at ambient conditions have always oxidized surfaces. The surface groups prevailing on freshly cleaned and heated silicon wafers are shown in Figure 5-15 [100]. Surface silanol groups are the main centers of adsorption of water molecules. Water can associate through hydrogen bond formation with all types of surface silanols. The wafer surfaces are hydrophilic and have a high surface energy. During exposure to air, various substances can be adsorbed on the surfaces, so that the surface energy is significantly reduced and the contact angle increased.

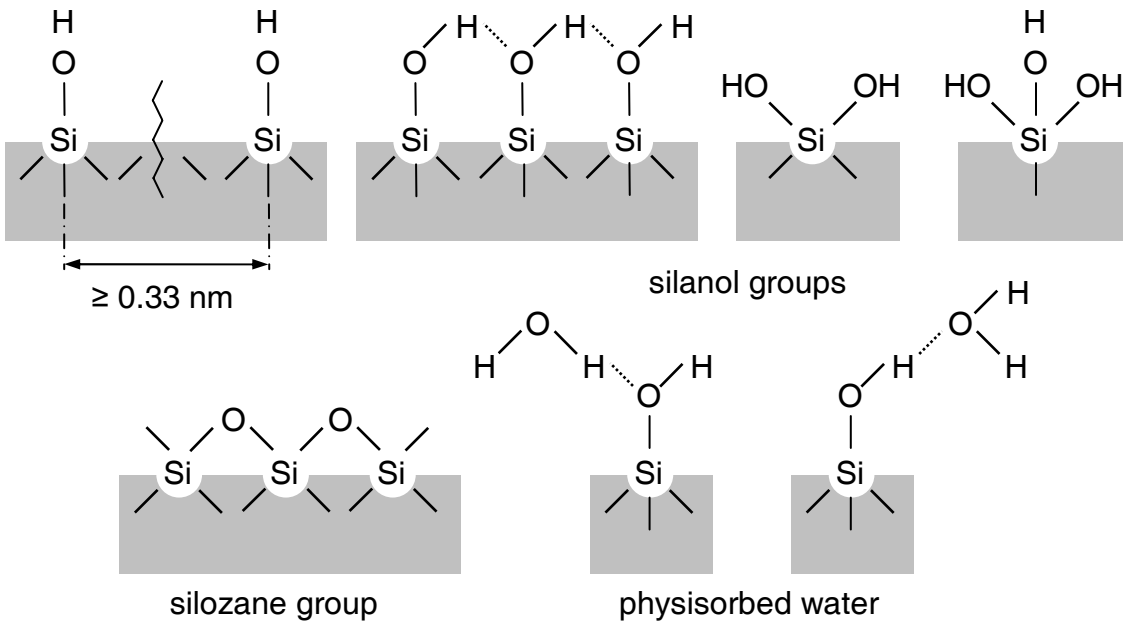

Figure 5-15 Possible types of silanol groups and siloxane bridges occurring on the surface of silicon wafer surface.

The measurements of the contact angle of a polystyrene surface are carried out on flat polystyrene probes. These flat probes are produced by pressing them against a silicon wafer while increasing the temperature to $150°C$ and then cooled down to the room temperature again. The surface rms-roughness is significantly below $1nm$. The contact angle of ultra-pure water on the polystyrene probes is usually in the range of $60 \pm 5°$. For comparison, the contact angle of water is on freshly cleaved mica surface approximately zero.

Investigating of the contact angle of other probes such as of toner or aluminum substrates does not make much sense, since, in case of rough and inhomogeneous surfaces, the contact angle is no longer a unique function of the surface energy.

5.5 Mechanical property of the materials

5.5.1 DMA measurements

The mechanical properties of toner material are determined with DMA (see Paragraph 4.2.7.1). The measurement is carried out with a frequency of $1Hz$ and a maximal strain of 1%. The complex Young's modulus $E*$ is derived from the complex shear modulus $G*$ according to Eq. 4-11. Figure 5-16 exemplarily shows the complex Young's modulus $E* = E' + E''$ of a certain toner type as a function of the measuring temperature. The toner types investigated within the frame of this work usually have similar mechanical behavior. The Young's modulus of toner is very sensitive to temperature. At room temperature the loss modulus E'' is negligible in comparison to

the storage modulus E'. The storage modulus reduces monotonously with increasing temperature, and around the glass transition temperature of circa $70°C$ the storage modulus decreases most rapidly whereas the loss modulus reaches its maximum.

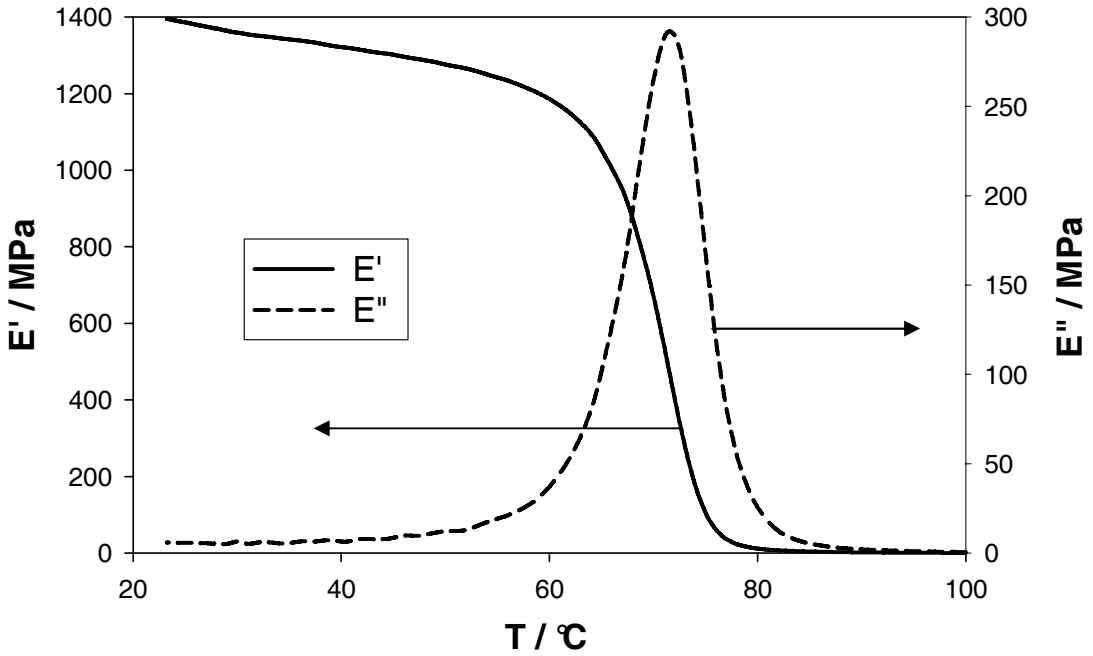

Figure 5-16 Complex Young's modulus of typical toner material in dependence of the temperature.

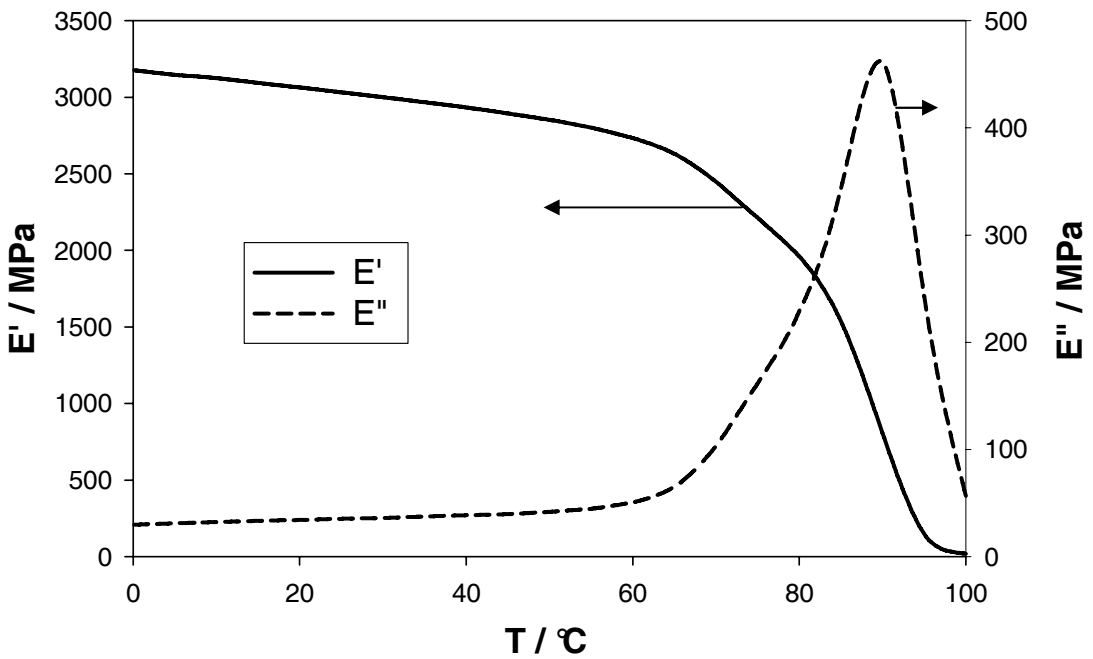

Figure 5-17 Complex Young's modulus of polystyrene in dependence of the temperature.

In comparison to toner, the model material, here polystyrene, has a higher Young's modulus, and the glass transition temperature shifts to approximately $90°C$. Both

materials have a glass transition temperature which is higher than room temperature. At room temperature the loss moduli are much smaller than the storage moduli. At $25°C$ the loss tangents $tan\delta = E''/E'$ of toner and polystyrene are 0.004 and 0.01, respectively. The viscous properties of the materials are irrelevant.

5.5.2 Nanoindentation measurements

Since the microscopic material properties of the region near the surface are more important for the adhesion behavior than the bulk properties, the microscopic material properties of polystyrene are studied with nanoindentation. Measurements were carried out on flat polystyrene surfaces with a Nano Indenter XP (MTS Systems) equipped with a 3-faces pyramidal Berkovich-indenter.

Polystyrene probes with smooth surfaces are produced by pressing them against silicon wafers at temperatures above the glass transition temperature, so that the surfaces are almost as smooth as the wafers. In this work the probes are heated to $150°C$ for approximately 1 hour and then cooled down slowly to room temperature in the oven, during the whole process the probes are pressed to silicon wafers by means of heavy weights. Finally they are kept at room temperature for several weeks, so that remaining internal stresses originating from the manufacturing process can be eliminated.

5.5.2.1 Frequency domain measurements

During the CSM measurement the indenter is vibrated at a frequency of $75Hz$ while it indents a depth of about $1000nm$ into the probe with increasing normal force. The storage modulus E' and the loss modulus E'' are recorded as functions of the displacement, as shown in Figure 5-18 and Figure 5-19. The Young's modulus obtained from the frequency domain measurement ($\overline{E}' = 4.49GPa$ averaged for 12 measurements in the range between 600 and $1000nm$) is significantly larger than the one obtained from DMA measurements. It can be also observed that the Young's modulus reduces slightly if the indentation depth increases. Klapperich [101] suggested that these phenomena are due to the rearrangement of the chains. This lowers the surface energy of the probe and thus results in a more organized surface layer, which has a higher elastic modulus than the bulk. This should not be the only reason. Otherwise, if the indentation depth reached several $100nm$, this surface effect should reduce to zero. An additional and maybe even more important reason is that the probe is not homogeneous, *i.e.*, the mechanical properties are determined by the failures in the structure [102]. During the indentation measurement, the stress is distributed in a very small region (maybe several μm^3) in comparison to the DMA measurement where the stress is distributed within the whole macroscopic probe. Accordingly, the probability for structure failure is – in the investigated region – much smaller so that the nanoindenter measures a higher modulus.

Although the applied normal force (circa $5mN$) is not significantly larger than the dispersion force between the indenter and the probe, the latter one may be – according to the simulation (see Section 3.2) – expected to be of the order of $\sim 1mN$. However, since the amplitude of the vibration rarely exceeds several nm, the dispersion force, which is directly related to the contact area, remains approximately constant during one cycle of the vibration. Hence, the dispersion force does not have a significant impact on the measurement. The loss tangent in this measurement is 0.02, *i.e.*, not much larger than 0.01 as obtained from the DMA measurement.

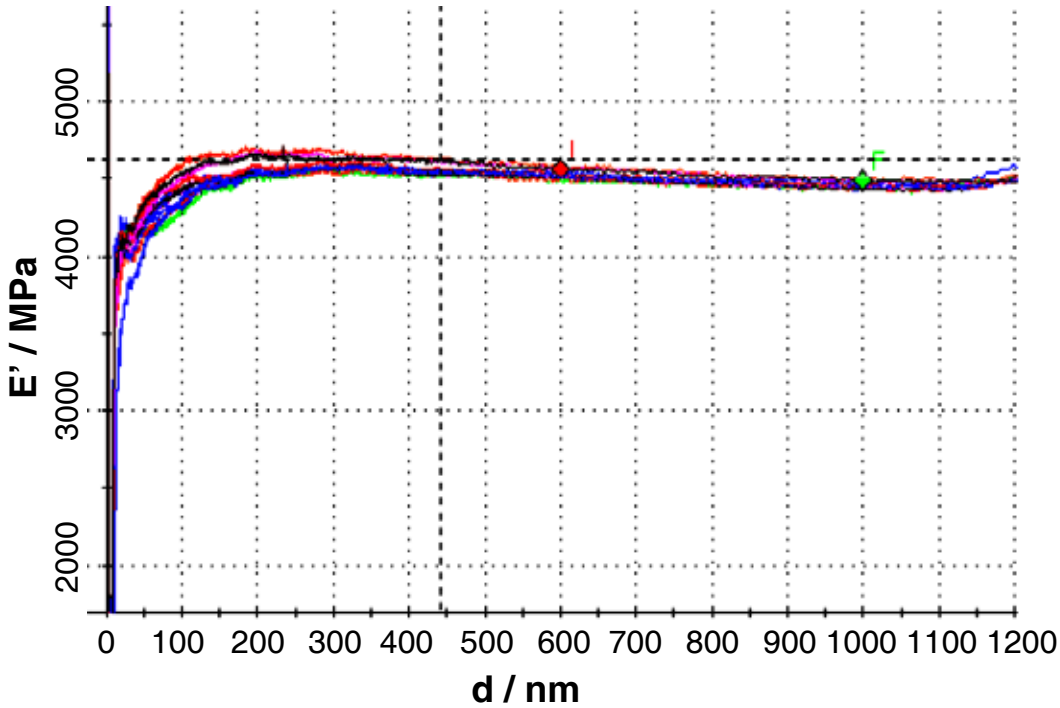

Figure 5-18 Storage modulus of polystyrene at room temperature as a function of the displacement measured with nanoindentation applying the CSM technique (12 measurements are shown).

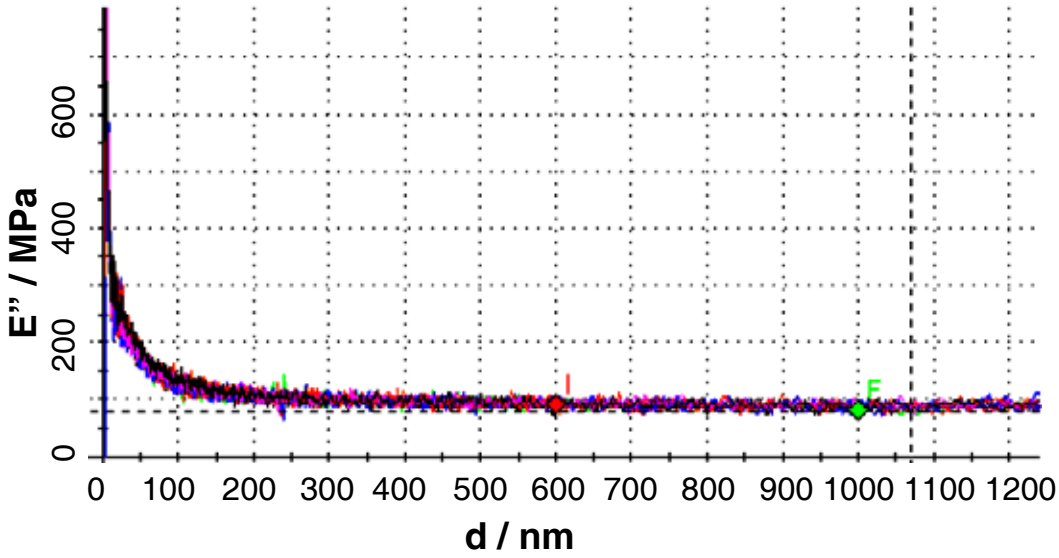

Figure 5-19 Loss modulus of polystyrene at room temperature as a function of the displacement measured with nanoindentation applying the CSM technique (12 measurements are shown).

The hardness of the material as obtained from the indentation measurements is derived from the unload segment of the tests (Eq. 4-13). The mean value of the hardness is $H = 0.27 \pm 0.01 GPa$.

5.5.2.2 Time domain measurements

In this work the viscoelasticity of polystyrene is also determined within the time domain. Figure 5-20 shows the change of the displacement obtained of the load is quickly set to certain value and then kept constant there. The displacement does not remain constant while the load is kept constant. It shows a time dependent behavior, which will be discussed in detail in the rest of this paragraph. Besides, the deformation observed in section b does not go back to zero, if the load vanishes. The plastic deformation remains permanent, as it is irreversible.

During a nanoindentation measurement the strain is not exactly known and the load cannot be suddenly applied at time zero. Considering that the strain $\varepsilon(t)$ is proportional to the displacement $\delta(t)$ as measured during the indentation, Eq. 4-15 can be converted into:

$$\frac{\delta(t)-\delta_0}{\delta(t_s)-\delta_0} = \frac{1-exp(-\lambda(t-t_0))}{1-exp(-\lambda(t_s-t_0))}. \qquad \text{Eq. 5-2}$$

Here δ_0 is the displacement at the time t_0, just before a load is applied; $\delta(t_s)$ is the displacement at an arbitrary starting point t_s chosen within the period during which the load is kept constant.

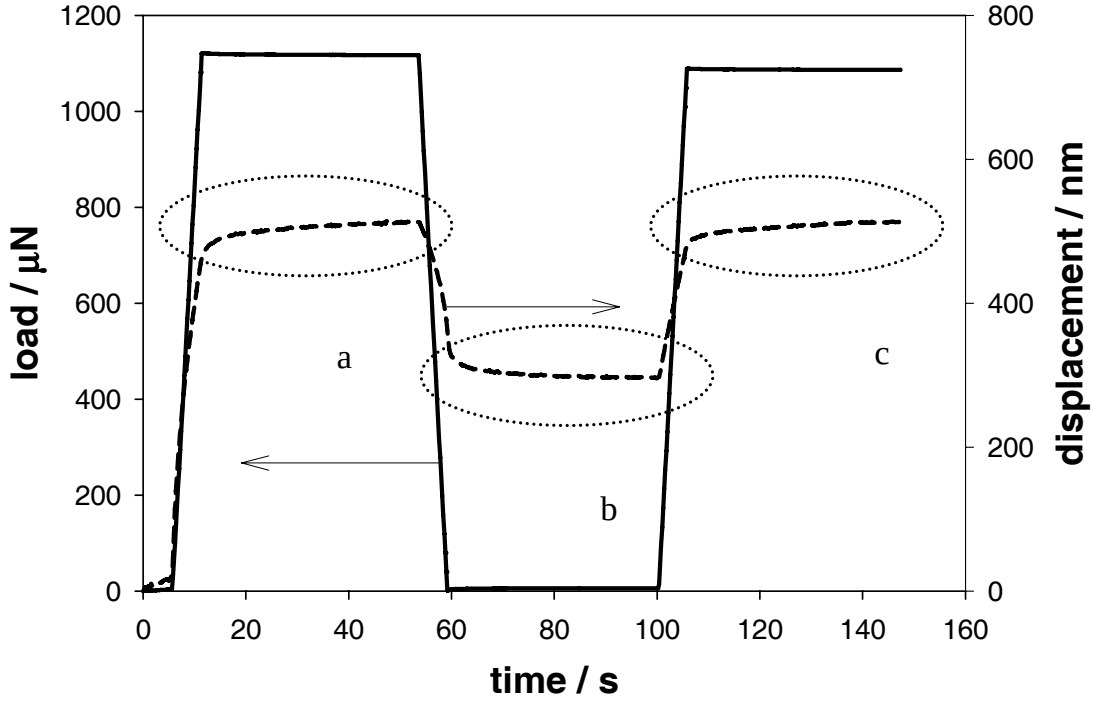

Figure 5-20 Time domain indentation measurement of polystyrene. The three segments characterized by a constant load are labeled with a, b and c.

Eq. 5-2 is represented by the dashed curve in Figure 5-21. It does not give a perfect fit for the measurement of section a. This is due to the fact that the polymers are more viscoplastic than viscoelastic. If the viscoplastic deformation can be described with a simple linear function:

$$\delta_{plas}(t) = m \cdot t, \qquad \text{Eq. 5-3}$$

wherein m is the time constant of the viscoplastic deformation, then the displacement-time behavior of polystyrene can be well described with the parameters $\lambda = 0.51 s^{-1}$ and $m = 0.43 nm/s$, as shown by the solid curve of Figure 5-21. In this measurement the contact radius and accordingly the dispersion force is kept constant. The increase of the dispersion force during the approach procedure seems to be slow in comparison to the material response of polystyrene. The system becomes more viscous than in the time domain and the DMA measurements.

This model gives estimation for the time scale at which the deformation takes place. The rate of relaxation of this fitting curve is $\lambda = 0.51 s^{-1}$, accordingly the relaxation time is $t_{rel} = 1/\lambda = 2 s$, which indicates that the deformation takes place mainly in the first few seconds. Afterwards, the viscoplastic deformation continues to take place, but the rate of the deformation reduces significantly. It is $0.43 nm/s$ in comparison to the displacement of $20 nm$ during the first $2 s$ which is related to the viscoelastic deformation. If the contact time during the adhesion force measurement with AFM

can be controlled within the frame of approximately $2 \sim 10\,s$, it is not necessary to consider the time dependence of the deformation. The material can be regarded as being plastic.

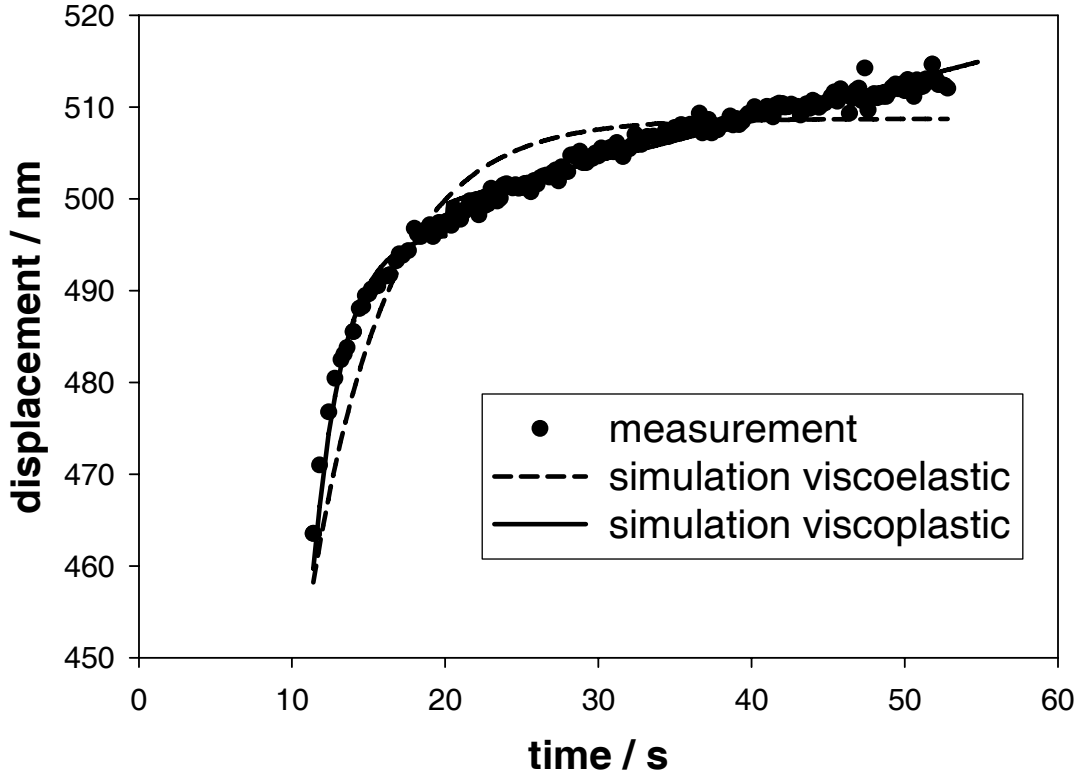

Figure 5-21 Fitting of the load *vs.* time curve section a as obtained from Figure 5-20 with the viscoelastic and viscoplastic model.

Upon carrying out the time domain measurement, the Young's modulus and the Hertzian hardness of the probe can be determined from the unloading curve (see Paragraph 4.2.7.2). For example, between the sections a and b, their values are $E = 4.0\,GPa$ and $p_{pl}^{H} = 0.22\,GPa$, respectively.

6 ADHESION FORCE BETWEEN PARTICLES AND SUBSTRATES

6.1 Van der Waals forces between smooth adhesion partners

6.1.1 Rigid adhesion partners

Sintered silica particles (see Figure 5-6, left) and silicon wafers are considered as rigid smooth adhesion partners within the frame of this work. The van der Waals force between a $10\,\mu m$ smooth silica particle and a certain position on a silicon wafer is measured with AFM. To avoid the influence of the capillary force the measurement is carried out in a fluid cell (Digital Instruments, USA) flushed with pure nitrogen (5.0, Messer, Sulzbach). The influence of the electrostatic interaction is minimized by means of earthening both adhesion partners. During the measurement the applied normal force is gradually increased from approximately $5\,\mu N$ to over $20\,\mu N$ and then reduced stepwise to $5\,\mu N$ again by varying the position of the zero-force point in the force-distance curve (Paragraph 4.3.1.4). At each normal force range the measurement is carried out 49 times (each measurement takes $20\,s$, the contact time depends on the $z-$position of the jump-in and the jump-out). The average value of the adhesion force is shown in Figure 6-1 as the function of the normal force. The deviation of the force is negligible and hence not shown.

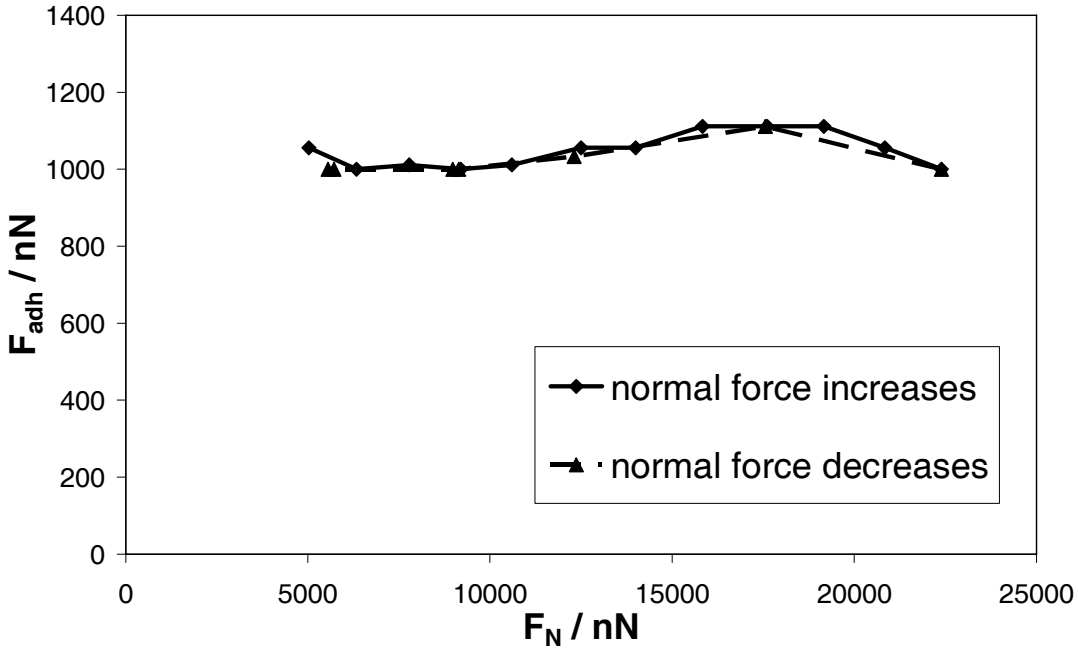

Figure 6-1 Adhesion force between a smooth sintered silica particle and a smooth silicon wafer as a function of the applied normal force.

Since the adhesion partners are almost rigid – more precisely, they show purely elastic behavior with very high Young's modulus ($E = 75GPa$, with the Poisson's number $\nu = 0.17$ [69]), they do not deform inelastically when they are pressed together, so that the adhesion force between the adhesion partners barely depends on the normal force. If the normal force is increased, the adhesion force does not increase monotonously with the normal force; and if the normal force is reduced from the maximal value, the correlation between the normal and the adhesion force remains the same. Obviously, the normal force does not lead to plastic deformation of the adhesion partners. The observed variation of the measured adhesion force value is nearly entirely due to the non-linearity of the piezo element and not due to deformation.

However, the adhesion force between the adhesion partners depends sensitively on the contact geometry. Since the sintered silica particles are not perfectly spherical, the adhesion forces of individual silica particles differ significantly from each other as well as from the theoretical prediction of the Hamaker model (Paragraph 2.1.1). The result obtained from the numerical simulation described in Paragraph 3.2.4 is similar to the prediction of the Hamaker model. No dependence of the adhesion force on the applied normal force is expected.

6.1.2 Deformable adhesion partners

6.1.2.1 Influence of the contact time

In the AFM measurement the contact refers to three steps: approaching after jump-in, delay between approaching and retrace and retrace before jump out. In this measurement the approaching and retrace velocities are kept constant at $1.2\mu m/s$. The time is mainly controlled by varying the delay between approaching and retrace.

While the adhesion force between the smooth silica particle and the silicon wafer depends almost not on the contact time, for adhesion partners, such as the polymers, the influence of the contact time on the adhesion force is significant. As shown in Figure 6-2, the adhesion force between a $10\mu m$ smooth polystyrene particle (Figure 4-1, right) and a silicon wafer increases by a factor of 1.4, if the contact time is increased from $0.005s$ to $2s$. This is mainly due to the viscoplastic [103] behavior of the polystyrene, *i.e.*, due to the time-dependent deformation of the material, as described in Paragraph 2.1.2.2 [29]. Fortunately, the variation of the adhesion force is not too strong, as the contact time is ranging between 2 and $20s$, which is of the order of the relaxation time t_{rel} (see Paragraph 5.5.2.2). At this time scale the deformation of the particle increases relatively slowly with time, so that the influence of the contact time on the adhesion force is relatively insignificant.

In order to ensure the comparability of the measuring results, all further AFM-measurements between polystyrene particles and silicon wafers are carried out with

contact times within this range and the approaching and the retrace velocity are kept constant at $1.2\,\mu m/s$.

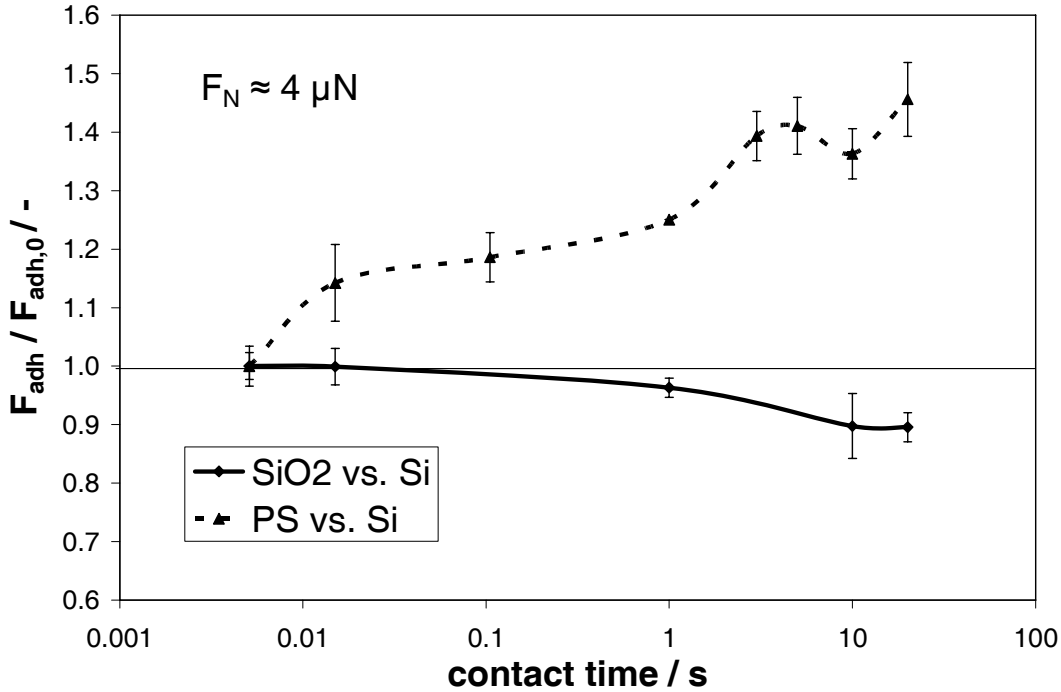

Figure 6-2 Adhesion forces between a rigid (silica) particle, a deformable (polystyrene) particle, and a silicon wafer in dependence of the contact time during the AFM-measurement.

6.1.2.2 Influence of the normal force

Between plastically deformable adhesion partners the applied normal force has a significant influence on the adhesion force. During the AFM-measurement between a $10\,\mu m$ smooth polystyrene particle and a silicon wafer the adhesion force is measured while the normal force is increased from 2 to $10\,\mu N$ and then reduced vice versa. The corresponding forces are represented by the solid curve in Figure 6-3. While the normal force is increasing, the adhesion force also increases, because of the growing importance of the plastic deformation, which results in an increase of the contact area. However, the plastic deformation remains later on while the normal force is reduced. Therefore, the adhesion force remains at a high level.

The results obtained from the AFM-measurement are compared with the predictions of the numerical simulation (see Figure 3-4), as described in Paragraph 3.2.3. The bilinear plastic model is applied for two different Young's moduli, namely $3.3\,GPa$ and $4.0\,GPa$, respectively. The value of $3.3\,GPa$ and the plastic behavior are taken from the CAMPUS®-Database for polystyrene 158K (BASF) at $23°C$. The value of $4.0\,GPa$ is obtained from the nanoindentation measurement of the material in the time domain (Paragraph 5.5.2.2). The simulations describe the measurements quantitatively with errors smaller than 20% in the whole normal force range [64]. An even higher accuracy can be expected, if more accurate material properties are available.

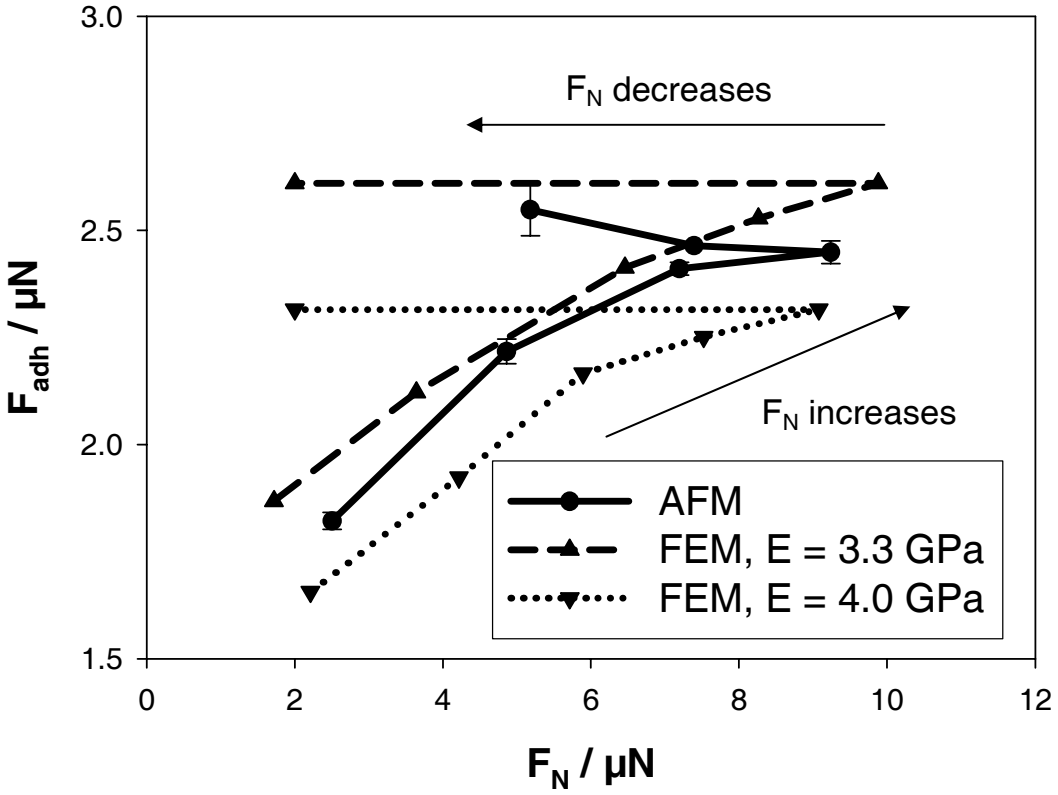

Figure 6-3 Adhesion force between a polystyrene particle and silicon wafer in dependence of the applied normal force measured with AFM. In the measurement, the normal force is increased gradually, and then decreased. For comparison, the results of the FEM-simulations are also shown.

6.2 Van der Waals forces between rough adhesion partners

6.2.1 Reduction of the adhesion force due to the surface roughness

The adhesion force can be reduced by the surface roughness of the contact partners, as discussed in theoretical [30, 32, 37] as well as experimental [6, 33, 75] studies. AFM-measurements were carried out between a dyed (hence rough, with irregular roughness of approximately $10\,nm$ in size) polystyrene particle and various surfaces. In these measurements the normal force is kept as small as possible, usually $<100\,nN$. The median value of the adhesion forces between the particle and the silicon wafer is $155\,nN$ and thus significantly smaller than the value between a smooth polystyrene particle and a silicon wafer which is approximately $1800\,nN$ (see Figure 6-3). If the substrate is also rough, the adhesion force may be even smaller. The median value then reduces to $153\,nN$ for the same, *i.e.*, polystyrene particle on the polished aluminum substrate and to $29\,nN$ on the PVD coated aluminum substrate. Because of the oxidation of the substrate surfaces, the surfaces of the aluminum and silicon

substrates can be regarded as alumina and silica layers, respectively. The Hamaker constant of the alumina layer is even significantly higher than that of the silica surface [10]. The obtained reduction of the adhesion force between particle and substrate is mainly due to the surface roughness. The influence of the roughness is studied in detail in the following.

6.2.2 Distribution of the adhesion force due to the roughness

The roughness also has a significant influence on the distribution of the adhesion force. While the adhesion forces measured between the smooth polystyrene particle and the silicon wafer as well as between the dyed polystyrene particle and the silicon wafer have quite a narrow distribution, the adhesion force measured on the aluminum substrates are widely distributed. Two types of adhesion force distributions can be characterized, as shown in Figure 6-4 [104]. On the polished aluminum substrate the adhesion force has a bimodal distribution. In most of the cases an adhesion force similar to the one on the silicon wafer is measured, while on several positions on the substrate a significantly smaller adhesion force is detected. On the PVD-coated aluminum substrate the adhesion force stretches from below $10\,nN$ to around $140\,nN$, its distribution can be fitted with a log-normal curve [105] with the following sum function:

$$Sum(F_{adh}) = \frac{1}{\sigma_L \sqrt{2\pi}} \int_{-\infty}^{\log F_{adh}} exp\left(-\frac{(t-\mu_L)^2}{2\sigma_L^2}\right) dt \quad , \qquad \text{Eq. 6-1}$$

where μ_L and σ_L^2 are the fitting parameters. The expected value μ and the variance σ^2 of the distribution depend on the parameters μ_L and σ_L^2:

$$\mu = exp\left(\mu_L + \frac{\sigma_L^2}{2}\right) \qquad \text{Eq. 6-2}$$

and

$$\sigma^2 = \left(exp\,\sigma_L^2 - 1\right) exp\left(2\mu_L + \sigma_L^2\right). \qquad \text{Eq. 6-3}$$

For the adhesion force between the dyed polystyrene particle and the PVD coated aluminum substrate the expected value and the variance are $\mu = 39.3\,nN$ and $\sigma^2 = 823.7\,nN^2$, respectively.

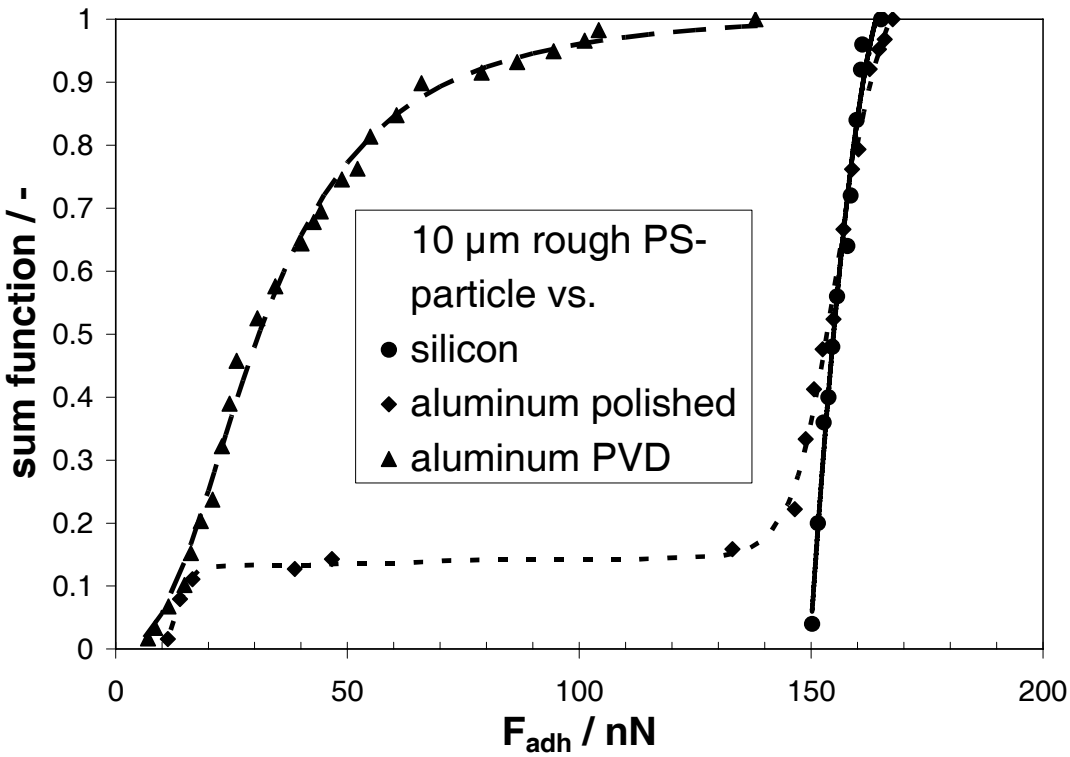

Figure 6-4 Adhesion force distribution of a rough polystyrene particle on various substrates: silicon wafer, polished aluminum substrate as well as the PVD-coated aluminum substrate.

These different behaviors are due to the different roughness characteristic of the surfaces. On the silicon wafer, where the surface is almost atomically smooth, the adhesion force is independent from the position of the particle on the substrate surface. Only the geometry of the particle surface is decisive for the adhesion. This is not the case for the adhesion force between the particle and the rough surfaces of the aluminum substrates.

The polished aluminum surface has a wave-like surface structure, such as shown in Figure 5-2, left, and the peak-to-peak distance between the waves is so large that the particle easily fits between two such peaks (see Figure 6-5). This structure does not result in a significant reduction of the adhesion force between the substrate and a particle on it. The resulting bimodal adhesion force distribution with several very small adhesion force values is due to the superposition of the wave shape with a hemispherical roughness profile (see Figure 5-2). The small adhesion force values are measured most likely at positions characterized by a nano-sized sphere exactly in the contact region. The surface of the PVD coated aluminum substrate has a layer of hemispherical asperities. This configuration allows the significant reduction of the adhesion force. Since the radii of the asperities and the peak-to-peak distances are random, such as shown in Figure 5-3 as well as in Figure 6-5, the adhesion force exhibits a wide distribution.

Designing a well defined roughness profile with hemispherical asperities on the surfaces of the adhesion partners is the most important manner to control the adhesion force. In the Paragraphs 6.2.5 to 6.2.7 the influence of the size of the asperities and their peak-to-peak distance on the adhesion force (distribution) will be discussed in detail. Prior to these investigations the influences of the measuring conditions, such as the contact time and the applied normal force, are validated.

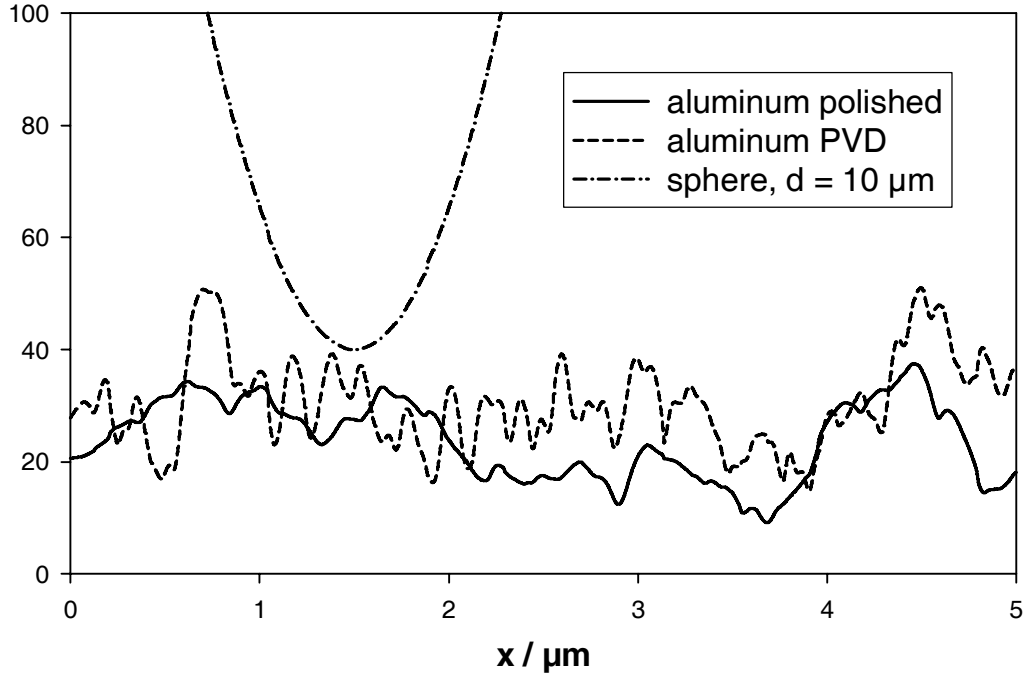

Figure 6-5 The surface profiles of the polished and the PVD coated aluminum substrates in comparison to the profile of a $10\mu m$ sphere.

6.2.3 Influence of the contact time and history on the adhesion force

Because of the viscoplastic behavior of polystyrene, an influence of the contact time on the adhesion force between rough surfaces can be also observed (cf. influence of the contact time between smooth adhesion partners, Paragraph 6.1.2.1). As shown in Figure 6-6, an increase of the contact time from $0.007s$ to $0.1s$ at a comparable normal force range of $\sim 30nN$ only results in a slight increase of the adhesion force between a polystyrene particle and PVD-coated aluminum substrate. The increase of the adhesion force along the contact time is a little bit more significant, if the applied normal force is larger. For example, if the normal force is approximately $300nN$, an increase of the contact time from $0.08s$ to $0.3s$ causes a more significant shift of the adhesion force distribution towards larger values. However, a further increase of the contact time to $0.9s$ does not have any effect on the adhesion force distribution. The time scale here is smaller than the one observed between smooth adhesion partners as in Paragraph 6.1.2.1. To allow for comparing AFM-measurements between

polystyrene particles and different rough surfaces the contact time is always kept at around $1s$, and if not mentioned otherwise, the normal force is controlled as to be kept in the range of several $100nN$.

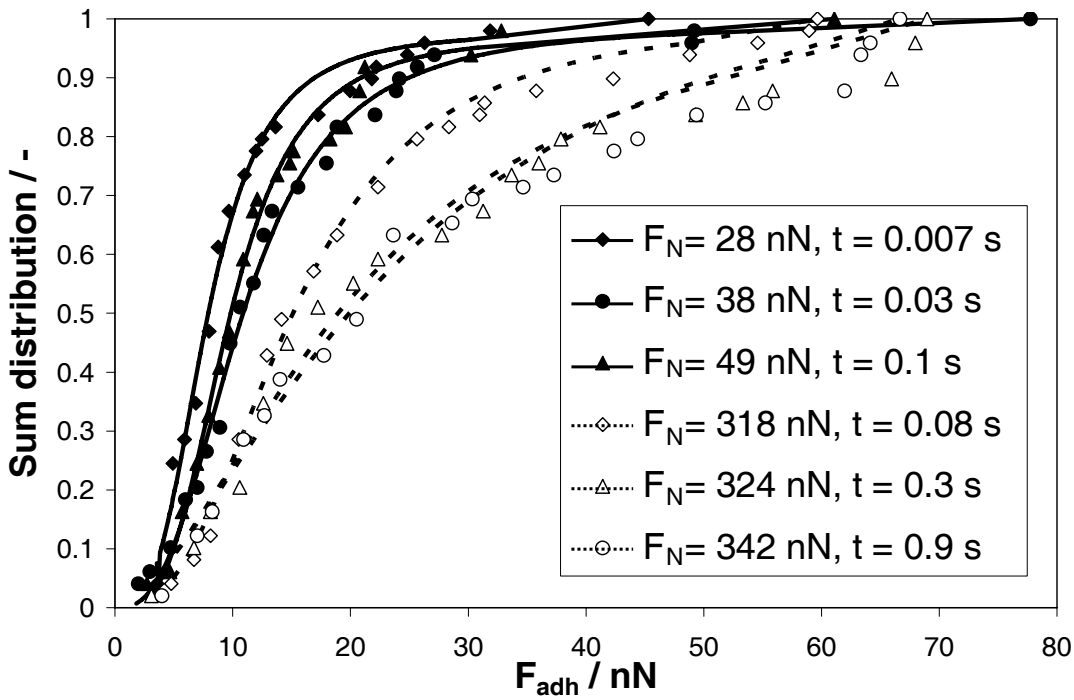

Figure 6-6 Adhesion force distribution between a polystyrene particle and a PVD coated aluminum substrate in dependence of the applied normal force and the contact time. This measurement is carried out with two normal force ranges, in each normal force range three different contact times are tested.

The contact history also leaves some traces on the particle surface. If for example, a particle contacts a rough surface, the stress in the contact region is usually so high that the material deforms plastically. After each measurement the contact area shows a modified roughness profile. This corresponding plastic deformation always will influence the following measurements carried out with the same particle. Figure 6-7 depicts – as an example – the adhesion force between a polystyrene particle and a surface coated with $34nm$ silica nano-particles right after preparation and after carrying out a measurement with this particle and a glass particle, which is glued on an aluminum substrate. After the measurement on the glass particle the median value of the adhesion force increases and the distribution gets wider. A possible reason for this phenomenon is that the measurement results in the strong deformation of the contact region of the polystyrene particle. There will be always some concave positions on the surface. If these happen to get into contact with a convex particle, the contact area can be increased, so that the adhesion force increases as well. This increase can be observed during all the measurements carried out with different polystyrene particles. Unfortunately, the preparation required for AFM-measurements is so time-consuming that it is not possible to prepare one particle only for one single

force-distance curve. To minimize the effect of the contact history on the AFM-measurement, the measurements including polystyrene particles or other deformable particles are usually carried out in such a way that – if the variation of the normal force is a key-issue – it is increased sequentially. If the influence of the roughness constitutes the key-issue, then the measurement is carried out on the smooth silicon wafer at first, and later on the rough surfaces with decreasing asperity size. After the measurement carried out on the substrate with minimal asperity size the particle is no more used.

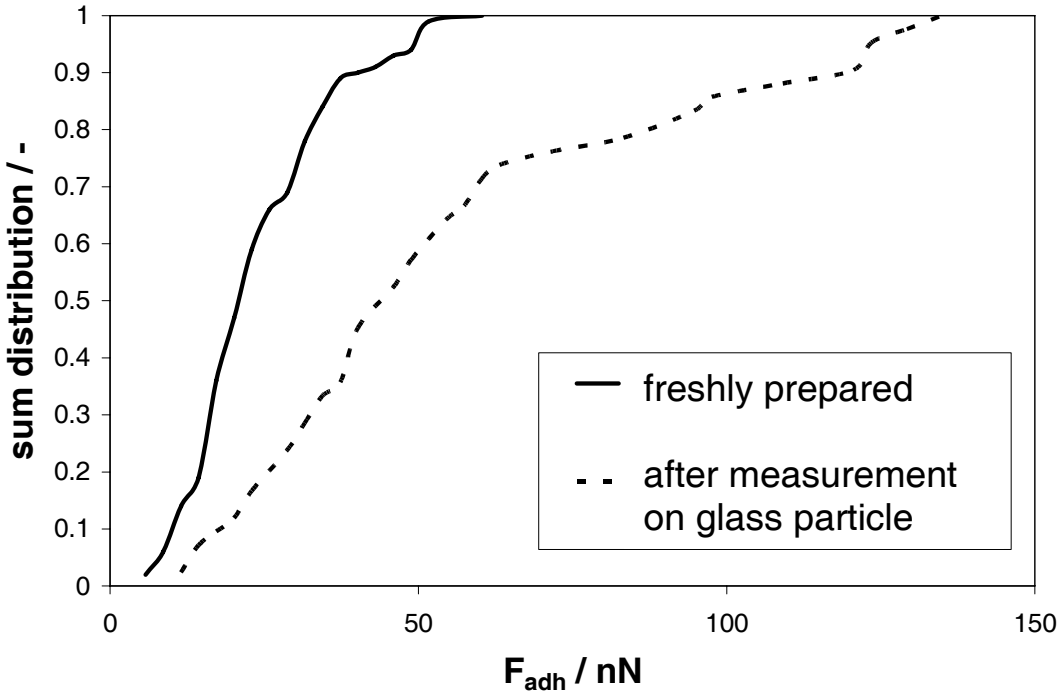

Figure 6-7 Adhesion force distributions between a polystyrene particle and a wafer surface (coated with $34\,nm$ silica nano-particles coating) before and after carrying out the measurement with the same particle on a glass particle.

6.2.4 Influence of the normal force on the adhesion force

The dependence of the adhesion force on the applied normal force can also be observed during AFM-measurements between rough adhesion partners, as shown in Figure 6-8. This measurement is carried out with a measuring frequency $1\,Hz$. For rough, plastically deformable adhesion partners the correlation between normal and adhesion force really differs from the one obtained between the smooth adhesion partners (Figure 6-3). The adhesion increases significantly as long as the normal force values remain relatively small. In this regime, the adhesion force increases from $F_{adh} = 80\,nN$ to $160\,nN$ if the normal force is gradually increased from $500\,nN$ to approximately $2500\,nN$. No further increase of the adhesion force is observed if the normal force is increased beyond that value. During this measurement, the adhesion

force values vary very strongly and a large standard deviation can be observed as indicated by error bars of Figure 6-8.

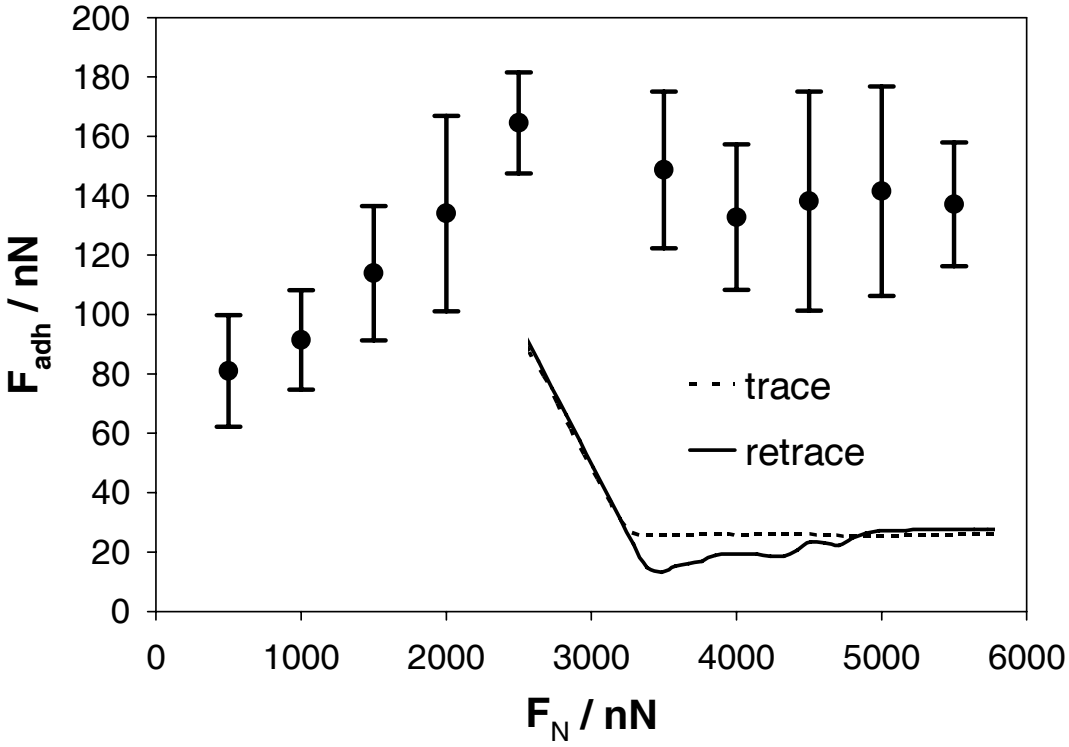

Figure 6-8 Adhesion force between a smooth polystyrene particle and a PVD coated aluminum substrate as a function of the applied normal force measured by AFM. The insert reveals a typical force-distance curve signaling the breakage of multiple contact points.

Two effects contribute most to the increase of the adhesion force in the low normal force range.

Similar as for the adhesion between smooth adhesion partners (see Paragraph 6.1.2.2), the first relevant mechanism is the plastic deformation: between the particle and the asperity the contact area is very small, so that the stress is strongly localized. Hence the influence of the plastic deformation can be even stronger than in the case of smooth adhesion partners.

The second effect is the increasing number of contact points (cf. Paragraph 2.1.3.2). If the particle is on a rough surface with a densest packing of asperities, there is a certain probability that the particle gets into contact with two or more asperities. This effect can be enhanced, if the particle is deformable. The increase of the number of contact points results in a significant increase of the contact area, so that the adhesion force also increases significantly. There is evidence for such multiple contact points obtained from AFM measurements. For example, the retrace curve depicted in the insert of Figure 6-8 apparently shows the breakage of such a contact. The increase of the number of contact points is more important for the increase of the adhesion force between rough adhesion partners along an increasing normal force because this effect

can easily cause the adhesion force to double or triple. This is also the reason for the strong scattering of the adhesion force data. However, because of the spherical shape of the particle, the maximum number of contact points is limited, such as shown in the comparison of particle and substrate profiles of Figure 6-5. Accordingly, the significant increase of the adhesion force stops at a normal force of approximately $2500\,nN$.

In the next two paragraphs these two effects are separately investigated by means of model calculations.

6.2.5 FEM-simulation of the adhesion force between rough adhesion partners

Considering that there is only one single asperity in the middle of the contact region between the particle and the substrate, the system turns out to be axisymmetric. The adhesion force can be predicted with the model described in Section 3.2. Various asperity sizes ranging from $10\,nm$ to $1000\,nm$ are simulated in the FEM-study [64], whereas the applied normal force is maintained in the range of several $100\,nN$ and the Hamaker constant of the system is set to $6.6 \cdot 10^{-20}\,J$. The results obtained are shown in Figure 6-9 and compared with the Rumpf model for the adhesion force between rough, rigid adhesion partners (Paragraph 2.1.3.1).

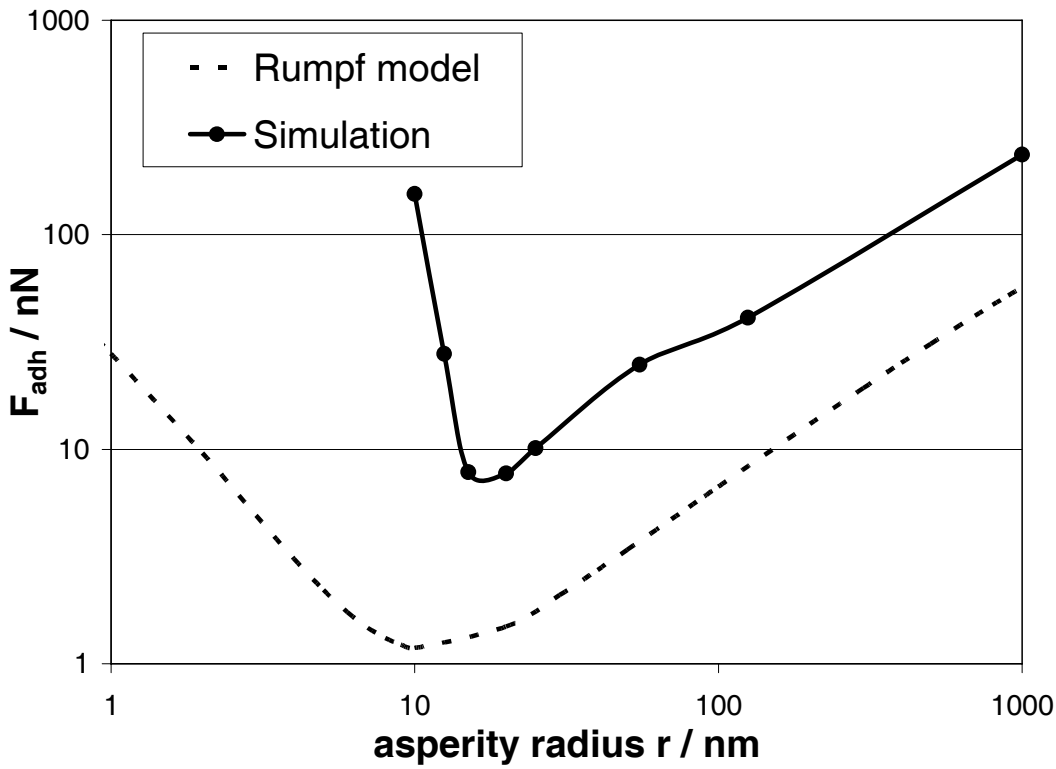

Figure 6-9 Prediction of the adhesion force between a $10\,\mu m$ polystyrene particle and a rough substrate as a function of the asperity radius according to the FEM-simulation and to the Rumpf model.

Because the particle deformation is included in the FEM-model, the simulation usually predicts higher adhesion force values than the Rumpf model. Also the optimal asperity radius, at which the minimum adhesion force is obtained, is larger than predicted by the Rumpf model. In the example depicted in Figure 6-9 the optimal asperity of $r = 10\,nm$ according to Rumpf does not effectively reduce the adhesion force, since the asperity can almost totally penetrate into the polymer particle. The optimum radius lies at the specified condition at approximately $r = 20\,nm$.

6.2.6 Adhesion force distribution between a particle and a monolayer of asperities

In a simplified approach the adhesion force between a particle and a layer of asperities is investigated without considering the particle deformation. The surface is modeled with as a densest packed layer of spherical asperities, such as shown in Figure 6-10 as a top view. The interaction of each asperity with the particle is calculated according to the Hamaker theory (see Paragraph 2.1.1). To simplify the definition of the positions of each asperity the y-axis is set to be in an angle $60°$ to the x-axis. This numerical simulation is done in two steps. In the first step the (x,y)-position of the particle is defined, and the z-position of the particle is reduced, until the minimal distance between the particle and one of the asperities reaches the contact distance of $0.4\,nm$; in the second step the adhesion forces between the particle and each asperity are calculated and summarized to give the total adhesion force at this position. The Nassi-Shneidermann diagram of this calculation is given in Appendix 10.4. Since the surface structure is periodical, the variation of the (x,y)-position of the particle axis within the hatched area is representative. The adhesion force between the particle and the asperities on the rough surface can be derived from the geometry of the surface, which is described by the radius of the asperities r and the positions of the asperity centers (x_n, y_n, z_n), and the radius R and the center (x, y, z) of the particle.

The projections of the centers of the asperity n and the particle on the $x-y$ plane are separated by a distance of:

$$d_n = \sqrt{(x_n - x)^2 + (y_n - y)^2 + (x_n - x)(y_n - y)}. \qquad \text{Eq. 6-4}$$

The contact distance between the center and the asperity is then:

$$a_n = \sqrt{(x_n - x)^2 + (y_n - y)^2 + (x_n - x)(y_n - y) + (z_n - z)^2} - (r + R), \qquad \text{Eq. 6-5}$$

and the angle between the line connecting the both centers and the $x-y$ plane is:

$$\theta_n = \arctan[(z_n - z)/d_n]. \qquad \text{Eq. 6-6}$$

Hence, the adhesion force between the particle and the entire surface is:

$$F_{adh} = \frac{AR}{6(z-R)^2} + \sum_{1}^{n} \frac{A}{6a_n^2} \frac{R \cdot r}{R+r} \sin\theta_n \,. \qquad \text{Eq. 6-7}$$

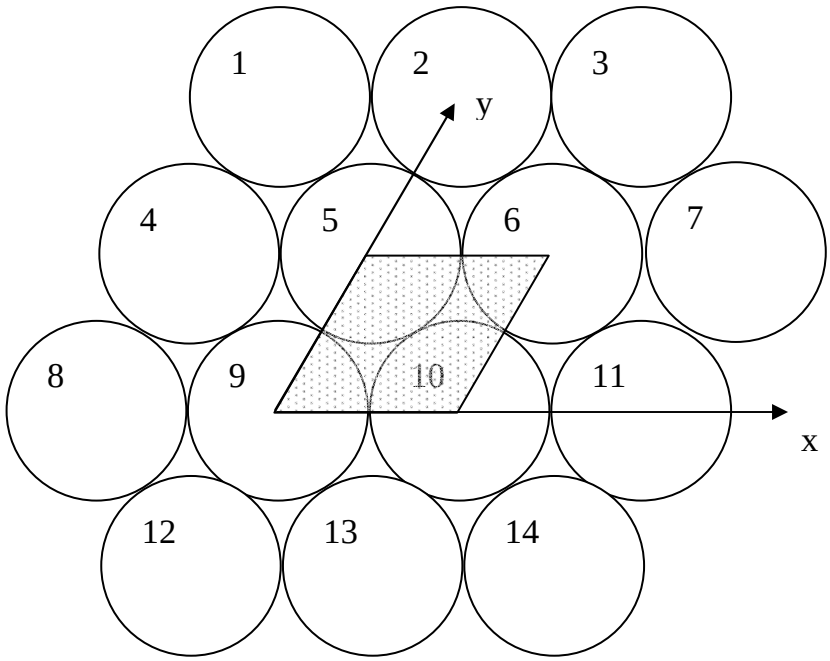

Figure 6-10 Example of a pattern for the simulation of the adhesion force distribution. If the asperity size is small, this pattern has to be enlarged accordingly, to reach a sufficiently high accuracy.

The distributions of the adhesion force are shown in Figure 6-11 for various asperity sizes. The width of the adhesion force distribution appears to increase with increasing asperity radius.

If the asperity size is small, the particle is always in the vicinity of several asperities (distances significantly below $1nm$). Hence, the adhesion force is relatively large and it does not strongly depend on the (x,y)-position of the particle. However, in case of large asperities, a particle may – depending on its (x,y)-position – get in direct contact with one to three asperities. The adhesion forces between the particle and other asperities, which are not in the vicinity of the particle, are negligible. Accordingly, the adhesion force distribution can vary approximately by a factor of 3.

According to Götzinger *et al.* [106], adhesion force distributions between a smooth particle and a rough substrate can be approximately described with Weibull distributions:

$$P(F_{adh}) = 1 - exp\left[-0.693\left(\frac{F_{adh} - F_{adh,min}}{F_{adh,50} - F_{adh,min}}\right)^n\right]. \qquad \text{Eq. 6.8}$$

However, this paper did not discuss the dependence of the index n, it is merely given as a fit parameter of 1.2. In fact, it is a parameter depending on the size of the asperities as well as the size of the particle, not only on the ratio between the both radii. This value can only be calculated from the numerically simulated adhesion force distributions. For the investigated cases shown in Figure 6-11 with a particle of $10\,\mu m$ in diameter, the value of n decreases from 4.2 for asperities with a radius $r = 10\,nm$, to 2.4 for $r = 25\,nm$ and to $n = 0.74$ for $r = 100\,nm$.

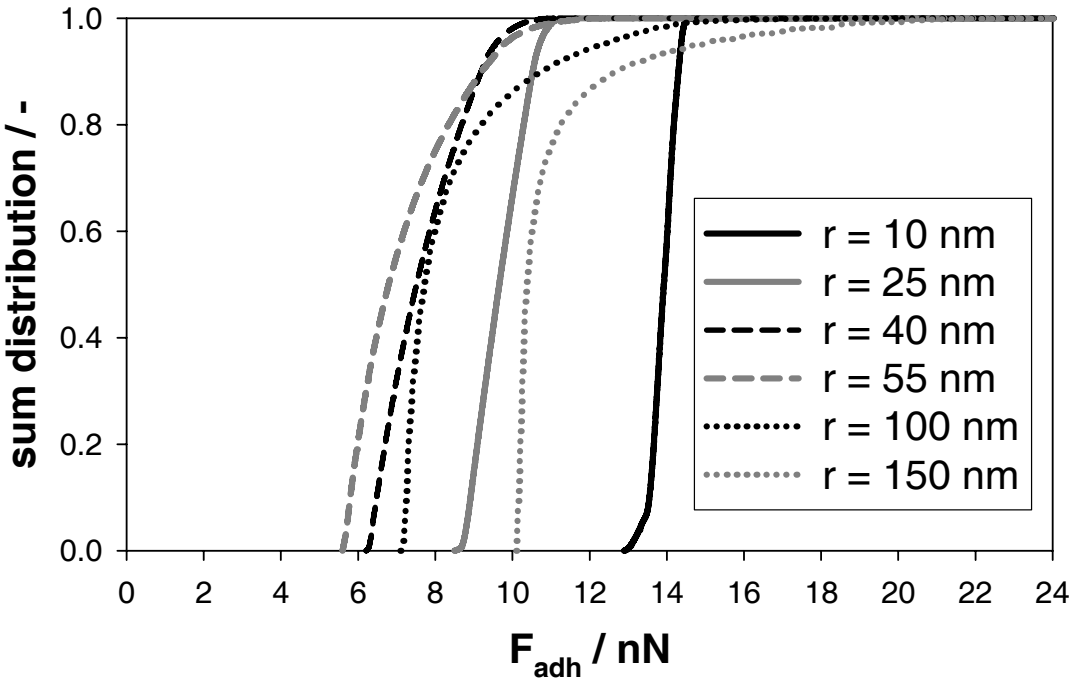

Figure 6-11 Distributions of the adhesion force between a $10\,\mu m$ polystyrene particle and rough substrates characterized by a densest packing of asperities of various radius.

There is an optimal radius of the asperity with respect to minimizing the median value of the adhesion force. For example, in case of a $10\,\mu m$ spherical particle this optimal asperity size is approximately $55\,nm$; this value is significantly larger than predicted by the model of Rumpf (Paragraph 2.1.3.1), wherein only the adhesion force between the particle and a single asperity is considered.

As can be seen in Figure 5-4, real surfaces do usually deviate from a densest packing of asperities. There are always offsets and failures in the structure. However, if the probability for offsets and failures is not too high, *i.e.*, if the asperity layer is by all means not “coarse”, the adhesion force distribution of a spherical particle with such a surface does not deviate a lot from the simulation based on a densest packing of asperities. Actually, the ideal surface with respect to reduce the adhesion force is a “not too coarsely” coated one. In this case, there are enough asperities on the surface, so that the particle cannot reach the vicinity of the uncoated surface, while the distances between the asperities are possibly large so that adhesion between the

particle and the neighboring asperities is minimized. If the surface is coated too coarsely, the adhesion force distribution is always very wide, often bimodal or multimodal. A good example is the adhesion force distribution between a polystyrene particle and a polished aluminum substrate, such as shown in Figure 6-4.

6.2.7 AFM-measurements on substrates with well-defined roughness profiles

In this paragraph the modeling of the adhesion force between rough adhesion partners is validated by AFM-measurements. Since the two aluminum substrates used as model surfaces in Paragraph 6.2.2 do not possess well-defined surface structures, further investigations are carried out between a $10\mu m$ polystyrene particle and dip-coated silicon wafers, each coated with a layer of mono-disperse silica particles of different sizes – $34nm$, $110nm$ and $250nm$. The surface profiles of these substrates are shown in Figure 5-4. The AFM-measurements performed here are carried out in pure nitrogen atmosphere. During the measurement the normal force is always controlled in the range of several $100nN$ and the contact time is approximately $1.5s$. The resulting adhesion force distributions are shown in Figure 6-12.

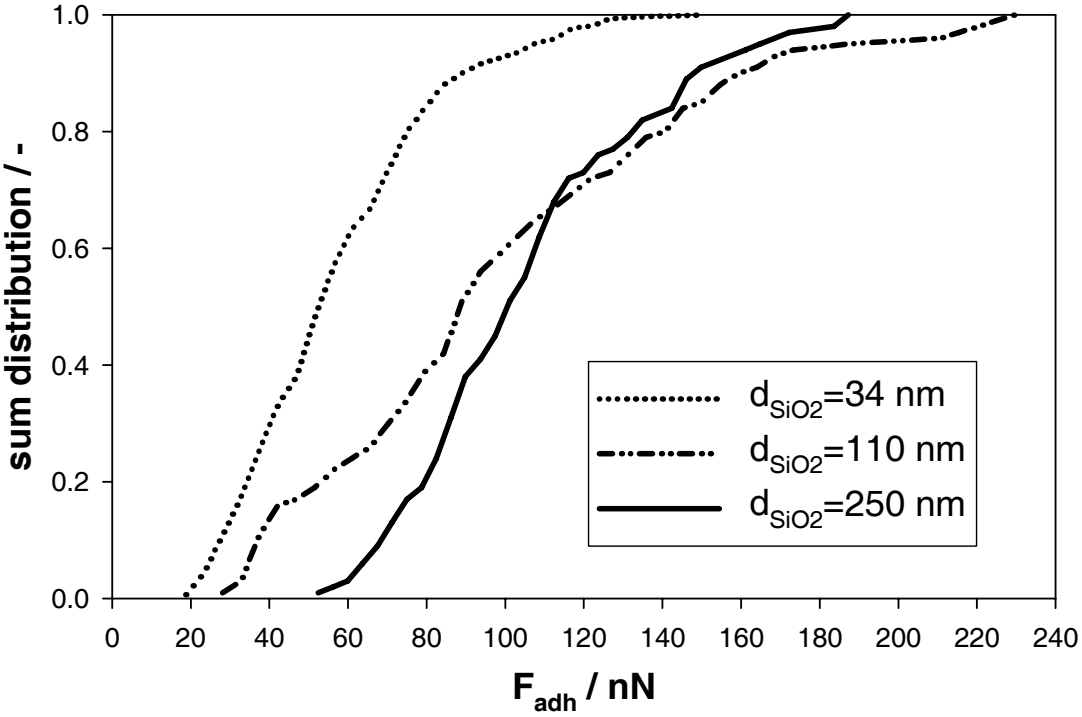

Figure 6-12 Adhesion force distribution of a $10\mu m$ polystyrene particle on substrates coated with silica nano-particles of different sizes.

If comparing the AFM-measurement (Figure 6-12) with the model calculation (Figure 6-11) one will note that the experimentally obtained adhesion force is generally higher and that the corresponding force distributions are wider. This is due to the deformation

of the polystyrene particle. The sum functions of the adhesion force distributions are fitted with Weibull functions (Eq. 2.32). The fitting parameters of the three adhesion force distributions are summarized in Table 6-1.

Table 6-1 Parameters of the adhesion force distributions shown in Figure 6-12 according to Weibull in comparison to the prediction of the FEM-simulation as described in section 6.2.5.

Asperity size on substrate	$F_{adh,FEM}$	$F_{adh,min}$	$F_{adh,50}$	n
$34\,nm$	$8\,nN$	$19\,nN$	$52\,nN$	1.55
$110\,nm$	$25\,nN$	$28\,nN$	$89\,nN$	1.46
$250\,nm$	$42\,nN$	$52\,nN$	$100\,nN$	1.74

It is quite interesting to note that the minimal adhesion forces obtained by means of AFM-measurements $F_{adh,min}$ are always only somewhat larger than the prediction of the FEM-simulation $F_{adh,FEM}$, as shown in Table 6-1. As the FEM simulation only considers the adhesion force of a particle being in contact with one asperity, the interaction of the particle with the neighboring asperities is neglected. Therefore, obtaining this small difference is quite reasonable: it can be concluded that the FEM-simulation provides a proper estimation of the minimal adhesion force between a deformable particle and rigid substrates with regular roughness profiles.

The mean adhesion force of the $10\,\mu m$ polystyrene particle on the $110\,nm$ substrate is of the same order as the mean force on the $250\,nm$ substrate, while the distribution is wider. It is reasonable that for a single contact between the polystyrene particle and the $110\,nm$ silica particle on the substrate the adhesion force is smaller than the adhesion force of the same particle with a $250\,nm$ silica particle. Nevertheless, because the peak-to-peak distance between the asperities is smaller, the probability that the polystyrene particle gets into contact with several asperities of the $110\,nm$ substrate is higher than for the $250\,nm$ substrate.

If the surface coating is a monolayer (see Figure 6-11), it may be expected that the median value of the adhesion force distribution between the polystyrene particle and the $34\,nm$ substrate is larger than for the same particle and the $110\,nm$ substrate, However, as can be seen in Figure 5-4, right, the $34\,nm$ coating has a 3-dimensional structure. Upon approaching the substrate surface the probability that the particle gets in touch with an outstretched asperity is high (Figure 6-13). Since the van der Waals force is reversely proportional to the squared particle-asperity distance, the adhesion forces between this particle and the asperities near the outstretching one are smaller than predicted by the model. Hence, the total adhesion force is also smaller.

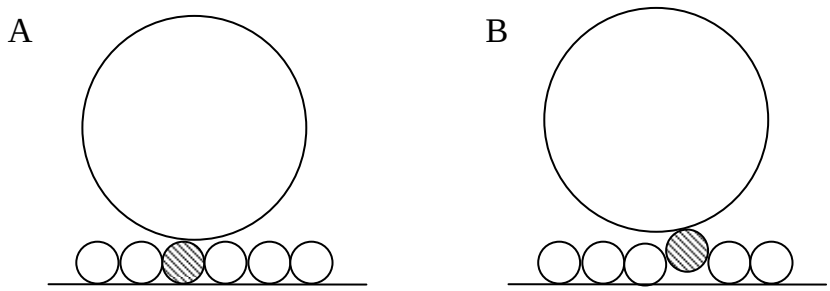

Figure 6-13 A: a particle on a regular monolayer of asperities. B: a particle on a monolayer of asperities with one outstretching asperity. The hatched asperity is in contact. In the case B the distance of the particle to the other asperities is larger than in the case A.

6.2.8 AFM-Measurements with the toner particles

Toner particles are also rough. The effects observed between the rough adhesion partners (*e.g.*, reduction of the adhesion force, dependence of the adhesion force on various parameters) can all be found upon measuring the toner particles. As shown in Figure 6-14, the adhesion force between a toner particle and a smooth silicon wafer $\overline{F}_{adh} = 75\,nN$ is significantly smaller than the prediction of $240\,nN$ according to the Hamaker model (Eq. 2.4) for the adhesion force between smooth adhesion partners. Due to the high homogeneity of the wafer surface, the adhesion force distribution is very narrow. On the polished aluminum substrate a multimodal adhesion force can be characterized, as discussed in Section 6.2.6. On the randomly rough PVD-coated surface the adhesion force shows a Weibull distribution (Eq. 2-32, Paragraph 2.1.3.1), with the parameters: $F_{adh,\min} = 5.87\,nN$, $F_{adh,50} = 21.18\,nN$ and $n = 1.14$.

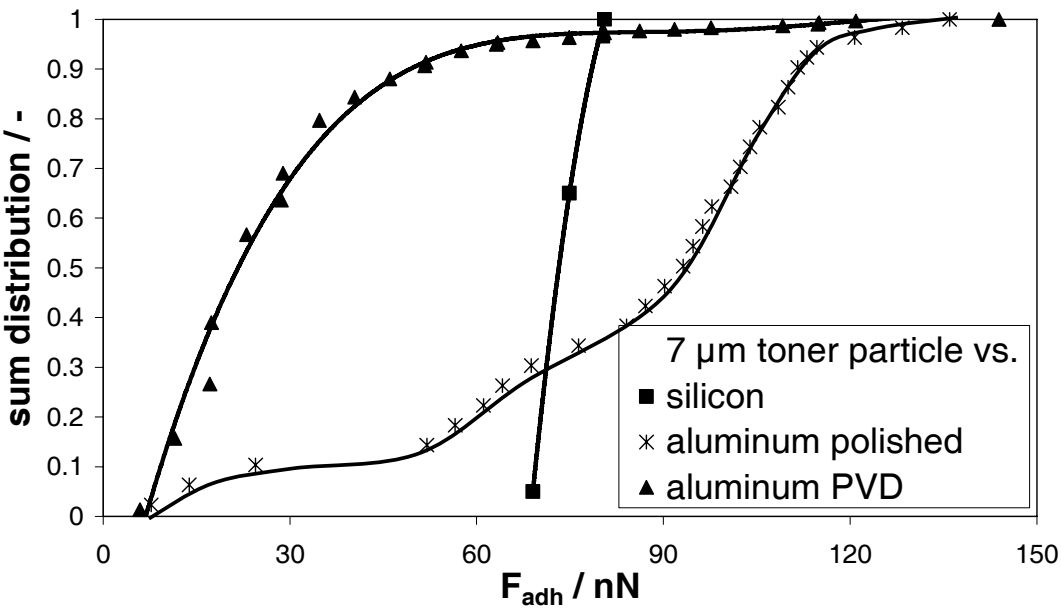

Figure 6-14 Adhesion force distribution of a $7\,\mu m$ toner particle on various substrates: silicon wafer, polished aluminum substrate as well as the PVD-coated aluminum substrate.

As toner particles have complex compounds and not a well-defined surface structure, the adhesion force depends on the individuality of each particle and each contact position. It is therefore necessary to treat the adhesion force between toner particles and different surfaces as a stochastic phenomenon. As a consequence, several particles have to be examined and several measurements should be carried out on each particle.

Figure 6-15 shows the adhesion force distributions between 6 toner particles of two different types (magenta, without CCA and magenta, with CCA, surface is covered with $16\,nm$ silica nano-particles to approximately 30%) and OPC surfaces measured with AFM. These measurements are also carried out on different positions of the OPC surface. To avoid any influence of moisture, the measuring cell is continuously flushed with pure nitrogen. The normal force is set to approximately $300\,nN$ during all the measurements and the contact time is around $1\,s$. While most of the curves are generally comparable and have the same trends as for the model system, there are always some curves, which appear to significantly differ from the others (*e.g.*, the curve "Magenta, with CCA, No. 2" of Figure 6-15).

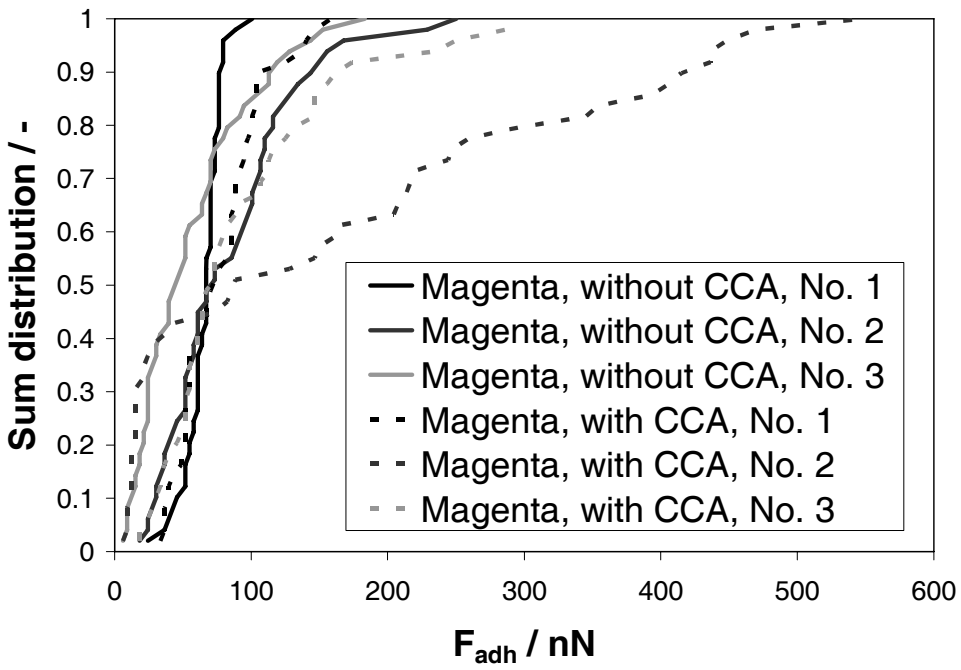

Figure 6-15 Adhesion force distributions between 6 different toner particles of two different types and OPC surface.

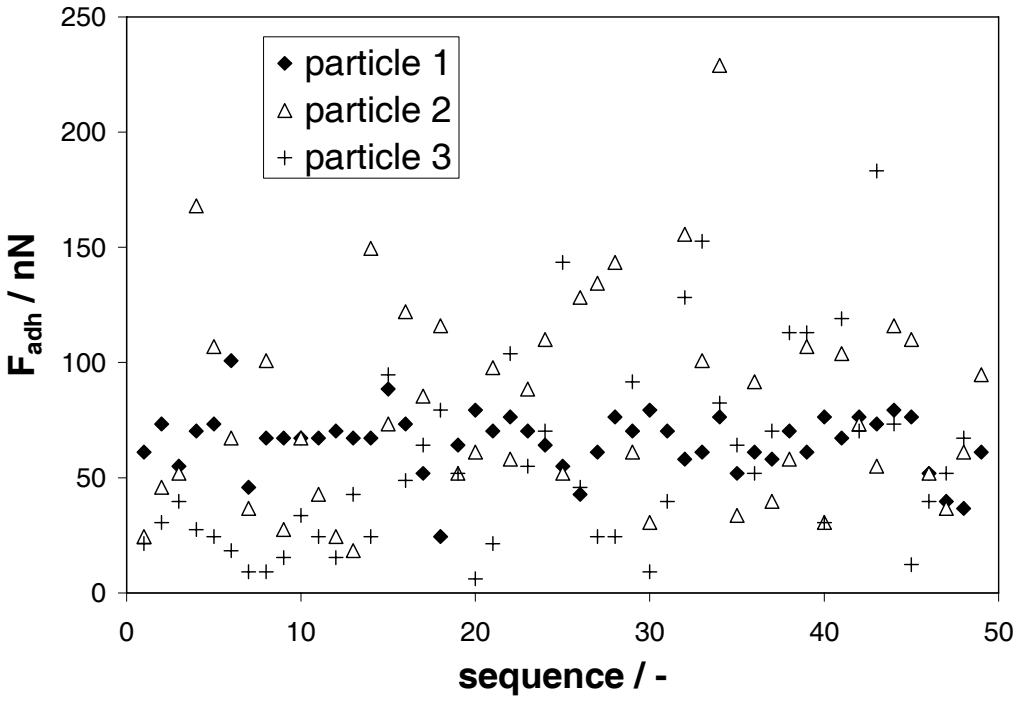

Figure 6-16 Adhesion force between 3 toner particles (magenta, without CCA) and OPC surface in dependence of the measuring sequence.

Figure 6-16 shows the adhesion forces of the 3 magenta particles without CCA as a function of the measuring sequence. It is observed that at the beginning of each measuring sequence the adhesion force is usually quite small, later the spectrum of the adhesion force gets wider. There is also SEM evidence (Figure 6-17), which shows that the surface of the toner particle is significantly deformed during AFM-measurements. This deformation results in the loss of surface roughness. The same effect is also observed in the laser printing process. When the toner is agitated too long together with the carrier particles in the development station, the silica nano-particles turn out to be almost totally pressed into the toner particle, as shown in Figure 6-18.

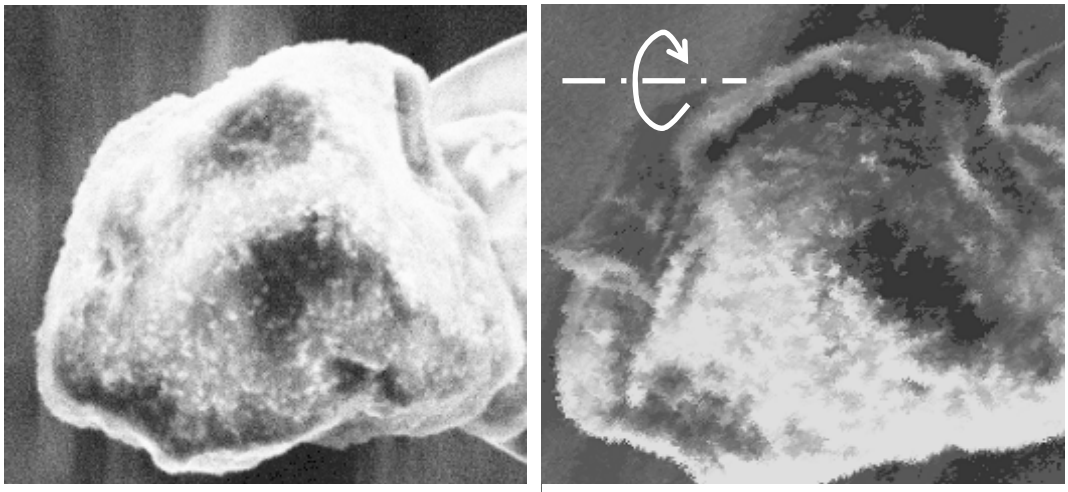

A. Before contact | B. After 10 contacts, $F_N \approx 50\,nN$

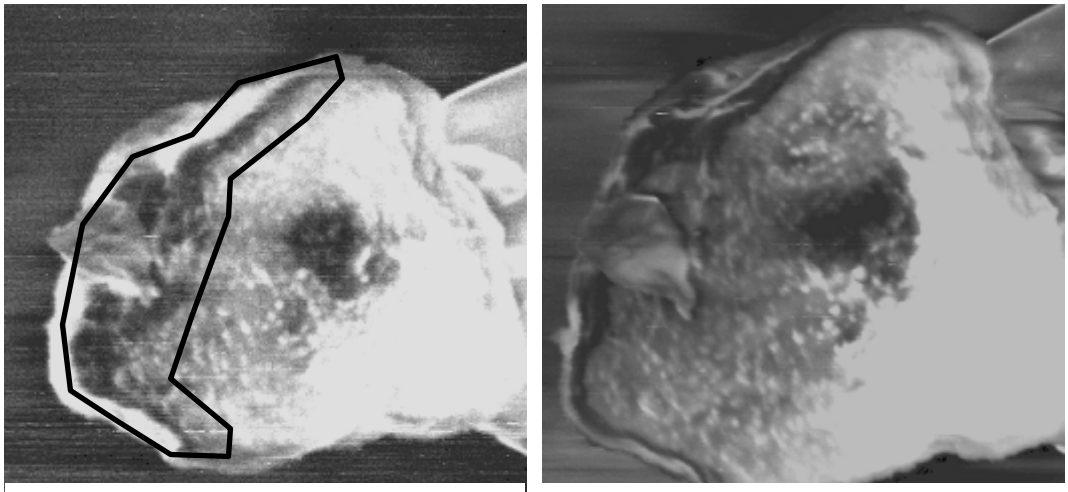

C. After 20 contacts, $F_N \approx 50\,nN$ D. After 70 contacts, $F_{N,max} \approx 350\,nN$

Figure 6-17 SEM-pictures show the deformation of a toner particle along the AFM-measurement. A: freshly prepared particle on the AFM-cantilever; B: after 10 force-distance measurements the particle is relocated. The rotation of the particle is indicated by the arrow in the picture, deformation is not yet significant; C: after 20 measurements first evidences of the deformation can be observed on the particle; and D: the particle is considerably distorted.

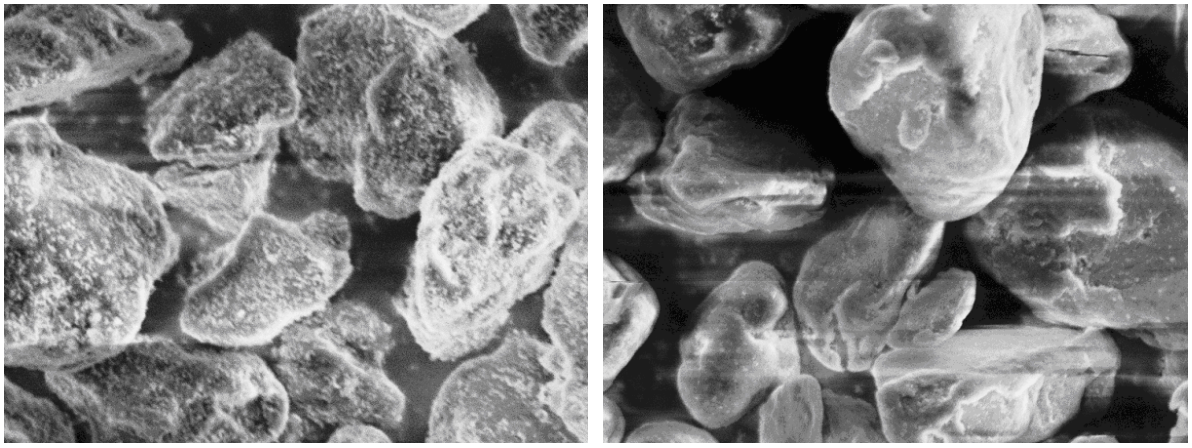

Figure 6-18 Aging of the toner particle in the development process. The silica nano-particles on the toner surface are pressed into the toner particle due to impacting and friction. Left: freshly prepared toner probe; right: the same charge of toner particles after agitated for $30\,min$ in the development station.

6.2.9 Centrifugal detachment measurement of toner particles

For the measurement of the adhesion force between the toner particles and the substrates the centrifugal detachment measurement provides obvious advantages in comparison to the AFM-method. It measures the adhesion force of many toner particles during one experiment, while every particle is only measured once.

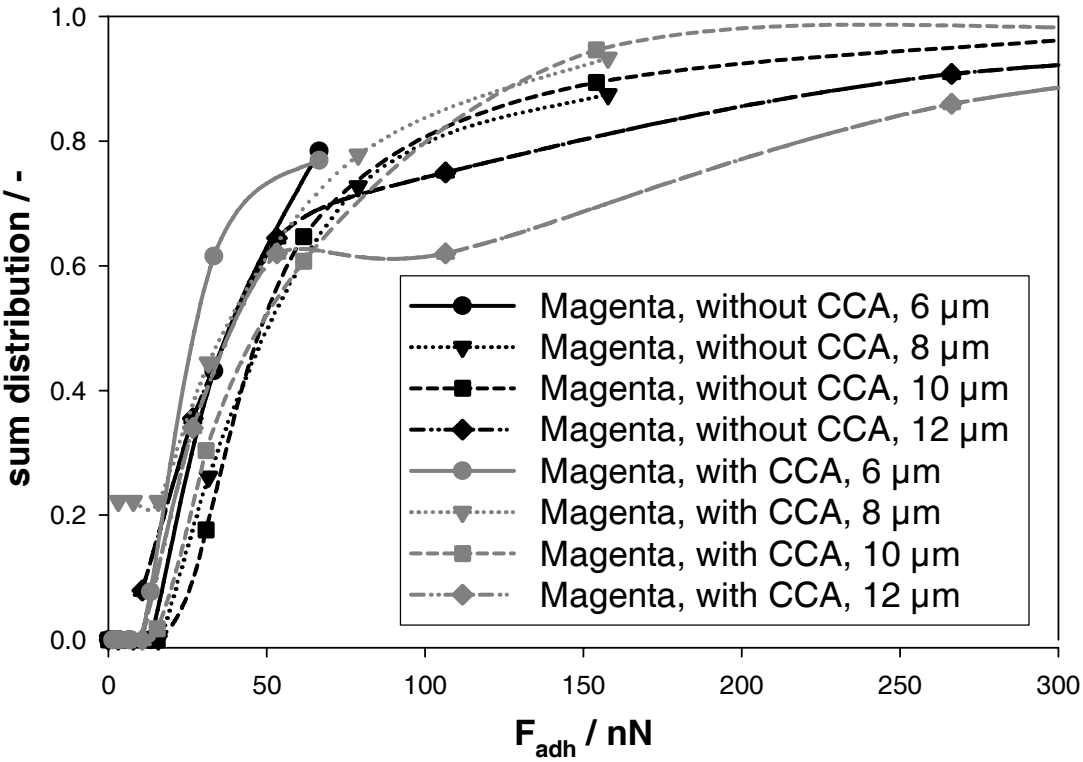

Figure 6-19 Adhesion force distribution of toner particles of various size fractions with OPC surface measured with the centrifugal detachment method.

As described in Paragraph 4.3.2.1 the toner particles are dispersed on the OPC surface through deposition, so that they are brought into contact with negligible normal forces. Figure 6-19 shows the adhesion force distributions between the magenta toner particles with and without CCA (surface covered with $16\,nm$ silica nano-particle with a surface coverage of approximately 30%) and OPC surface. Here, the median values of the adhesion force distributions are smaller, in comparison to when performing AFM-measurements of the same adhesion partners (see Figure 6-15), while the width of the distribution remains comparable. The larger median values of the adhesion force measured in the AFM-measurement may be due to the influence of the normal force during the measurement.

Since the adhesion force distribution only slightly depends on the particle size, it is possible to approximately describe it with a single log-normal function. Table 6-2 shows the parameters of the adhesion force distribution of the toner fraction $6 \sim 12\,\mu m$ on OPC surface. For most of toner types investigated in this work at least 70% of the toner particles follow this fraction.

Table 6-2 Parameters of the log-normal adhesion force distributions between toner particles and an OPC surface as shown in Figure 6-19.

Toner sort	Expected value μ	Variance σ^2
Magenta, without CCA	$57\,nN$	$2496\,nN^2$
Magenta, with CCA	$79\,nN$	$18458\,nN^2$

This mathematic description simplifies the comparison between the different measurements. In the electrophotographic process for example, small μ and small σ^2-values (hence narrow distribution) are always favorable.

6.2.9.1 Relocation effect in the centrifugal detachment measurement

The influence of the normal force is investigated in the centrifugal detachment measurement with the method described in Paragraph 4.3.2.2.

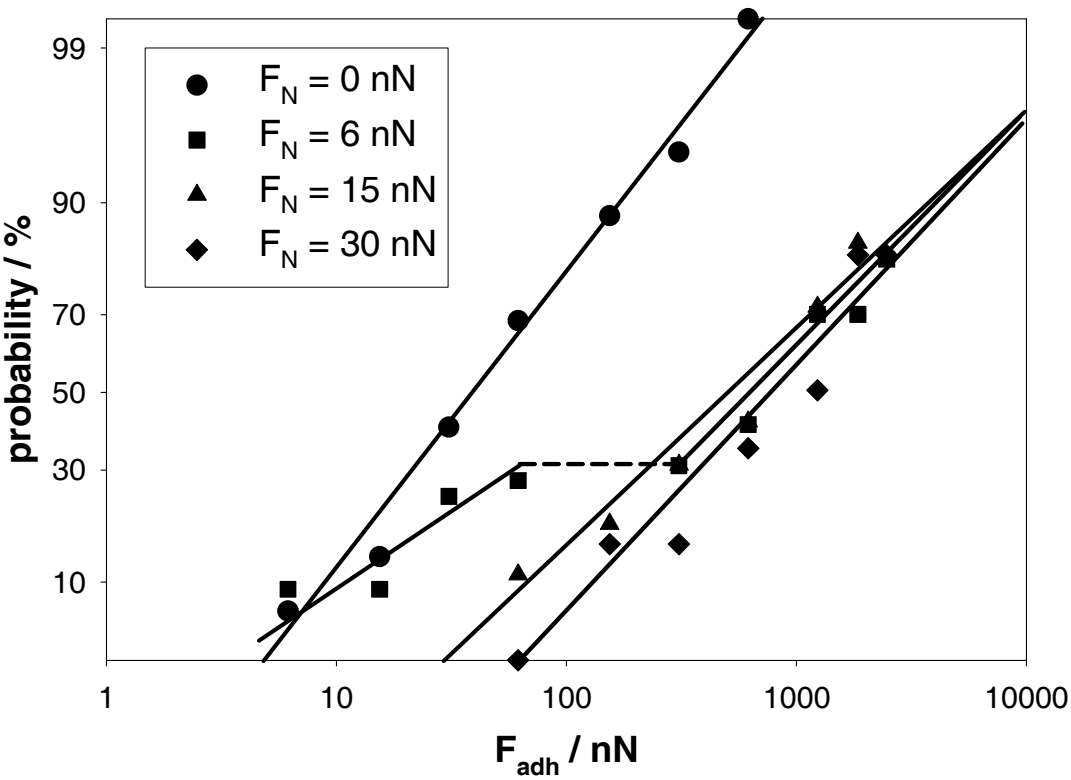

Figure 6-20 Adhesion force distributions between the fraction of $10\,\mu m$ black toner particles (surface covered with $16\,nm$ silica nano-particle with a surface coverage of approximately 30%) with silicon wafer under the influence of the normal force. The distributions are shown in a probability plot. In this plot the sum function of a log-normal distribution is a straight line.

The influence of the normal force on the adhesion force distribution between toner particles and silicon wafer is shown in Figure 6-20. Although the applied normal force is tiny, it has a large influence on the adhesion force. The whole adhesion force shifts approximately one order of magnitude to the right, *i.e.*, to higher values. This large influence is due to the relocation of the particle into a stable position (see Paragraph 2.1.3.1) which is followed by the deformation of the contact positions (see Paragraph 2.1.3.2). This effect can always take place, if the particle is not fixed, as in the case of centrifugal detachment measurements or in the most industrial processes. Rumpf [17] also observed this increase in his centrifugal detachment measurements. This effect has to be taken into consideration in order to optimize the behavior of the toner particles in the electrophotographic process.

6.2.9.2 Influence of the silica coating on the particles

Toner particles with different silica nano-particle coatings are investigated to study the influence of the nano-particle size and the surface coverage on the adhesion force in the centrifugal detachment measurement. The size of the silica nano-particles varies from approximately $12\,nm$ to $400\,nm$ and the surface coverage varies from 10% to 90% (produced by KAO, Japan). The specifications of the different probes are listed in Table 6-3.

Table 6-3 Specification of the silica coatings of the modified toner sorts measured in this work

Short name	Silica size	coverage	Short name	Silica size	coverage
T_12nm_10	$12\,nm$	10%	T_40nm_70	$40\,nm$	70%
T_40nm_10	$40\,nm$	10%	T_40nm_90	$40\,nm$	90%
T_40nm_30	$40\,nm$	30%	T_400nm_10	$400\,nm$	10%

At first the influence of the silica nano-particle size is investigated. The toner probes each with a surface coverage of 10% of silica nano-particles are tested against a silicon wafer. During the measurements no normal force is applied. The results are shown in Figure 6-21. Although the sizes of the silica nano-particles are quite different from each other, the adhesion force between the particles and the silicon wafer seems to be comparable, with the Weibull-parameters $F_{adh,50}$ in the range of $150 \sim 200\,nN$ and $n \approx 1$. This result appears to be unexpected at a first glance: in case of rough substrate surfaces a strong influence of the asperity size can be observed (see Paragraph 6.2.7). The reason for only minor differences as observed here between the toner particles with different silica coatings is that the surface coverage is no more than 10%. As the particles fall on their proper surface with a certain position, there is only a relatively low probability that a silica nano-particle happens to be there. Most

likely, the particle directly gets into touch with the wafer surface and accordingly the adhesion force is larger than which between toner particle with 30% surface coverage of silica nano-particle and silicon wafer (Figure 6-20) under the same condition. If there is a silica particle at the contact position, – even though the theoretical adhesion force is $1nN$ for a $12nm$ silica nano-particle acting as spacer to the silicon wafer and $27nN$ for a $400nm$ silica particle – this makes little difference, as these forces only refer to the first 10% or 20% of the adhesion force distribution. The more the surface is covered with silica nano-particles, the less is the probability that the particle comes into contact with the wafer surface. That is also why the adhesion forces measured in this measurement are generally higher than measured for the magenta toner probes (Figure 6-19), where the surface coverage is approximately 30%.

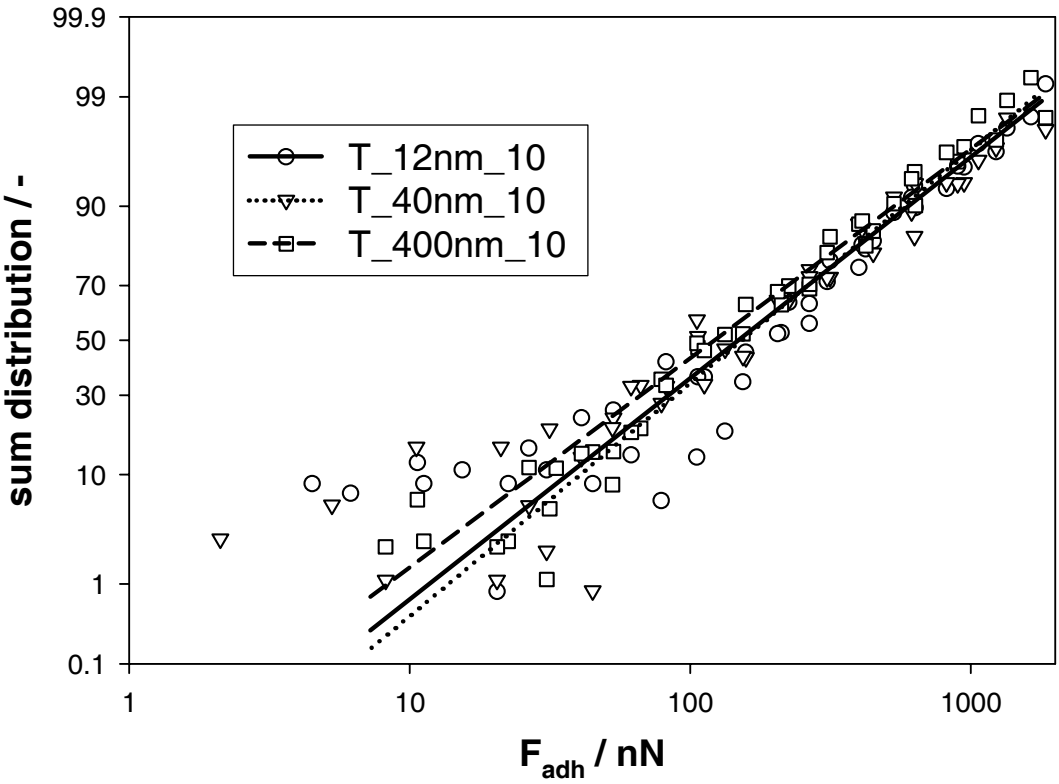

Figure 6-21 Adhesion force distributions between toner particles with different dimensions of the silica coating and the silicon wafer. The symbols indicate measured values of adhesion force distributions of various fractions from $6\mu m$ to $12\mu m$. The data points of each toner probe are fitted with a Weibull function.

In the following, the influences of the surface coverage and the normal force are investigated. Toner particles coated with different amount of $40nm$ silica nano-particles are tested in this experiment. The surface coverage ranges from 10% to 90%. In Figure 6-22 the $F_{adh,50}$ and the $F_{adh,90}$-values of the toner fraction of $6 \sim 12\mu m$ are shown as functions of the surface coverage and the normal force. Since the normal force is applied to the particles through centrifuging, this load is expressed

in the diagram in terms of n-fold of the acceleration of gravity. In case of a $6\,\mu m$ toner particle $5000\,g$ corresponds to a normal (centrifugal) force of $7\,nN$ and in case of a $12\,\mu m$ particle this force is accordingly $53\,nN$.

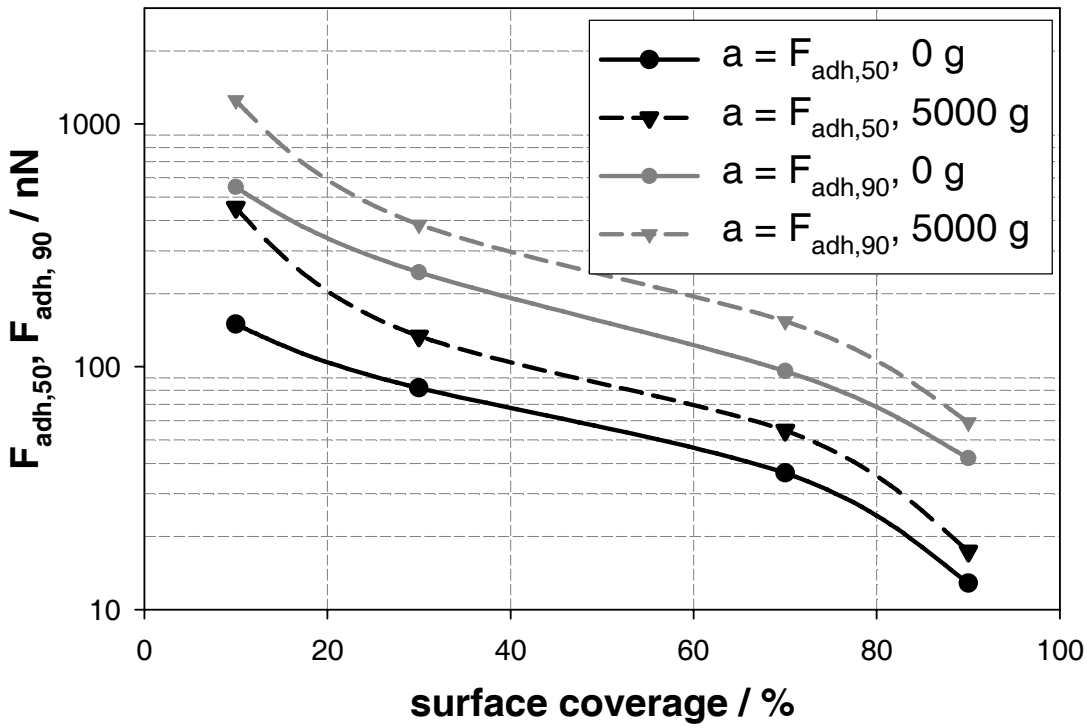

Figure 6-22 Adhesion force between toner particles and silicon wafer in dependence of the applied normal force and the surface coverage of a $40\,nm$ silica coating.

If no normal force is applied, the $F_{adh,50}$-value reduces by a factor of 10, as the surface coverage increases from 10% to 90%. Quite impressive is the behavior if a normal force is applied. If the surface coverage is only 10%, the $F_{adh,50}$-value increases from $150\,nN$ to $453\,nN$, when the particles are pressed to the wafer surface with a tiny normal force. This increase can be even stronger, if the silica size is smaller, as shown in Figure 6-20 for the example of black toner with a $16\,nm$ silica coating. The small silica nano-particles are even easier to “overcome” during relocation.

Increasing the surface coverage of the $40\,nm$ silica coating from 10% to 30% already results in a significant reduction of the $F_{adh,50}$-value. At a coverage of 90% the normal force rarely causes an increase of the $F_{adh,50}$-value of less than 50%, from $13\,nN$ to $18\,nN$.

This measurement indicates that – if the particle surface is well covered with asperities, so that relocation of the particle does not cause a direct contact of the particle with the surface – the drastic increase of the adhesion force due to the relocation effect can be avoided.

6.3 Adhesion force in humid ambience

In a humid atmosphere water vapor can condense on the particle and on the substrate surface. Capillary condensation then leads to a meniscus in the contact region. Two opposite effects of the condensed water with respect to the adhesion force can be observed: The first is a decrease of the Hamaker constant, which is due to the formation of the water layer on the surfaces. The generated meniscus has to be broken in order to separate the adhesion partners, thus an additional meniscus force is needed, as described in Section 2.3. In this section the influence of the meniscus on the adhesion force is experimentally investigated.

6.3.1 Adhesion force between silica particle and mica surface

The adhesion force between a $10\mu m$ sintered silica particle and mica surfaces is investigated by means of AFM-measurements. To avoid any influence of the adsorbed water layer on the force measurement the particle is mounted to the cantilever and heated to $800°C$ prior to the measurement. At this temperature the particle is sintered to the cantilever (melting temperature of silica at $1bar$ is about $1400K$, usually sintering of micron-sized particles starts to become relevant at temperatures of about 70% to 80% of melting temperature). The cantilever is transported to the AFM in a pure nitrogen atmosphere. In the meanwhile the mica substrate is freshly cleaved to assure that the both surfaces are essentially water-free. The measurement is started in a pure nitrogen atmosphere. As shown in Figure 6-23, the relative humidity in the measuring cell upon carrying out the AFM-measurement between the silica particle and the mica surface is gradually raised from 0 to 80% by partially moistening of the nitrogen flow. The adhesion force is in fact a function of the relative humidity. However, stationary conditions are not immediately attained. For example, if the relative humidity increases from zero to 10% the adhesion force reduces gradually from approximately $1200nN$ to $600nN$ within 20 minutes prior to arriving at a constant level. If the relative humidity is further increased, it always takes some time to attain the new equilibrium value of the relative humidity.

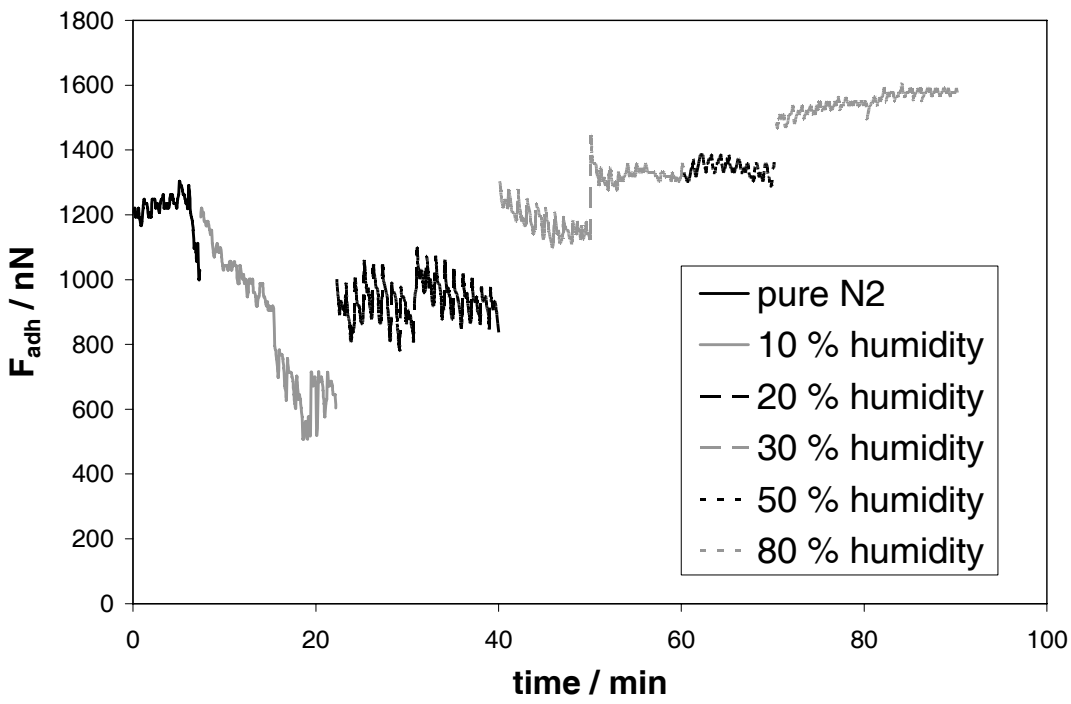

Figure 6-23 Adhesion force between a flame synthesized silica particle and a mica surface in a carefully controlled humid environment. The humidity level in the measuring cell is increased step wise.

The correlation obtained was described in detail by Götzinger [72], who characterized four domains in the whole humidity range:

(1) If a small amount of water molecules is adsorbed on a surface with a relatively high Hamaker constant and if the water molecules are strongly bound and thus not mobile, then the Hamaker constant and the adhesion force decreases. The actual value of the Hamaker constant in humidity depends on the thickness of the water layer, which is related to the relative humidity.

(2) If the humidity continues to increase, the system shifts towards the second domain, where the thickness of the adsorbate layer increases gradually to $0.25 \pm 0.05\,nm$. This layer remains strongly bound on the surface, it can be observed as ice (solid) [107]. The van der Waals force remains small as there is still no meniscus during this regime.

(3) In the third domain the mobility of the water layer further increases so that a meniscus can be formed giving raise to the meniscus force. An increase of the total adhesion force can be observed. According to the Laplace model the meniscus force is almost a constant value within the whole relative humidity range, provided that the meniscus geometry can be described by the Kelvin equation. However, the Kelvin equation is based on the continuum mechanical consideration, which reaches its limit for the prediction of the meniscus geometry in sub-nanometer range between the adhesion partners. It is reasonable, that at low relative humidity the meniscus only built locally at smaller asperities. This is shown in a Monte Carlo simulation of Jang *et*

al. [108, 109]. If the relative humidity increases the small menisci gradually grow to a meniscus covering the whole contact region between particle and substrate. This results in a slow but constant increase of the meniscus force along the increase of the relative humidity. The capillary force may be further increased by an increase of the high viscosity of the water in the vicinity of the particle and the substrate surface, the viscous force (see Paragraph 0) has a significant contribution to the adhesion.

(4) Finally, if the humidity is very high, the thickness of the condensed water may increase to $d \geq 10\,nm$, and the interaction between the water molecules and the substrate surface becomes weak. Measurements of Brunner *et al.* [110] show that the viscosity of the water layer reduces gradually to the bulk value. The viscous force decreases and becomes negligible.

The thresholds between the domains depend on the material properties, especially on the properties of the interacting surfaces (*e.g.*, hydrophilicity or hydrophobicity, surface contamination) [107, 111]. In some cases, not all of these four domains can be observed during the experiment.

Since the amount of water molecules in the contact region approaches asymptotically the equilibrium value, a hysteresis can be observed during increasing and during decreasing the relative humidity. As shown in Figure 6-24, during decreasing a peak of the adhesion force in the humidity range of approximately 50% – which is characterized by a high viscous force – cannot be observed. The adhesion force reduces monotonously with the relative humidity.

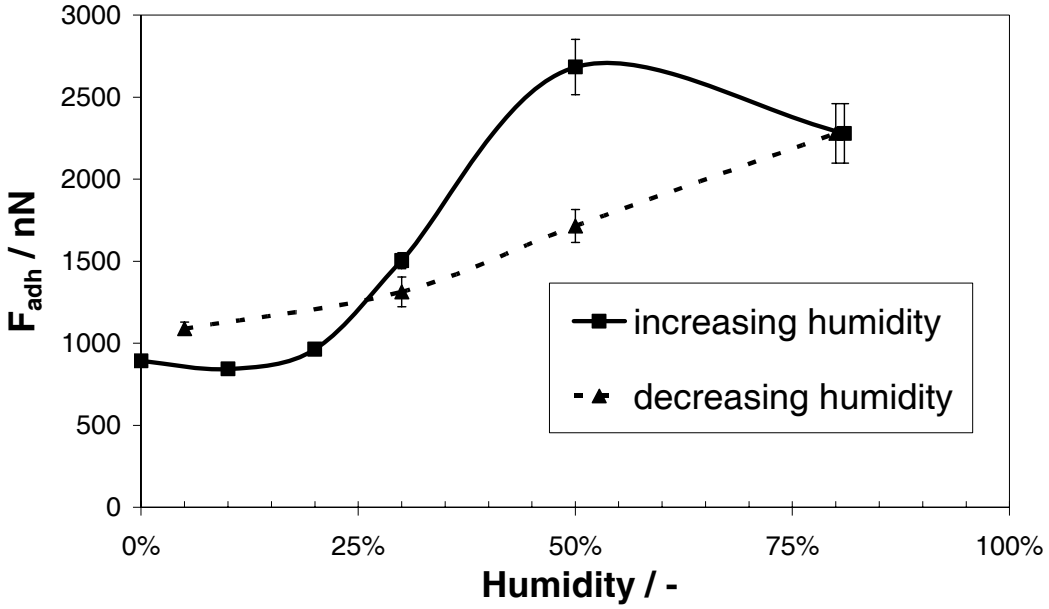

Figure 6-24 Adhesion force between a flame synthesized silica particle and a mica surface in a carefully controlled humid environment. At first, the humidity level in the measuring cell is increased, and then decreased step wise.

6.3.2 Adhesion force between polystyrene particle and silicon wafer

This hysteresis can also be observed during measurements between polystyrene particles and silicon wafer (Figure 6-25). However, the surfaces of the polystyrene particles are not completely water-free, while the surface of the silica particle does not contain any water after heating the particle in the oven, so that the first domain during which the adhesion force reduction takes places cannot be observed. The adhesion force is relatively small in the low humidity range. Since the polystyrene particle surface is not water-free and the difference between the Hamaker constants of polystyrene ($6.6 \cdot 10^{-20}\ J/m^2$) and water ($3.7 \cdot 10^{-20}\ J/m^2$) is not very large, the drop of the van der Waals force because of adsorption of water is not observed. However, the other 3 domains described by Götzinger can all be identified during the measurements. The maximal increase of the adhesion force due to the raise of the meniscus force is approximately $1000\,nN$. This meniscus force is significantly smaller than the prediction of the Laplace model (Eq. 2.49), which should be circa $2000\,nN$ for the system polystyrene-water with a contact angle of $65°$. The relatively large difference between the two measurements shown in Figure 6-25 is still not well understood.

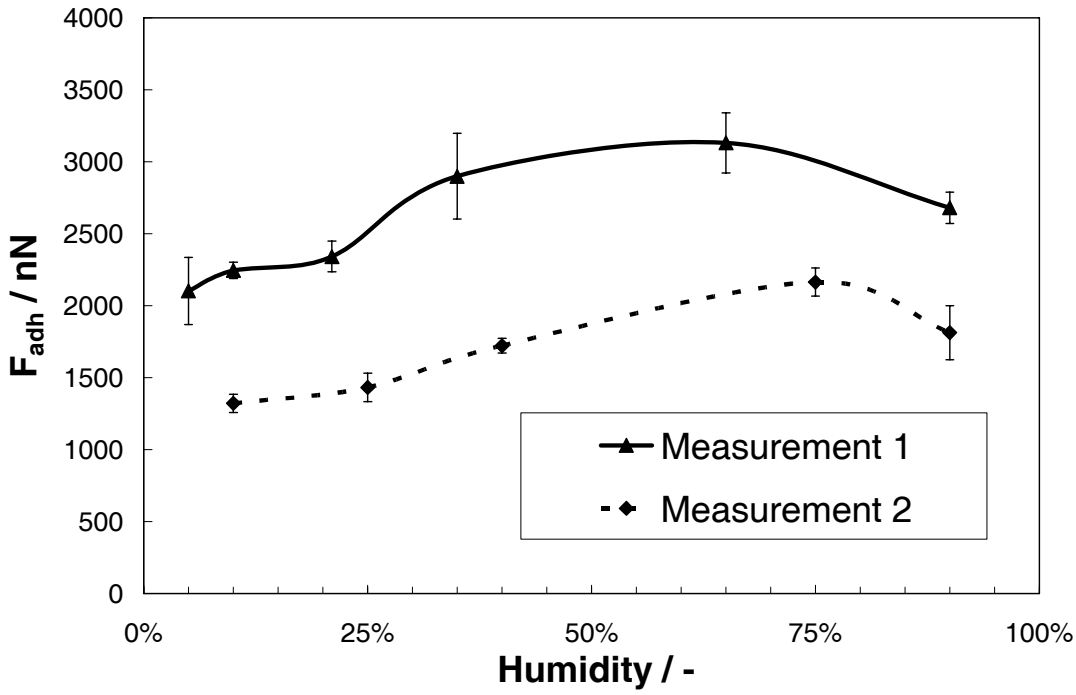

Figure 6-25 Adhesion force between a polystyrene particle and a silicon wafer as measured in a measuring cell as a function of the increasing relative humidity.

It is interesting to observe the influence of the contact time on the adhesion force between smooth adhesion partners in a humid ambience (Figure 6-26). The measurement was carried out in a relative humidity range between 5% and 90%. At each relative humidity level the contact time is increased from $5s$ to $10s$ and then to $15s$.

At low relative humidity values the adhesion force is larger for longer contact time. However, this order changes for high humidity values. This indicates that the meniscus formation and the related effect on the adhesion force constitute a time-dependent phenomenon. If the adhesion partners are not in contact, there is a certain amount of adsorbed water on the surfaces. This amount depends on the properties of the surfaces as well as on the humidity within the measuring cell. If the particle and the substrate get in contact, capillary condensation occurs. This process does not happen immediately, but takes some time to reach an equilibrium, *i.e.*, it takes time for the meniscus to completely form. Longer contact times therefore lead to higher adhesion forces. At high humidity values, the adsorbed layer is already relatively thick, while the adhesion partners are not yet in contact. The meniscus is built almost immediately, when the adhesion partners get into contact. However, if the contact time is long, more and more water molecules condense to reach an equilibrium, which is characterized by a rather thick meniscus. The related system then refers to the domain (4) in Paragraph 6.3.1, where the adhesion force reduces again.

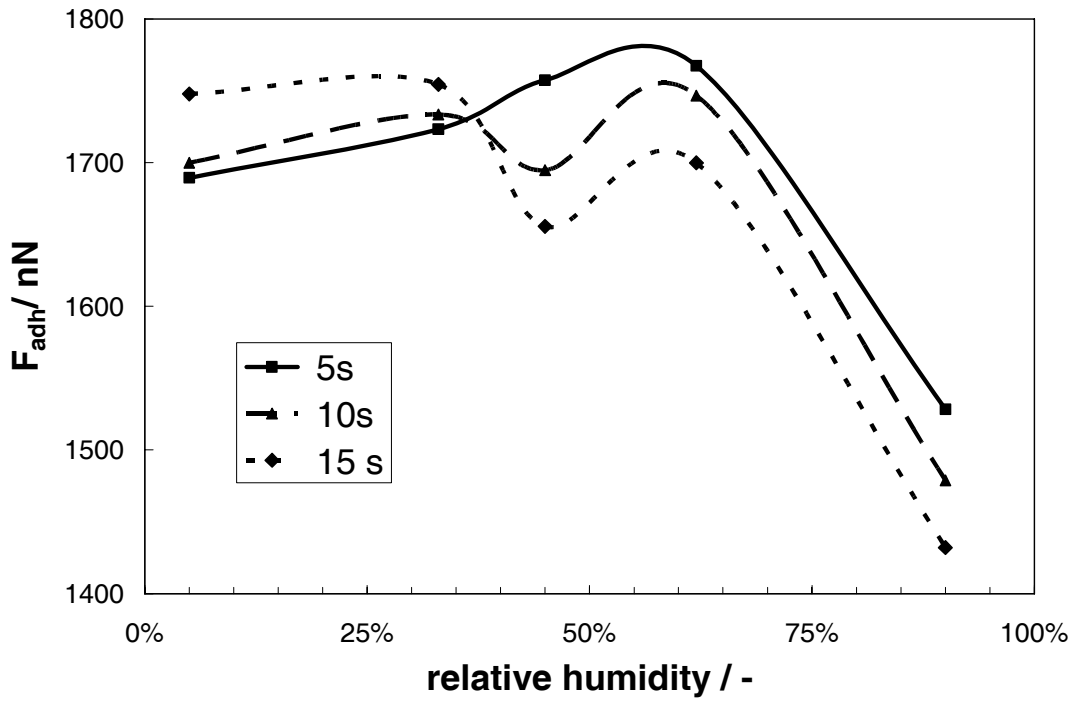

Figure 6-26 Adhesion forces between a polystyrene particle and a flat silicon wafer substrate as a function of the increasing relative humidity.

6.3.3 Adhesion force between rough adhesion partners

Measurements between rough surfaces show a significantly different tendency. The influence of the relative humidity is not significant for measurements between the rough adhesion partners within a large humidity range (Figure 6-27). The slight variation of the median value of the adhesion force measured at different relative humidity level is more due to the strong scattering of the recorded adhesion force data than due to the influence of the meniscus force.

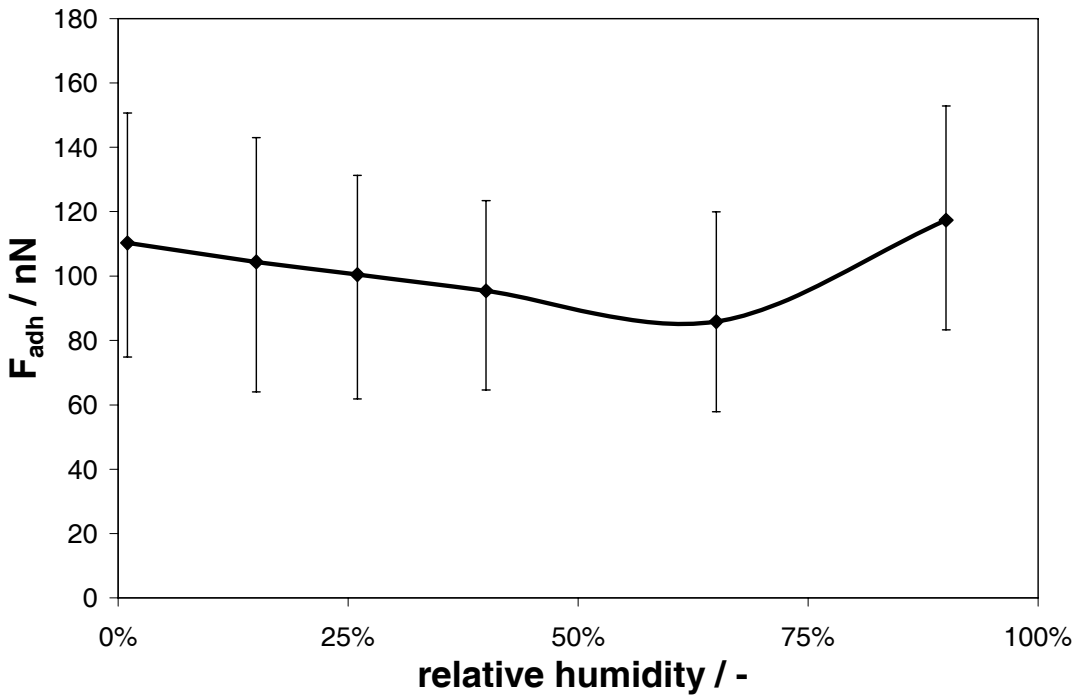

Figure 6-27 Adhesion force between a silica particle and a substrate coated with $34\,nm$ silica nano-particles as a function of the increasing relative humidity.

If the meniscus is not thicker than the radius of the asperity, *i.e.*, $17\,nm$ as for the probe exemplary studied here, the geometry of the meniscus can be described according to the sketch of Figure 2-11, left. The meniscus force may then be calculated with Eq. 2.55, which leads to a value of $15\,nN$. This value is one order of magnitude smaller than the van der Waals force. It can thus be concluded that the meniscus force does not play a determining role in the electrophotographic process, provided that the relative humidity is low and that the silica particles located on the toner surface are within the proper size range. Podczeck *et al.* [112] came to the similar results in the range of low relative humidity up to 55%, however, in the high humidity range they observed a significant increase of the adhesion force, which may follow the model described in Figure 2-11, right. Unfortunately, they did not give the size of the asperities on the particles.

6.4 Forces on the charged particles

In the electrophotographic process the toner particles are transferred from the OPC surface to paper surface with the help of electric fields. For this purpose the particles have to be charged. However, these particle charges lead to additional interactions between the particles and the surfaces, namely, the electrostatic force.

6.4.1 AFM-measurement of charged particles

A previous paper [104] described the measurement of the electrostatic force as a function of the particle-substrate distance with the atomic force microscopy (AFM) as well as the estimation of the particle charge.

The interaction force between an alumina particle with a diameter of $10\,\mu m$ and a flat alumina substrate is measured by means of force-distance curve. In a first series of measurements, the particle is uncharged and then charged by means of the electron beam of a SEM. The effect of charge on the alumina particle was observed in the force-distance curve (Figure 6-28, left) which indicates a long-range force between the adhesion partners. The interaction force measured from zero-force point and jump-out point is approximately $300\,nN$ larger if the particle is charged in comparison to when it is uncharged. This is attributed to the electrostatic force (Figure 6-28, right).

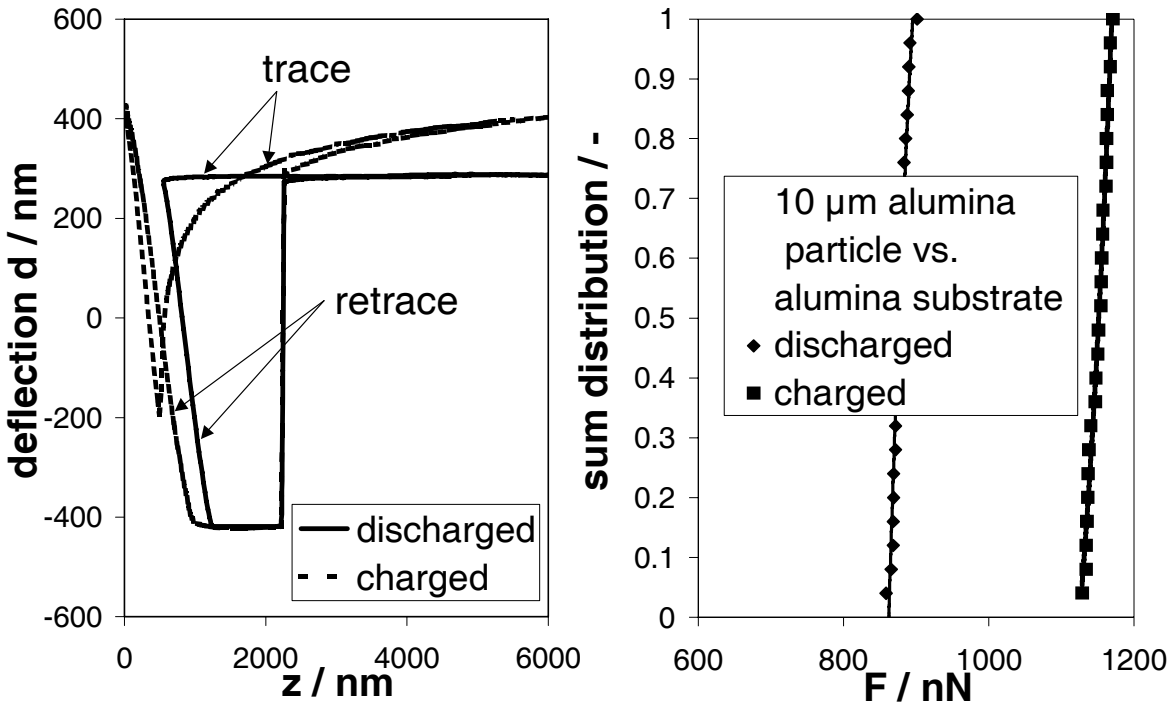

Figure 6-28 Left: Influence of the particle charge on the form of the force-distance curve. Right: Influence of the particle charge on the total adhesion force measured between a spherical alumina particle and a flat alumina substrate with AFM.

The particle charge in the vicinity of the contact area comprises a remarkably high contribution to the electrostatic force at small particle-substrate distances because the electrostatic force is inversely proportional to the squared separation distance a^2. However, the charge distribution on the adhering particle is unknown. In addition to a mean charge Q_1 in the center of the particle an additional point charge Q_2 is assumed to be near the contact region, which represents the charges in the contact region. The distance s between the two charges is shown in Figure 6-29. Both point charges interact due to their respective images with the substrate. The electrostatic force can be approximated by:

$$F_e = \frac{\varepsilon_r - 1}{\varepsilon_r + 1}\left(\frac{Q_1^2}{16\pi\varepsilon_0 (a+R)^2} + \frac{Q_2^2}{16\pi\varepsilon_0 (a+R-s)^2}\right). \qquad \text{Eq. 6.9}$$

The particle-substrate distance a on the approaching part of the force-distance-curve can be determined from the piezo-position z and the cantilever deflection d. If the particle-substrate distance is much larger than the contact distance $a_0 = 0.4\,nm$, the van der Waals force is negligible. The profile of the approaching part of the force-distance curve depends on the balance of the electrostatic force F_e and the tension of the cantilever $F_{cantilever}$.

$$F_e(a) = F_{cantilever}(d) \text{ if } a >> a_0. \qquad \text{Eq. 6.10}$$

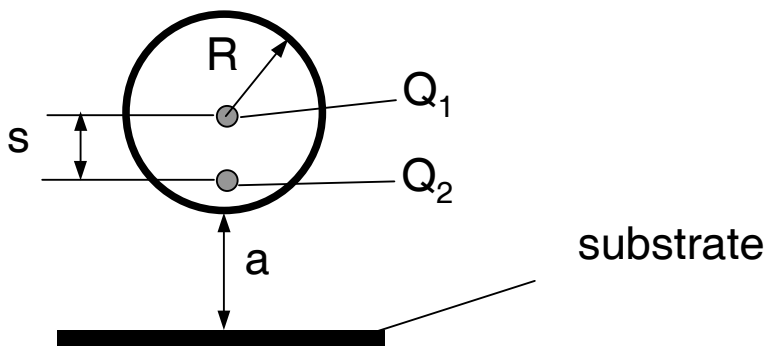

Figure 6-29 Geometry of the particle charge-substrate interaction.

By fitting the approaching part of the force-distance curve in Figure 6-28, left, between the charged particle and the alumina substrate ($\varepsilon_r = 11.6$, $R = 5000\,nm$) using the model Eq. 6.9, both point charge can be determined: $Q_1 = 37.6\,fC$ in the center of the particle and $Q_2 = 6.9\,fC$ at a distance of $s = 4364\,nm$ from the center of the particle, *i.e.*, the charge Q_2 is located several $100\,nm$ away from the contact position.

The individual electrostatic forces of both point charges $F_e(Q_1)$ and $F_e(Q_2)$, the total electrostatic force F_e and the spring force of the cantilever $F_{cantilever}$ are shown in Figure 6-30 as functions of the particle-substrate distance a. It is remarkable that a

relatively small charge in the vicinity of the contact position of approximately 18% of the total charge contributes to about $2/3$ (over $200\,nN$) to the total electrostatic force, when the adhesion partners are in contact.

According to the fitting of the approaching part of the force-distance curve the electrostatic force is $313\,nN$ when the particle and the substrate are in contact. This value is very close to the difference of approximately $300\,nN$, which is obtained between the adhesion forces measured with the charged and with the uncharged particle, respectively (Figure 6-28, right). This indicates that this simple model can well describe the adhesion between charged adhesion partners.

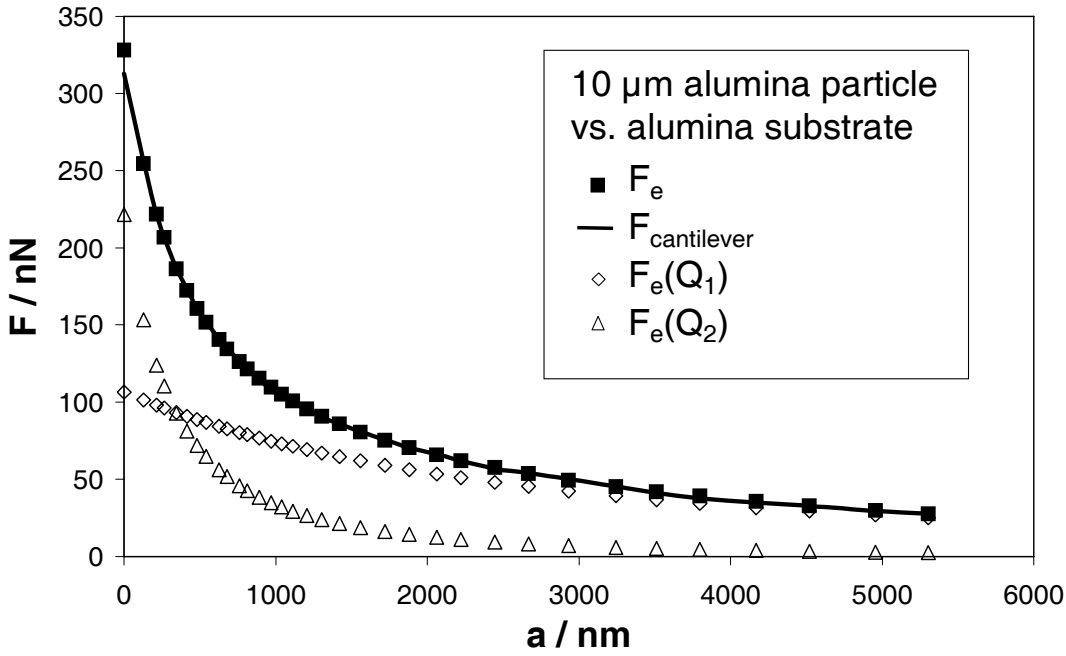

Figure 6-30 Calculated electrostatic forces (total force and forces due to the two point charges) and the spring force of the cantilever as functions of the particle-substrate distance.

During AFM-measurement of triboelectrically charged toner particles performed on various surfaces the effect of the electrostatic interaction is not significant. As it can be seen in the q-test measurement (Paragraph 5.2.2), the charge on a $10\,\mu m$ toner particle can rarely be more than $10\,fC$. Furthermore, a large portion of this charge is lost during the preparation (toner particles have to be triboelectrically charged at first, and then glued to the cantilever). The remaining amount of charges on the toner particle is therefore very small. Usually, no influence of the electrostatic force on the shape of the force-distance curve can be detected, even if an AFM-cantilever with very small spring constant is used for the measurement.

6.4.2 Centrifugal detachment measurement of charged particles

In the centrifuge detachment measurement the behavior of the charged toner particle ensembles is totally different from their behavior in the AFM-measurements. While the adhesion force values of the uncharged particles as obtained from the two measuring techniques are well comparable, this is clearly not the case for the charged particles. In centrifugal detachment measurements charged particle may lead to adhesion forces which are approximately one order of magnitude larger than in case of uncharged ones (Figure 6-31). Such different behavior is never observed during AFM-measurements.

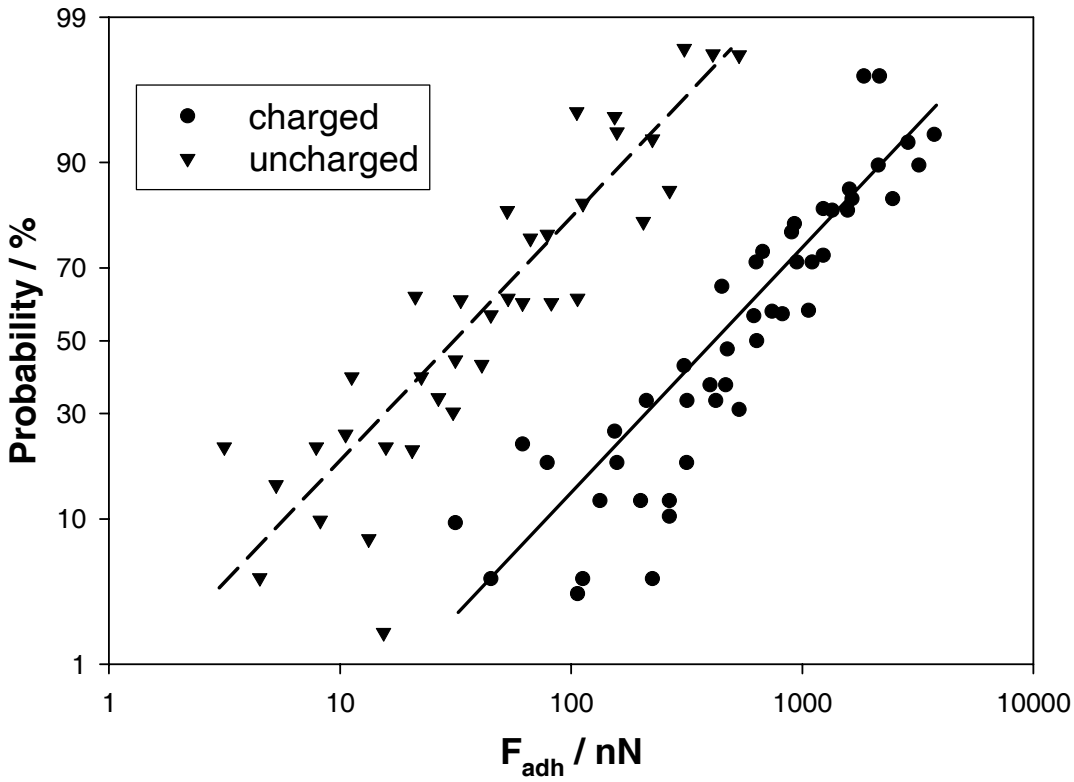

Figure 6-31 Adhesion force distributions between toner particles (magenta, with CCA, the surface is covered with $16\,nm$ silica nano-particles with a surface coverage of 30%) of various fractions from $6\,\mu m$ to $12\,\mu m$ and an OPC surface measured with the centrifugal detachment method.

One of the reasons for this large difference between the AFM and centrifuge detachment measurement may be the charge loss of the particle when it is glued to the tip of a cantilever. Actually, even if the particle surface charge was reaching its theoretical maximum, *i.e.*, the Gaussian limit of the charge density in air of $2.65 \cdot 10^{-5}\,C/m^2$, the particle charge and the electrostatic part of the adhesion force of a $10\,\mu m$ spherical particle could maximally reach [39, 45]:

$$Q_{max} = \sigma_{max} \cdot 4\pi R^2 = 8.3\, fC \text{ and} \qquad \text{Eq. 6.11}$$

$$F_{e,max} = c_1 \cdot \frac{Q_{max}^2}{16\pi\varepsilon_0 R^2} = 12\, nN\,, \qquad \text{Eq. 6.12}$$

respectively.

Even the maximal electrostatic force is significantly smaller, *i.e.*, negligible in comparison to the total adhesion force. Nevertheless, during the centrifugal detachment measurement this small force is sufficiently strong to cause the relocation of the particle, which may lead to a new stable position which is characterized by an increased number of contact points. Since the investigated toner type has a relatively low surface coverage of silica ($\sim 30\%$), the contact area and the adhesion force increase significantly through the relocation (cf. Paragraph 6.2.9). This increase ($F_{adh,50}$ from $40\,nN$ to $570\,nN$) is similar to those during the centrifugal detachment measurement where normal force is applied on a toner type with a similar surface coating ($F_{adh,50}$ increases from $43\,nN$ to $880\,nN$, see Figure 6-20). One may conclude that the particle charge does not affect the particle-substrate adhesion strongly, if the relocation effect can be eliminated.

6.4.3 Electric field detachment of toner particles

The most important behavior of the toner particle is of course its behavior in the electric field. A good toner sort shall be easily removable from the OPC surface with a possibly low electric field strength. This behavior is measured by means of the electric field detachment test. For this measurement the toner particles are triboelectrically charged, mixed with the carrier particles and agitated with a turbo-shaker for $15\,min$.

The two magenta toners are quite similar with respect to the polymer material and to the surface coatings, except that one contains CCA and the other one not. This results in a slight difference of the chargeability, which can be observed in the q-test measurement, such as shown in Paragraph 5.2.2. In this paragraph, the effect of this difference on the adhesion behavior in the electric field is investigated.

Figure 6-32 shows the results of the toner jumping measurement between the toner particles (magenta, without CCA) and OPC surfaces. The experiment is carried out at ambient conditions. The detachment rate at each field strength level is shown as a function of the q/d-ratio. Over 80% of the toner particles have a q/d-ratio in the range between -1.2 and $-0.2\, fC/\mu m$. Therefore, only this fraction is shown in the diagram.

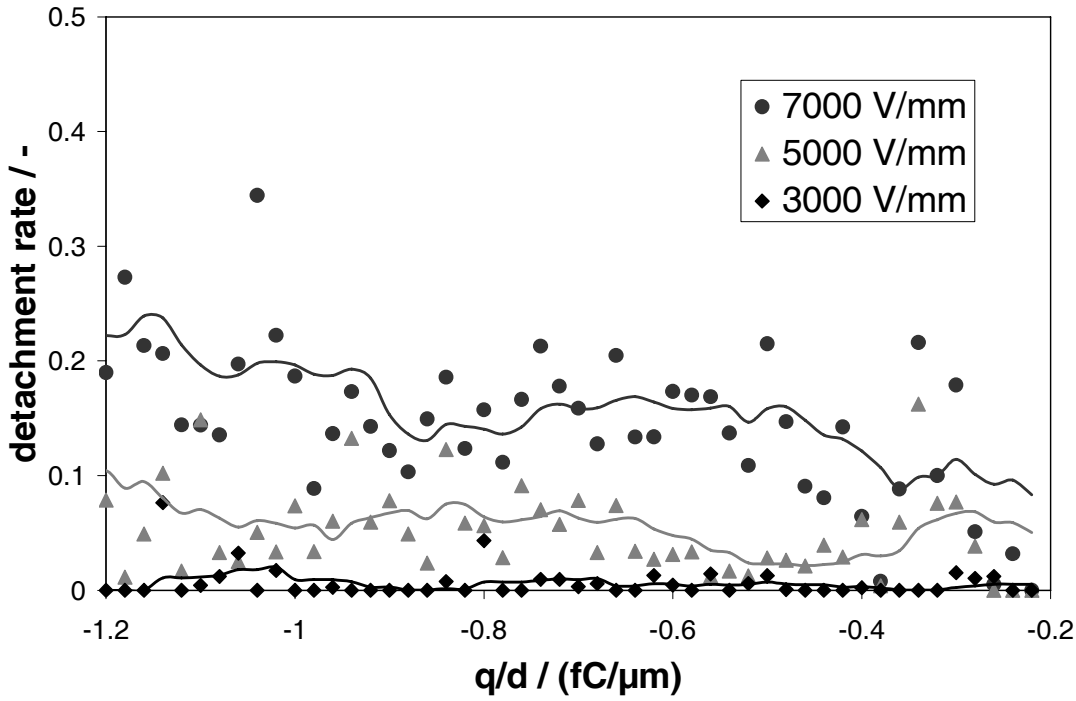

Figure 6-32 Electric field detachment of triboelectrically charged toner particles (magenta, without CCA, surface covered with $16nm$ silica nano-particles with a surface coverage of 30%) from OPC surfaces. The toner particles are negatively charged and dispersed on the substrate with the q-test equipment.

It can be observed that the overall detachment rate is quite low. Up to a field strength of $7000V/mm$, which is already above the theoretical air breakdown field strength, only approximately 20% of the toner particles are detached from the photo conductor surface. This indicates that in the electrophotographic process, the last layer of toner particles located on the OPC surface is usually not removed from the OPC surface. These particles are the fraction of toner, which has to be cleaned and deposited afterwards. Due to the low detachment rate and the strong scattering of the data, no dependence of the detachment rate on the q/d-ratio can be identified.

An interesting observation during the measurement is that some of the particles jump back and forth between the substrate and the counter electrode, which indicates that the charge transfer between the particles and the OPC surface or the counter electrode through contact charging is possible.

The particle charging is related to the voltage on the substrate surface. To understand the influence of the particle charging during the jumping process we investigated the detachment rate of the same toner type in dependence of the voltage between the electrodes. Since the field strength is related to the voltage with $E = U/D$, the voltage and the separation distance between the electrodes can be simultaneously varied, so that the field strength remains unaltered. In case of toner particles without CCA the voltage seems to have no effect on the detachment rate (Figure 6-33). The detachment

rate increases gradually with the field strength to a maximum value of 25%. Any further increase of the field strength has no effect on the toner detachment.

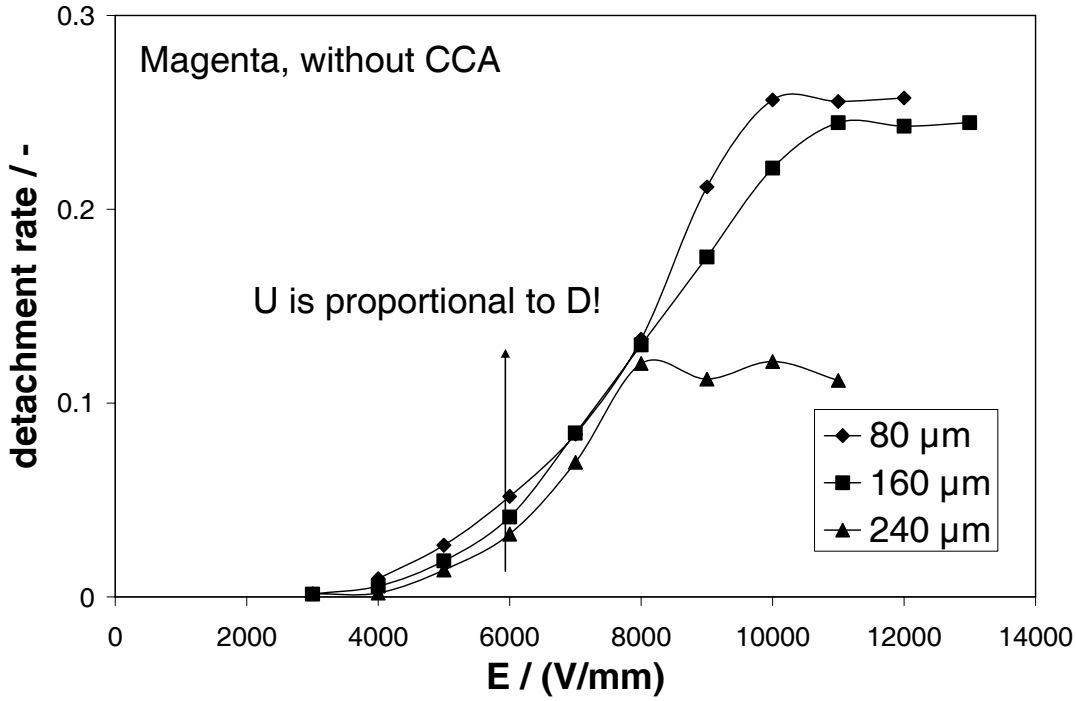

Figure 6-33 Detachment of triboelectrically charged toner particles (magenta, without CCA) from OPC surfaces in dependence of the field strength E and the separation distance between the electrodes D.

Nevertheless, the voltage has a slight influence on the detachment rate of the toner particles containing CCA. It can be observed in Figure 6-34 that at relatively low field strength (up to $7000 V/mm$) the detachment rate increases with the separation distance, in other words, it increases with the voltage. However, again the detachment rate does not increase monotonously with the field strength, it approaches asymptotically a maximum value of approximately 25%.

The classic explanation according to Hays [44] assumes that the electric forces on a charged particle in an electric field consist of three compounds (Eq. 2.38): The first compound is the image force of the particle charge; the second compound is the field force, which depends on the direction of the electric field – a negative field force is a detaching force; the third compound is the image force induced by the particle polarization. The image forces are always attractive.

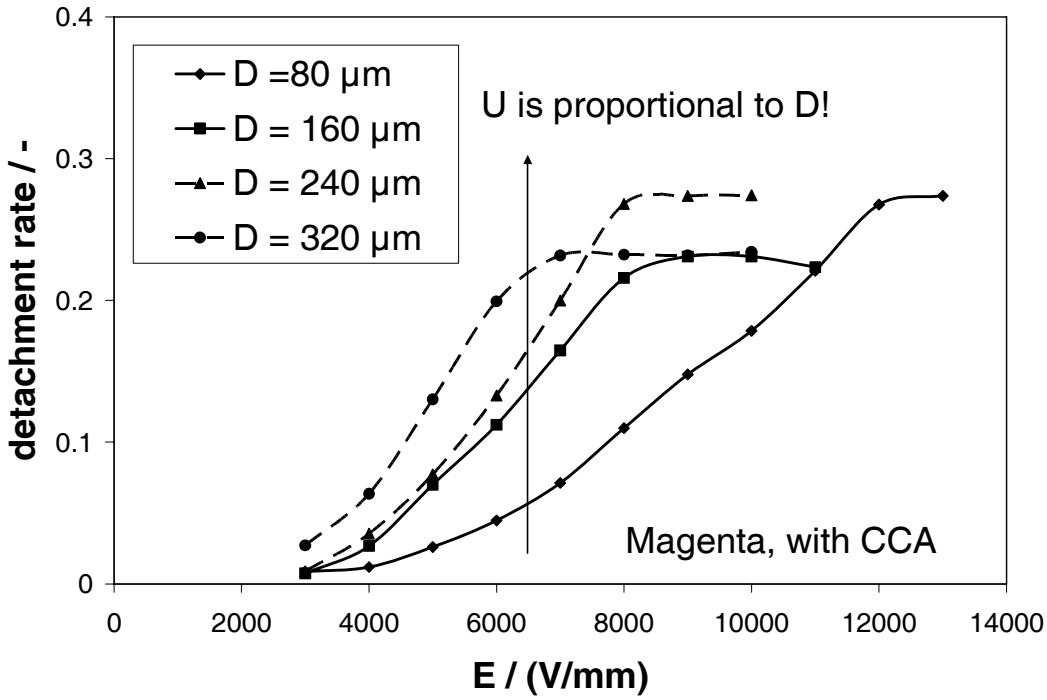

Figure 6-34 Detachment of triboelectrically charged toner particles (magenta, with CCA) from OPC surfaces in dependence of the field strength E and the separation distance between the electrodes D.

According to this model, there is a maximum of the electric detaching force. For the toner particles observed in this work the maximum electric detaching force can reach approximately $100\,nN$. Viewing the adhesion force of the charged particles as obtained from the centrifugal detachment method (Figure 6-31), it is clear that only a small part of the particles can be removed by the electric field force. One may conclude that the detachment rate can only be increased if the strong van der Waals force resulting from the relocation process of the particles can be minimized. As shown in Figure 6-35, the detachment rate can be significantly increased, if the surface coverage of silica nano-particle is increased. Especially for the fraction with a high q/d-ratio, high detachment rates, *i.e.*, above 80%, can be achieved (Figure 6-36).

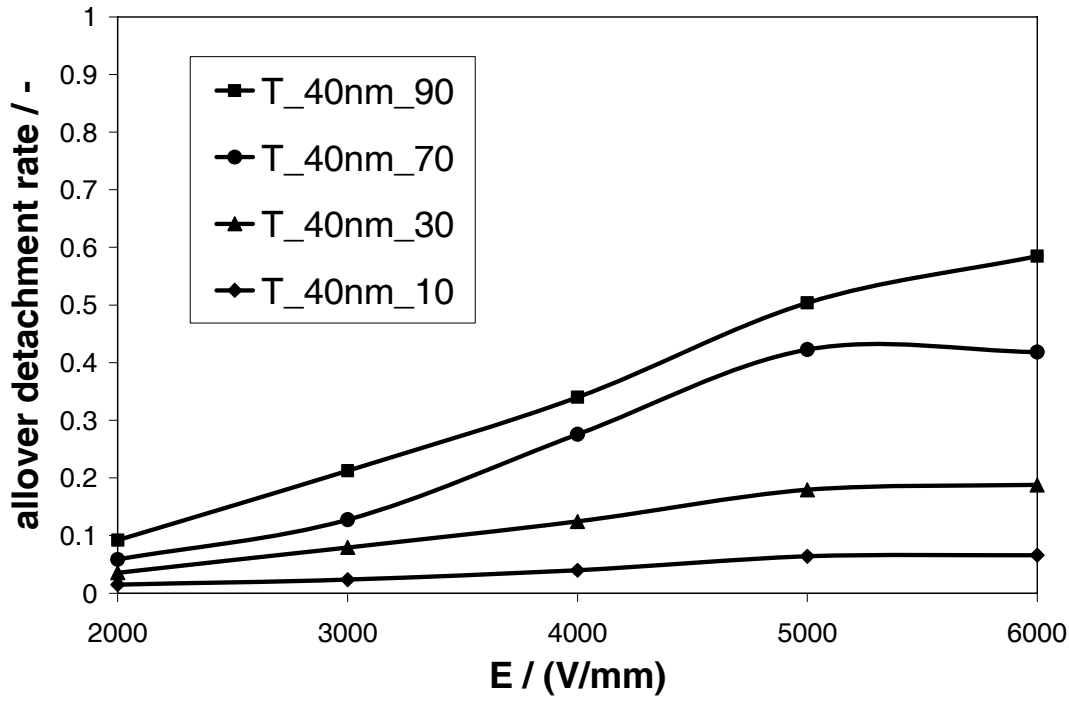

Figure 6-35 Detachment of triboelectrically charged toner particles with various surface coverage of silica nano-particle (see Table 6-3) from OPC surfaces in dependence of the field strength E .

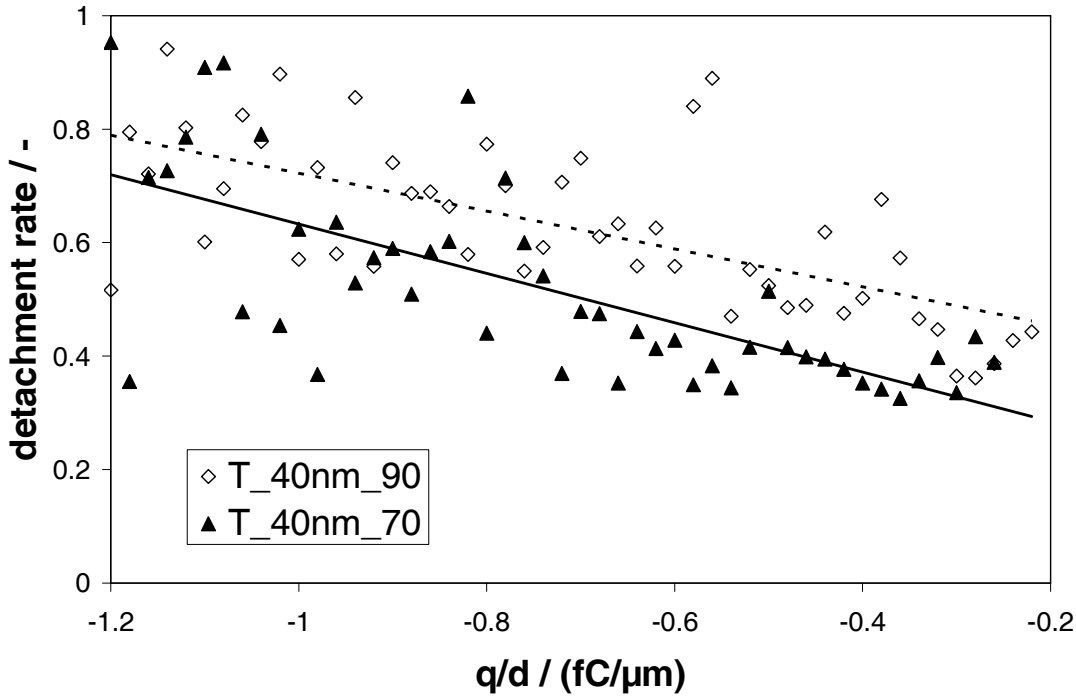

Figure 6-36 Detach rate of triboelectrically charged toner particles with various surface coverage of silica nano-particle in dependence of the q/d -ratio.

7 CONCLUSION AND OUTLOOK

7.1 Conclusion

For the optimization of the electrophotographic process it is necessary to deepen the understanding of the adhesion forces between toner particles and various substrate surfaces. The relevant adhesion forces in this process are the van der Waals, the capillary and the electrostatic forces. These forces depend on various physical parameters (*e.g.*, the material and surface properties, the load as well as the ambient conditions). In the frame of this work the relevant surface and bulk properties of the particles and substrates are characterized; a parameter study of the adhesion forces is carried out with diverse experimental and theoretical methods with the focus to minimize the particle-substrate adhesion forces.

While the van der Waals force is always present between particles and substrates in air, the capillary force only acts in humid ambience and the electrostatic force only between charged adhesion partners. Under well defined measuring conditions (*e.g.*, humidity, particle charging) the contribution of these different parts to the total adhesion force can be separately investigated.

The van der Waals force is characterized as the main part of the adhesion force in the electrophotographic process. In the frame of this work the dependence of the van der Waals force is investigated between different model adhesion partners as well as between real toner particles and substrates. The van der Waals force between smooth, rigid adhesion partners is usually characterized by narrow distributions and it depends neither on the applied normal force nor on the variation of the contact position. Between deformable particles and rigid substrate surfaces the adhesion force is a function of the mechanical properties of the materials and of the applied normal force. This behavior can be described with a model that makes use of FEM for the prediction of the particle deformation and numerical integration for the Hamaker summation. The characteristic values of the mechanical property required to carry out the FEM simulations are taken from literature and obtained from nanoindentation measurements.

The roughness of the contact region results in a reduction and in scattering of the van der Waals force. The corresponding adhesion force distribution depends on the size of the asperities as well as on their distribution on the particle and the substrate surface. The minimal adhesion force can be predicted with the same numerical method as applied for smooth adhesion partners. The shape of the adhesion force distribution can usually be characterized by a Weibull function (for substrates with a regular surface structure) or a log-normal function (for irregular surfaces). The width of the adhesion force distribution between a rigid spherical particle and a rigid, densest packing of

asperities can be numerically simulated. However, the width of the adhesion force distribution is strongly affected by the particle deformation and the irregularities in the packing of the asperities. In case of rough adhesion partners the applied normal force may result in an increase of the contact area through deformation and relocation, characterized by a significant increase of the van der Waals force. The influence of deformation and relocation can be significantly reduced by means of increasing the fraction of the surface covered with asperities.

In humid atmosphere water vapor is adsorbed on the surfaces and it may even condense in the contact region. Water adsorption on the surfaces reduces the Hamaker constant (hence the van der Waals force), while capillary condensation in the contact region gives rise to the meniscus force. Between smooth adhesion partners the adhesion force may decrease as soon as the surfaces are exposed to humidity. The adhesion force increases at higher relative humidity values because of the additional meniscus force. Between rough adhesion partners the meniscus is usually built between the asperity and the other adhesion partner. The radius of the meniscus turns out to be very small in comparison to the particle radius, so that the meniscus force, which is directly proportional to the cross section of the meniscus, is negligible in comparison to the van der Waals force within a wide humidity range.

In the printing process the particle charge is captured during a triboelectrical process, *i.e.*, during mixing the toner and the carrier particles and during mechanical agitation. However, the surface charge on the toner particle is usually so small that the resulting electrostatic force is at least one order of magnitude smaller than the van der Waals force. Nevertheless, the presence of the electrostatic force can result in a relocation of the particles to a new, more stable position, leading to an increase of the van der Waals force. In case of toner particles with a low surface coverage of silica nano-particles the detachment rate in the electric field is much lower than desired. An increase of the surface coverage is favorable for the improvement of the particle detachment.

7.2 Outlook

In the AFM-measurements the influence of the contact time and the measuring velocity can always be observed. Since the electrophotographic process is a highly transient process, it is necessary to understand the time-dependent behavior of adhesion. This can only be achieved by means of characterizing the time-dependent material and contact behaviors, *i.e.*, with the viscoelastic and the viscoplastic models for the description of the material property and applying an additional damping term resulting from the energy disappearance due to contact and separation.

Furthermore, the model is only available for systems, which can be assumed as approximately axisymmetric, with one adhesion partner being rigid and spherical and the other one deformable. However, most technical surfaces cannot be described sufficiently correct by axisymmetric models, furthermore, both adhesion partners are usually deformable to some extend. To simulate these cases the existing model needs to be extended in the future.

The behavior of the meniscus force is not well understood. In the regime of sub-micron-sized menisci the macroscopic model according to Kelvin cannot properly describe the geometry of the corresponding meniscus. Accordingly, the meniscus force cannot be predicted properly. It would be an interesting aspect to simulate the formation and the breakage of the meniscus by means of molecular dynamic methods.

Up to now the charging process is considered as a black box. There are only some empirical rules to predict the triboelectrical charging of polymer particles. More effort is necessary to control the charging of toner particles. For example, because of the overall low transfer rate of the magenta toner particles with 30% surface coverage of silica nano-particles, the influence of the CCA is not significant. It would be interesting to investigate the influence of the CCA in toner types with a relatively high transfer rate.

7.3 Suggestions for the electrophotographic process

The key to improve the transfer rate of toner particles in the electrophotographic process is to reduce the van der Waals force, whereas the deformation and the relocation of the particles have to be taken into consideration. In the investigated process the contribution of the meniscus and the electrostatic forces is less essential.

To achieve a minimum van der Waals force, both of the toner particle and the substrate surfaces should be coated with nano-particles. A relatively high coverage of the substrate is preferred to avoid a significant increase of the van der Waals force due to the relocation effect. The optimal size range of the roughness is around $50\,nm$ (cf. Figure 6-11). The coating of the toner particles could result in a further reduction of the particle-substrate interaction and prevent agglomeration of the toner particles.

CCA did not show a significant positive influence in the electric field detachment experiment shown in Figure 6-33 and Figure 6-34, the main reason is the low overall detachment rate due to the high van der Waals forces resulting from the relocation effect. In systems with significantly lower van der Waals forces the effect of CCA is promising, because using CCA the particle charge distribution becomes more homogeneous. There will be less uncharged particles which cannot be detached by the electric field and simultaneously there will be less strongly charged particles which then suffer from extremely large electrostatic forces.

8 NOMENCLATURE

8.1 Physical constants

e	$1.602 \cdot 10^{-19}\ C$	Elementary charge
h	$6.626 \cdot 10^{-34}\ J \cdot s$	Planck's constant
k_B	$1.381 \cdot 10^{-23}\ J / K$	Boltzmann constant
$\Re$	$8.31\, J / (mol \cdot K)$	Gas constant
ε_0	$8.854 \cdot 10^{-12}\ F / m$	Permittivity of vacuum

8.2 Latin symbols

A	J	Hamaker constant
A	m^2	Area
a	m	Distance between interacting bodies (contact distance $a_0 = 0.4\, nm$)
a	m / s^2	Acceleration
C	$J \cdot m^6$	London-van der Waals constant
c	–	Coefficient
D	m	Distance between electrodes
d	m	Particle diameter
E	Pa	Young’s modulus
E	V / m	Electric field strength
E_B	V / m	Breakdown electric field strength
F	N	Force
$\tilde{F}$	–	Normalized force
f	m^2	Contact area
f	Hz	Resonance frequency
G	Pa	Shear modulus
h	m	Height
I	A	Current

K, $K(t)$	Pa	Elastic constant
k	N/m	Spring constant of cantilever
l	m	Length
M	kg	Mass
n	–	Natural number (Lifshitz theory, Paragraph 2.1.1) or exponent (Götzinger theory, Paragraph 2.1.3.1)
P	–	Probability
p	Pa	Pressure
p_s	Pa	Saturation vapor pressure
p_{pl}^{H}	Pa	Hertzian Hardness
Q, q	C	Charge
R	m	Particle radius
R	Ω	Electric resistance
rms	m	Root-mean-square roughness
r	m	Radius in axisymmetric models or asperity radius or principal radius of a meniscus
S	m	Distance between two mass points
s	–	Slope of a curve
s	m	Thermal noise
T	K	Temperature
T	m	Thickness
t	s	Time
U	J	Interaction energy
U	V	Voltage
u	$C \cdot m$	Dipole moment
V	m^3	Volume
W, $W(a)$	J/m^2	Work of adhesion
$Z(\omega)$	Ω	Impedance
z	m	Height

8.3 Greek symbols

α, β	–	Coefficient
β, θ	–	Angle
γ	J/m^2	Surface energy
δ	m	Displacement
δ	–	Phase angle
ε	–	Strain
ε, ε_r	–	Dielectric constant or relative permittivity
$\varepsilon(i\nu)$	–	Dielectric constant at imaginary frequencies $i\nu$
ϕ	–	Relative humidity or work function (Paragraph 4.2.2)
κ	$1/(\Omega m)$	Conductivity
κ	–	Irreversible particle contact stiffness in the Tomas model (Paragraph 2.1.2.2)
η	$Pa \cdot s$	Viscosity
λ	–	Coefficient in the Maugis model (Paragraph 2.1.2.1)
λ	m	Peak-to-peak distance
λ	$1/s$	Rate of relaxation (in Eq. 4-13)
μ	$m^2/(V \cdot s)$	Electrical mobility
ν	Hz	Frequency, ν_I is the ionization frequency
ν	–	Poisson's number
ρ	$1/m^3$ or kg/m^3	Number concentration or density
ρ	Ωm	Specific resistance
σ	C/m^2	Surface charge density
σ	Pa	Stress
σ_0	Pa	Theoretical cohesive stress in the Maugis model (Paragraph 2.1.2.1)
τ_0	s	Time constant of the time-dependent meniscus force
ω	$1/s$	Angular velocity

8.4 Index

50	Median value
AC	Alternating current
adh	Adhesion
C	Contact
CPD	Contact potential difference
$crit$	Critical
D	Dispersion
DC	Direct current
E	Elastic
e	Electric
eqm	Equilibrium
G	Gas
L	Liquid
Lap	Laplace
M	Mechanical
m	Meniscus
max	Maximal
min	Minimal
N	Normal
pl	Plastic
S	Surface
S	Solid
T	Total
V	Vertical
vdW	Van der Waals
vis	Viscous
x,y,z	Cartesian coordinates
x,z,θ	Axisymetric coordinates

8.5 Abbreviations

AFM	Atomic force microscope
CCA	Charge control agency
CGL	Charge generating layer
CTL	Charge transfer layer
CSM	Continuous stiffness measurement
DMA	Dynamic mechanic analysis
EDX	Energy-dispersive X-ray spectroscopy
EFM	Electric force microscopy
FEM	Finite element method
JR	Jumper roller
MR	Magnet roller
OPC	Organic photo conductor
PC	Photo conductor
PVD	Physical vapor deposition
SEM	Scanning electron microscope
SP	Surface potential
TM	Tapping mode

9 LITERATURE

1. Goel, N.S. and P.R. Spencer, *Toner particle-photoreceptor adhesion*, in *Adhesion Science Technology*, L.-H. Lee, Editor. 1975, Plenum Press: New York.
2. Hoffmann, R., *Modeling and simulation of an electrostatic image transfer*, in *Lehrstuhl für Technische Elektrophysik*. 2004, Technische Universität München: München.
3. Schein, L.B., *Electrophotography and development physics*. 2nd. ed. 1992, New York: Springer Verlag.
4. Williams, E.M., *The physics and technology of xerographic processes*. 1993, New York: John Wiley & Sons.
5. Rimai, D.S., D.S. Weiss, and D.J. Quesnel, *Particle adhesion and removal in electrophotography.* Journal of Adhesion Science and Technology, 2003. **17**(7): p. 917-942.
6. Mizes, H., et al., *Small particle adhesion: measurement and control.* Colloids and Surfaces A-Physicochemical and Engineering Aspects, 2000. **165**(1-3): p. 11-23.
7. Schütz, W., *Haftung von Feststoffpartikeln an Festkörperoberflächen in gasförmiger Umgebung. Einfluss von Anpresskräften und der Umgebungsfeuchte*, in *Fakultät für Chemieingenieurwesen*. 1979, Universität Karlsruhe: Karlsruhe.
8. Israelachvili, J.N., *Intermolecular and surface forces*. 2nd. ed. 1991, San Diego: Academic Press.
9. Krupp, H., *Particle adhesion - Theory and experiment*, in *Advances in Colloid and Interface Science*, J.T.G. Overbeck, Prins, W., Zettlemoyer, A.C., Editor. 1967, Elsevier: Amsterdam. p. 111-239.
10. Visser, J., *Adhesion of colloidal particles*, in *Surface and Colloid Science*, E. Matijevic, Editor. 1976, Wiley: New York. p. 3-84.
11. Hamaker, H.C., *The London-van der Waals attraction between spherical particles.* Physica IV, 1937. **10**: p. 1059-1072.
12. Israelachvili, J.N. and D. Tabor, *Van der Waals forces. Theory and experiment.* Progress in Surface and Membrane Science, 1973. **7**: p. 1-55.
13. Perreault, J.D., *Using atom optics to measure van der Waals atom-surface interactions*. 2005, The University of Arizona.
14. Peukert, W., C. Mehler, and M. Gotzinger, *Application of adsorption and adhesion measurements for particle surface characterization.* Particle & Particle Systems Characterization, 2002. **18**(5-6): p. 229-234.
15. Bradley, R.S., *The cohesive force between solid surfaces and the surface energy of solids.* Philos. Mag. , 1932. **13**: p. 853-862.
16. Krupp, H. and G. Sperling, *Theory of adhesion of small particles.* J. Appl. Phys., 1966. **37**(11): p. 4176-4180.
17. Rumpf, H., *Haftung und Festigkeit von Agglomeraten - Vergleich zwischen Modellrechnung und Experiment.* Pharm. Ind., 1972. **34**(4): p. 270-281.

18. Lifshitz, E.M., *The theory of molecular attractive forces between solids.* Soviet Physics, 1956. **2**: p. 73-83.
19. Tomas, J., *Mechanics of nanoparticle adhesion - A continuum approach*, in *Particles on Surfaces 8*, K.L. Mittal, Editor. 2003, Brill Academic Publishers: Leiden p. 183-229.
20. Hertz, H., *Ueber die Berührung fester elastischer Körper.* Reine und Angewandte Mathematik, 1882: p. 156-171.
21. Johnson, K.L., K. Kendall, and A.D. Robert, *Surface energy and the contact of elastic solids.* Proc. R. Soc. Lond. A., 1971. **324**: p. 301-313.
22. Hui, C.Y., et al., *The accuracy of the geometric assumptions in the JKR (Johnson-Kendall-Roberts) theory of adhesion.* Journal of Adhesion Science and Technology, 2000. **14**(10): p. 1297-1319.
23. Derjaguin, B.V., V.M. Muller, and Y.P. Toporov, *Effect of contact deformations on the aAdhesion of particles.* Journal of Colloid and Interface Schience, 1975. **53**(2): p. 314-326.
24. Tabor, D., *Surface forces and surface interactions.* Journal of Colloid and Interface Science, 1976. **58**(1): p. 2-13.
25. Griffith, A.A., *The phenomena of rupture and flow in solids.* Philos. Trans. R. Soc. London A, 1920. **221**: p. 163-198.
26. Maugis, D., *Adhesion of spheres: The JKR-DMT transition using a Dugdale model.* Jounal of Colloid and Interface Science, 1992. **150**(1): p. 243-269.
27. Johnson, K.L. and J.A. Greenwood, *An adhesion map for the contact of elastic spheres.* Journal of Colloid and Interface Science, 1997. **192**(2): p. 326-333.
28. Molerus, O., *Theory of yield of cohesive powders.* Powder Technology, 1975. **12**: p. 259-275.
29. Rumpf, H., K. Sommer, and K. Steier, *Mechanismen der Haftkraftverstärkung bei der Partikelhaftung durch plastisches Verformen, Sintern und viskoelastisches Fließen.* Chem.-Ing.-Tech., 1976. **48**(4): p. 300-307.
30. Rumpf, H., *Die Wissenschaft des Agglomerierens.* Chem.-Ing.-Tech., 1974. **46**(1): p. 1-11.
31. Rumpf, H. *Particle adhesion*. in *Agglomeration 77, Proceedings of the Second International Symposium on Agglomeration*. 1977. New York: Wiley.
32. Rabinovich, Y.I., et al., *Adhesion between nanoscale rough surfaces - I. Role of asperity geometry.* Journal of Colloid and Interface Science, 2000. **232**(1): p. 10-16.
33. Rabinovich, Y.I., et al., *Adhesion between nanoscale rough surfaces - II. Measurement and comparison with theory.* Journal of Colloid and Interface Science, 2000. **232**(1): p. 17-24.
34. Liu, K.W., et al., *Combinatorial experiment in Ni-Ti thin films by laser interference structuring.* Applied Surface Science, 2005. **247**(1-4): p. 550-555.
35. Gotzinger, M. and W. Peukert, *Particle adhesion force distributions on rough surfaces.* Langmuir, 2004. **20**(13): p. 5298-5303.
36. Weibull, W., *A Statistical distribution function of wide applicability.* Journal of Applied Mechanics, 1951. **September**: p. 293-297.
37. Schütz, W. and H. Schubert, *Der Einfluß von Anpreßkräften auf die Partikelhaftung.* Chem.-Ing.-Tech., 1976. **48**(6): p. 567.

38. Langbein, D., *Non-retarded dispersion energy between macroscopic spheres.* J. Phys. Chem. Solids, 1971. **32**: p. 1657-1667.
39. Cross, J., *Electrostatics: principles, problems and applications*. 1987, Bristol: Adam Hilger.
40. Matsusaka, S. and H. Masuda, *Electrostatics of particles.* Advanced Powder Technology, 2003. **14**(2): p. 143-166.
41. Castle, G.S.P., *Contact charging between insulators.* Journal of Electrostatics, 1997. **40-1**: p. 13-20.
42. Schein, L.B., M. LaHa, and D. Novotny, *Theory of insulator charging.* Physics Letters A, 1992. **167**(1): p. 79-83.
43. Chen, A.H., H.T. Bi, and J.R. Grace, *Measurement of particle charge-to-mass ratios in a gas-solids fluidized bed by a collision probe.* Powder Technology, 2003. **135**: p. 181-191.
44. Hays, D.A., *Toner adhesion.* J. Adhesion, 1995. **51**: p. 41-48.
45. Hays, D.A. and J.Q. Feng, *Electrostatic forces on ion-charged toner particles.* Electrostatics, 2004(178): p. 77-82.
46. Zevenhoven, C.A.P., *Uni-polar field charging of particles: effects of particle conductivity and rotation.* Journal of Electrostatics, 1999. **46**(1): p. 1-12.
47. Unger, L., D. Boulaud, and J.P. Borra, *Unipolar field charging of particles by electrical discharge: effect of particle shape.* Journal of Aerosol Science, 2004. **35**(8): p. 965-979.
48. Anderson, J.H., *The effect of additives on the tribocharging of electrophotographic toners.* Journal of Electrostatics, 1996. **37**(3): p. 197-209.
49. Matsui, N., *Molecular structure of charge control agents (CCA) and toner triboelectrification II: The role of a molecular region with the same polarity as CCA charging in toner triboelectrification phenomena.* Journal of Imaging Science and Technology, 2000. **44**(1): p. 36-44.
50. Feng, J.Q. and D.A. Hays, *A finite-element analysis of the electrostatic force on a uniformly charged dielectric sphere resting on a dielectric-coated electrode in a detaching electric field.* IEEE Transactions on Industry Applications, 1998. **34**(1): p. 84-91.
51. Matsuyama, T. and H. Yamamoto, *The electrostatic force between a charged dielectric particle and a conducting plane.* Kona, 1998. **16**: p. 223-227.
52. Hays, D.A., *Adhesion of charged particles*, in *Fundamentals of Adhesion and Interfaces*, D.S. Rimai, Demejo, L.P., Mittal, K.L., Editor. 1995, VSP. p. 61-71.
53. Pollock, H.M., N.A. Burnham, and R.J. Colton, *Attractive forces between micron-sized particles: A patch charge model.* Journal of Adhesion, 1995. **51**(1-4): p. 71-86.
54. Feng, J.Q. and D.A. Hays, *Theory of electric field detachment of charged toner particles in electrophotography.* Journal of Imaging Science and Technology, 2000. **44**(1): p. 19-25.
55. Schein, L.B., Czarnecki, W.S., Christensen, B., Mu, T., Gallifort, G. *Theory of toner adhesion*. in *NIP20*. 2004. Salt Lake City.
56. Jones, T.B., *Electromechanics of particles*. 1995, New York: Cambridge University Press.

57. Farshchi-Tabrizi, M., et al., *On the adhesion between fine particles and nanocontacts: An atomic force microscope study.* Langmuir 2006. **22**(5): p. 2171-2184.
58. Stifter, T., O. Marti, and B. Bhushan, *Theoretical investigation of the distance dependence of capillary and van der Waals forces in scanning force microscopy.* Physical Review B, 2000. **62**(20): p. 13667-13673.
59. Rabinovich, Y.I., M.S. Esayanur, and B.M. Moudgil, *Capillary forces between two spheres with a fixed volume liquid bridge: Theory and experiment.* Langmuir, 2005. **21**(24): p. 10992-10997.
60. Li, J.C.M. and C.Z.Y. Wang, *Effect of moisture on the contact between a cylinder and a parallel plate.* Journal of Adhesion, 2005. **81**(10-11): p. 1049-1073.
61. Ata, A., Y.I. Rabinovich, and R.K. Singh, *Role of surface roughness in capillary adhesion.* Journal of Adhesion Science and Technology, 2002. **16**(4): p. 337-346.
62. Butt, H.J., B. Cappella, and M. Kappl, *Force measurements with the atomic force microscope: Technique, interpretation and applications.* Surface Science Reports, 2005. **59**(1-6): p. 1-152.
63. Pitois, O., P. Moucheront, and X. Chateau, *Liquid bridge between two moving spheres: An experimental study of viscosity effects.* Journal of Colloid and Interface Science, 2000. **231**(1): p. 26-31.
64. Zhou, H. and W. Peukert, *Modeling Adhesion Forces between Deformable Bodies by FEM and Hamaker Summation.* Langmuir, 2008. **24**(4): p. 1459 - 1468.
65. *ABAQUS 6.4-1 Documentation*. 2005, Weinheim: WILEY-VCH Verlag
66. Miesbauer, O., M. Götzinger, and W. Peukert, *Molecular dynamics simulations of the contact between two NaCl nano-crystals: adhesion, jump to contact and indentation.* Nanotechnology 2003. **14**(3): p. 371-376.
67. Luan, B. and M.O. Robbins, *Contact of single asperities with varying adhesion: Comparing continuum mechanics to atomistic simulations.* Physical Review E, 2006. **74**: p. 026111.
68. Nadai, A., *Theory of flow and fracture of solids, Volume 1*. 2nd edition ed. 1950: McGraw-Hill.
69. Kuchling, H., *Taschenbuch der Physik*. 1999, Leipzig: Fachbuchverlag.
70. Yang, C., U. Tartaglino, and B.N.J. Persson, *A multiscale molecular dynamics approach to contact mechanics.* Eur. Phys. J. E 2006. **19**(1): p. 47-58.
71. Combes, J.R., et al., *Toner compositions with surface additives*, in *United States Patent*. 2003: USA.
72. Götzinger, M., *Zur Charakterisierung von Wechselwirkungen partikulärer Feststoffoberflächen*, in *Lehrstuhl für Feststoff- und Grenzflächenverfahrenstechnik*. 2005, Universität Erlangen-Nürnberg: Erlangen.
73. Goldmann, G., *World of printers*. 2001: Océ Printing Systems.
74. Gunther, L. and W. Peukert, *Control of coating properties by tailored particle interactions: relation between suspension rheology and film structure.* Colloids

and Surfaces A-Physicochemical and Engineering Aspects, 2003. **225**(1-3): p. 49-61.
75. Beach, E.R., et al., *Pull-off force measurements between rough surfaces by atomic force microscopy.* Journal of Colloid and Interface Science, 2002. **247**(1): p. 84-99.
76. Meine, K., et al., *The influence of surface roughness on the adhesion force.* Surface and Interface Analysis, 2004. **36**(8): p. 694-697.
77. Gillies, G., et al., *Contact angles and wetting behaviour of single micron-sized particles.* Journal of Physics-Condensed Matter, 2005. **17**(9): p. S445-S464.
78. Binnig, G. and C.F. Quate, *Atomic force microscope.* Phys. Rev. Lett. , 1986. **56**(9): p. 930–933.
79. Giessibl, F.J., *Advances in atomic force microscopy.* Reviews of Modern Physics, 2003. **75**(3): p. 949-983.
80. Bhushan, B. and A.V. Goldade, *Kelvin probe microscopy measurements of surface potential change under wear at low loads.* Wear, 2000. **244**(1-2): p. 104-117.
81. Jacobs, H.O., et al., *Surface potential mapping: A qualitative material contrast in SPM.* Ultramicroscopy, 1997. **69**(1): p. 39-49.
82. Fujihira, M., *Kelvin probe force microscopy of molecular surfaces.* Annual Review of Materials Science, 1999. **29**: p. 353-380.
83. Baikie, I.D., et al., *Study of high- and low-work-function surfaces for hyperthermal surface ionization using an absolute Kelvin probe.* Journal of Vacuum Science & Technology A, 2001. **19**(4): p. 1460-1466.
84. Glatzel, T., S. Sadewasser, and M.C. Lux-Steiner, *Amplitude or frequency modulation-detection in Kelvin probe force microscopy.* Applied Surface Science, 2003. **210**(1-2): p. 84-89.
85. Bailey, A.G., *Charging of solids and powders.* Journal of Electrostatics, 1993. **30**: p. 167-180.
86. Garcia, R. and R. Perez, *Dynamic atomic force microscopy methods.* Surface Science Reports, 2002. **47**(6-8): p. 197-301.
87. Küttner, A., et al., *Theory and practice of a small toner-charge-spectrometer.* 1997.
88. Sharma, G.D., S. Sharma, and M.S. Roy, *Charge-carrier transport and photogeneration processes in pyronine (G) (PYR) sensitized-TiO2 photovoltaic device.* Materials Science and Engineering B-Solid State Materials for Advanced Technology, 2004. **110**(2): p. 135-142.
89. Wang, X. and P. Xiao, *Nondestructive characterisation of alumina/silicon carbide nanocomposites using impedance spectroscopy.* Journal of the European Ceramic Society, 2000. **20**: p. 2591-2599.
90. Thannberger, F.S., *Zur Eignung der Impedanzspektroskopie für die Charakterisierung von polymeren Langmuir-Blodgett-Schichten*, in *Institut für Technische Chemie, Lehrstuhl I*. 2002, Technischen Universität München.
91. Newbury, D.E., *Advanced scanning electron microscopy and X-ray microanalysis*. 1987, New York: Plenum Press.
92. Ward, I.M. and J. Sweeney, *An Introduction to the mechanical properties of solid polymers*. 1993, Chichester: John Wiley & Sons.

93. Oliver, W.C. and G.M. Pharr, *An improved technique for determining hardness and elastic modulus using load and displacement sensing indentation experiments.* J. Mater. Res., 1992. **7**(6): p. 1564-1583.
94. Fischer-Cripps, A.C., *Nanoindentation*. 2nd. ed. 2004, New York: Springer-Verlag.
95. Cappella, B. and G. Dietler, *Force-distance curves by atomic force microscopy.* Surface Science Reports, 1999. **34**(1): p. 5-104.
96. Hutter, J.L. and J. Bechhoefer, *Calibration of atomic-force microscope tips.* Review of Scientific Instruments, 1993. **64**(7): p. 1868-1873.
97. Stark, R.W., T. Drobek, and W.M. Heckl, *Thermomechanical noise of a free v-shaped cantilever for atomic-force microscopy.* Ultramicroscopy, 2001. **86**(1-2): p. 207-215.
98. Cleveland, J.P., et al., *A nondestructive method for determining the spring constant of cantilevers for scanning force microscopy.* Review of Scientific Instruments 1993. **64**(2): p. 403-405.
99. Fukuchi, Y. and M. Takeuchi, *Particle adhesion force measurements by toner jumping method*, in *IS&Ts NIP 15*. 1999.
100. Bergna, H.E. and W.O. Roberts. *Colloidal silica*. Ullmann's Encyclopedia of Industrial Chemistry 2000 [cited 2006.
101. Klapperich, C., K. Komvopoulos, and L. Pruitt, *Nanomechanical properties of polymers determined from nanoindentation experiments.* Journal of Tribology-Transactions of the Asme, 2001. **123**(3): p. 624-631.
102. Vogel, L. and W. Peukert, *Breakage behaviour of different materials - construction of mastercurve for the breakage probability.* Powder Technology, 2003. **129**(1-3): p. 101-110.
103. Lakes, R., *Elastic and viscoelastic behavior of chiral materials.* International Journal of Mechanical Sciences, 2001. **43**(7): p. 1579-1589.
104. Zhou, H., M. Gotzinger, and W. Peukert, *The influence of particle charge and roughness on particle-substrate adhesion.* Powder Technology, 2003. **135**: p. 82-91.
105. Bronstein, I.N., et al., *Taschenbuch der Mathematik*. 5 ed. 2001, Thun: Verlag Harri Deutsch.
106. Gotzinger, M. and W. Peukert, *Adhesive force distribution of rough adhesive systems for the example of a sphere-plate system.* Chemie Ingenieur Technik, 2003. **75**(12): p. 1848-1852.
107. Miranda, P.B., et al., *Icelike water monolayer adsorbed on mica at room temperature.* Physical Review Letters, 1998. **81**(26): p. 5876-5879.
108. Jang, J.K., G.C. Schatz, and M.A. Ratner, *Capillary force in atomic force microscopy.* Journal of Chemical Physics, 2004. **120**(3): p. 1157-1160.
109. Jang, J.Y., G.C. Schatz, and M.A. Ratner, *How narrow can a meniscus be?* Physical Review Letters, 2004. **92**(8): p. -.
110. Brunner, R., O. Marti, and O. Hollricher, *Influence of environmental conditions on shear-force distance control in near-field optical microscopy.* Journal of Applied Physics, 1999. **86**(12): p. 7100-7106.
111. Xu, L., et al., *Wetting and capillary phenomena of water on mica.* Journal of Physical Chemistry B, 1998. **102**(3): p. 540-548.

112. Podczeck, F., J.M. Newton, and M.B. James, *Variations in the adhesion force between a drug and carrier particles as a result of changes in the relative humidity of the air*. International Journal of Pharmaceutics, 1997. **149**(2): p. 151-160.

10 APPENDIX

10.1 Main features of Abaqus® 6.4.1

Finite element method (FEM) is a powerful technique originally developed for numerical solution of complex problems in structural mechanics. In the FEM, the structural system is modeled by a set of appropriate finite elements interconnected at points called nodes. Elements may have physical properties such as Young's modulus, Poisson's ratio, density, *etc*.

Abaqus® is a commercial FEM program developed by Abaqus, Inc., which is primarily designed to model the behavior of solids under externally applied loading. It provides a sophisticated capability to model contact between solids. The material properties of the solids can be defined with the help of an advanced material library, including the usual elastic and elastic-plastic solids; models for foams, concrete, and many others.

The analysis of the particle-substrate adhesion as a static problem with Abaqus® consists of three phases:

1 Pre-processing – defining the finite element model and environmental factors to be applied to it. As shown in Section 10.2, the geometry and the materials of the adhesion partners and the constraints (including contacts) are defined in this phase.

2 Analysis solver – solution of finite element model using Abaqus/Standard®. The program conducts a series of computational procedures involving applying forces and constraints and determining the effects such as deformations, strains, and stresses.

3 Post-processing of results using the visualization tools Abaqus/View®, the displacement of the nodes on the contact surface can be exported to the program for the calculation of the van der Waals force, which is shown in Section 10.3.

10.2 Input file for the FEM-simulation with Abaqus® 6.4-1

```
*HEADING
Static, axisymmetric, 4-nodes-elements.
**
** Definition of the nodes (node number, x, y coordinate) in nm
*NODE
1, 100., 100.
2, 90., 100.
…
```

```
**
** Definition of the axisymmetric elements, which consist of 4 nodes (element
number, numbers of the 4 nodes).
*ELEMENT, TYPE=CAX4, ELSET=PARTIKEL
1, 1, 2, 13, 12
2, 2, 3, 14, 13
…
**
** Definition of the contact line CLINE, which consists of 23 nodes.
*NSET, NSET=CLINE
111, 112, 113, 114, 115, 116, 117, 118, 119,…
**
** Definition of nodes LNODE, on which the normal force acts. The nodes are in the
middle of the particles.
*NSET, NSET=LNODE
1089, 1099,…
**
** Definition of a reference node RNODE for the control of the substrate position.
*NSET, NSET=RNODE
1194,
**
** Properties of the particle: system orientation and material properties.
*ORIENTATION, SYSTEM=R, NAME=OID1
1., 0., 0., 0., 1., 0. 2, 0.
*SOLID SECTION, ELSET=PARTICLE, MATERIAL=POLYSTYRENE,
ORIENTATION=OID1
1.,
**
** Definition of the material properties in nm/kg/s- unit system: density, Young's
modulus, Poisson's number and plastic deformation as a function of the stress.
*MATERIAL, NAME=POLYSTYRENE
*DENSITY
1.05E-24,
*ELASTIC, TYPE=ISO
3.3, 0.32
*PLASTIC
0.05, 0.0
0.1, 0.03
**
** Set the displacement of the nodes on the rotation axis in the radial direction to zero.
*BOUNDARY, OP=NEW
```

```
11, 1, , 0.
22, 1, , 0.
33, 1, , 0.
…
**
** Definition of the contact region: Geometry of the substrate – a line from (-100, -50) to (1000, -50) and the contact line of the particle CLINE. The friction coefficient is supposed to be 0.5
*RIGID BODY, ANALYTICAL SURFACE=M_CONTACT, REF NODE=RNODE
*SURFACE, TYPE=SEGMENTS, NAME=M_CONTACT, FILLET RADIUS=0.
START, -100., -50.
LINE, 1000., -50.
*SURFACE, TYPE=NODE, NAME=S_CONTACT
CLINE,
**
*CONTACT PAIR, INTERACTION=CONTACT
S_CONTACT, M_CONTACT
*SURFACE INTERACTION, NAME=CONTACT
*FRICTION, SLIP TOLERANCE=0.02
0.5,
**
** Step 1, Approaching of the surfaces
*STEP, AMPLITUDE=RAMP, INC=2000, NLGEOM=YES
*STATIC
0.5, 1., 1e-6
** Definition of the boundary conditions for the approaching: the substrate is fixed in all of the 6 degrees of freedom (DOF) in which RNODE is fixed. The particle is moved -50.003 nm in y-direction to approach the substrate, so that the contact between the adhesion partners is established.
*BOUNDARY, OP=NEW
RNODE, 1, 6, 0.
LNODE, 2, 2, -50.003
*END STEP
**
** Step2, The normal force is now applied. The substrate is fixed further on and a normal force of -100 nN in y-direction is applied to the LNODE on the particle.
*STEP, AMPLITUDE=RAMP, INC=2000, NLGEOM=YES
Step 2: F_V = 100 nN
*STATIC
0.005, 1.0, 0.00001, 0.05
*BOUNDARY, OP=NEW
```

```
RNODE, 1, 6, 0.
*CLOAD, OP=NEW
LNODE, 2, -100.
*END STEP
**
** Definition of further steps with different normal forces.
…
```

10.3 Nassi-Shneidermann diagram for the Hamaker Summation

The program for the Hamaker summation is described in Paragraph 3.2.2. Here the Nassi-Shneidermann diagram is given. The input file for the simulation is generated from the FEM-simulation containing the information of the nodes: x-position and the distance to the rigid surface in z-direction. For example, the profile of a $10\,\mu m$ particle before deformation takes place is shown in the followed table, with all the values given in μm:

x / µm	z_min / µm
0	0.0004
0.01	0.00041
0.02	0.00044
0.03	0.00049
0.04	0.00056
0.05	0.00065
…	…

Hamaker summation: main

Input the radius of the rigid adhesion partner and the Hamaker constant between the adhesion partners
Define the region of the Hamaker summation in the deformable particle in an axisymmetric coordinate system (x, z), see Figure 3.2, right
Define the starting discretization of the deformable particle
Read the profile data of the deformed particle from the data file (x, z_min) created by the axisymmetric FEM-simulation
Fit the profile of the deformed particle between the discrete data points with a cubic spline
Calculate the interaction energy in contact, i.e. contact distance is 0.4 nm with the subroutine "function_phi"
Set the adhesion partners to an infinitesimal distance, e.g. 0.002 nm to assure sufficient precision
Calculate the interaction energe at this distance with the subroutine "function_phi"
Calculate the adhesion force according to eq. 3-15

Hamaker summation: function_phi

Read the radius of the rigid particle, the distance between the adhesion partners and the parameters of the cubic spline from the program "main"
Set the starting values of the discretization size, interaction energy = 0 and error = 100 %
Interpolate the profile of the deformable particle with the cubic spline and the discretization size: (x, z_min) for each discrete point
Modify the values of z_min with an additional value equal to the distance between the adhesion partners, in contact this value is zero
Calculate the interaction energy according to eq. 3-14
Calculate the relative error between the calculated interaction energy and the previous value
Reduce the discretization size to the half of the previous value
If error is smaller than a given value, e.g. 2 %
Return the value of the interaction energy to the program "main"

10.4 Nassi-Shneidermann diagram for the simulation of roughness effect

Adhesion force rigid particle - rough surface

- Define the number of asperities, particle radius and Hamaker constant
- Define the wished discretization in x and y directions to position the particle
- Read the (x, y, z)-coordinate of the asperity centers from the input file
- Manually input the asperity radius
- Manually input the index of the asperity in the middle of the field
- For x-position of the particle center = 0 .. maximal
  - For y-position of the paritlce center = 0..maximal
    - Set the variation range of the center of the particle: (z_min..z_max) and a start value z_p
    - For i=1..number of asperities
      - Calculate the distances of the center of the particle and the asperity in x, y and z-directions: dx[i], dy[i] and dz[i]
      - Calculate the contact distance a[i] according to Eq. 6-5 and the angle of the line connecting the centers and the x-y plane theta[i] according to Eq. 6-6
      - Calculate the minimal of the contact distance between the particle and the asperities a_min = min(a[i])
    - if a_min < 0.4 nm
      - Set z_min = z_p; z_p=(z_min + z_max)/2
    - if a_min > 0.4nm + infinitesimal error
      - Set z_max = z_p; z_p=(z_min + z_max)/2
    - Until a_min is in the range 0.4 nm..0.4 nm + infinitesimal error
    - For i = 1..number of asperities
      - Calculate the adhesion force F_adh[i] between the particle and each asperity according to Eq. 6-7
    - Calculate the sum of the adhesion forces concerning the angles theta[i]
    - Append the value of the adhesion force to the results table

Curriculum vitae

Name	ZHOU, Hongben
Birthday and place	16.03.72 in Shanghai, China
Nationality	Chinese
Family status	Married, one child

Sep. 78 – Jul. 94	Guangji primary school in Ningbo, China
Sep. 84 – Jul. 90	Ningbo middle school in Ningbo, China Qualification for university entrance (Jul. 1990)
Sep. 90 – Jul. 94	Pharmaceutical studies at Zhejiang Medical University, Hangzhou, China – Bachelor exam (Jul. 1994)
Aug. 94 – Aug. 95	Salesman at Xiaogang Pharmaceutics Ltd., Ningbo, China
Sep. 95 – Mar. 97	German course at Tongji University, Shanghai, China and at TU Bergakademie Freiberg, Germany
Apr. 97 – Feb. 02	Process engineering studies at TU Bergakademie Freiberg and at Universität Stuttgart, Germany – Majors: Chemical process engineering Apparatus and machine engineering – Diploma exam (Feb. 2002)
Apr. 02 – Oct. 06	Scientific co-worker at the Institute of particle technology (Prof. Peukert), Universität Erlangen-Nürnberg, Germany Research field: Adhesion of polymer particles
Since Dec. 06	Research engineer at Lafarge research center, St. Quentin-Fallavier, France